INSTITUTE OF NATURAL AND APPLIED SCIENCES
UNIVERSITY OF CUKUROVA

PhD THESIS

Sezgin AYDIN

PERFORMANCE IMPROVEMENT OF AN AGATA SEGMENTED GERMANIUM DETECTOR

DEPARTMENT OF PHYSICS

ADANA, 2009

ÇUKUROVA ÜNİVERSİTESİ
FEN BİLİMLERİ ENSTİTÜSÜ

BÖLÜMLÜ AGATA GERMANYUM DETEKTÖRÜNÜN PERFORMANS ARTTIRIMI

Sezgin AYDIN

DOKTORA TEZİ
FİZİK ANABİLİM DALI

Bu tez 20.02.2009 tarihinde aşağıdaki jüri üyeleri tarafından oybirliği ile kabul edilmiştir.

İmza.....
Prof.Dr. Eda EŞKUT
DANIŞMAN

İmza.....
Prof.Dr. Sefa ERTÜRK
ÜYE

İmza.....
Prof.Dr. Ayşe POLATÖZ
ÜYE

İmza.....
Doç.Dr. İsa DUMANOĞLU
ÜYE

İmza.....
Doç.Dr. Mustafa TOPAKSU
ÜYE

Bu tez Enstitümüz Fizik Anabilim Dalında hazırlanmıştır.
Kod No:

Prof.Dr. Aziz ERTUNÇ
Enstitü Müdürü
İmza ve Mühür

Bu Çalışma Ç.Ü. Bilimsel Araştırma Projeleri Birimi Tarafından Desteklenmiştir.

Proje No: FEF 2007 D13

Not: Bu tezde kullanılan özgün ve başka kaynaktan yapılan bildirişlerin, çizelge, şekil ve fotoğrafların kaynak gösterilmeden kullanımı, 5846 sayılı Fikir ve Sanat Eserleri Kanunundaki hükümlere tabidir.

Sevgili aileme,

ABSTRACT

PhD THESIS

PERFORMANCE IMPROVEMENT OF AN AGATA SEGMENTED GERMANIUM DETECTOR

Sezgin AYDIN

DEPARTMENT OF PHYSICS
INSTITUTE OF NATURAL AND APPLIED SCIENCES
UNIVERSITY OF ÇUKUROVA

Supervisor: Prof.Dr. Eda EŞKUT
Year: 2009, Pages: 111
Jury: Prof.Dr. Eda EŞKUT
Prof.Dr. Sefa ERTÜRK
Prof.Dr. Ayşe POLATÖZ
Asc.Prof.Dr. İsa DUMANOĞLU
Asc.Prof.Dr. Mustafa TOPAKSU

This thesis is related to the development of AGATA, which is a new detection system for γ-ray spectroscopy based on the innovative concept of γ-ray tracking. AGATA is made up of a large number of high-purity Germanium detectors with the cathode segmented into 36 parts, providing the new capability of determining the position of the interaction points inside the bulk crystal with a precision of a few mm. Besides the problem of managing a much larger number of channels, the segmentation causes some new problems. One such problem is the electrical coupling between the various channels which causes a fold-dependent energy gain that must be corrected away to obtain the best energy resolution. Another problem is the incomplete charge collection affecting interaction events that take place very close to the segmentation lines, which degrades significantly the shape of the sum-energy peaks. This last effect was studied in detail in this thesis resulting in a practical event-by-event correction procedure which improves the energy resolution by up to 20% and increases by up to 50% the useful area of the low energy peaks.

Key Words: Charge sharing, Bow effect, crosstalk, segmented detector, AGATA array

ÖZ

DOKTORA TEZİ

BÖLÜMLÜ AGATA GERMANYUM DETEKTÖRÜNÜN PERFORMANS ARTTIRIMI

Sezgin AYDIN

ÇUKUROVA ÜNİVERSİTESİ
FEN BİLİMLERİ ENSTİTÜSÜ
FİZİK ANABİLİM DALI

Danışman: Prof.Dr. Eda EŞKUT
Yıl: 2009, Sayfa: 111
Jüri: Prof.Dr. Eda EŞKUT
Prof.Dr. Sefa ERTÜRK
Prof.Dr. Ayşe POLATÖZ
Doç.Dr. İsa DUMANOĞLU
Doç.Dr. Mustafa TOPAKSU

Bu tez çalışması, gama ışını spektroskopisi için henüz yeni olan gama-ışını izleme yöntemine dayalı AGATA detektör sisteminin geliştirilmesi ile ilgilidir. AGATA, kristal içindeki etkileşme noktasının pozisyonunu birkac mm hassaslıkla belirlenmesini sağlayacak, katodu 36 parçaya bölünmüş çok sayıda yüksek saflıkta germanyum detektöründen oluşmuştur. Fazla sayıda kanalı kullanma problemi yanısıra bölümlü olması bazı sorunlara yol açmaktadır. Bu sorunlardan biri etkileşme sayısı (Fold) bağımlı enerji kalibrasyonu gerektiren farklı kanallar arasındaki elektriksel bağlaşımdır ve iyi enerji çözünürlüğü elde etmek için dzeltilmesi gerekmektedir. Bir diğer sorun, toplam enerji piki şeklinin önemli ölçüde bozulmasına yol açan ve bölme çizgisine çok yakın yerlerde meydana gelen etkileşmeleri etkileyen eksik yük toplanmasıdır. Pratik olarak her etkileşmeyi ayrı ayrı düzeltme yöntemi ile bu son etki tezde detaylı olarak araştırılmıştır. Sonuç olarak enerji çözünürlüğü %20 ye kadar iyileştirilmiş ve düşük enerjili piklerdeki alan %50 ye kadar arttırılmıştır.

Anahtar Kelimeler: Yük Bölüşümü, Bow etkisi , crosstalk, bölümlü detektör, AGATA küresi

ACKNOLEDGEMENTS

This thesis would not have been imaginable without help and support of many people who also I have been not mentioned directly their name at this place.

I would like to thank to Dino Bazzacco for the supervision of my work. His help and suggestions were highly important for me and absolutely crucial in bringing this thesis to completion.

Further on I would like to thank my supervisor Prof. Dr. Eda EŞKUT for her continuous support and care during my stay in Çukurova University and in Italy.

I would like to acknowledge Prof. Dr. Sefa Ertrk who supported me during all stage of my scientific work.

I would like to thank İsa DUMANOĞLU for all his support.

I am also indebted to Enrico Farnea for correction of my thesis and to Francesco Recchia for numerous discussion during my work.

I owe my sincere gratitude to my colleges at LNL, Padova and Çukurova.

Finally I would like to thank to my parents, my sister and my brothers for support, understanding and being always together with me.

Particularly I would like to express my most important thanks to my wife Şebnem, for his love, encouragement and patience during my work.

TABLE OF CONTENTS **PAGE**

ABSTRACT I

ÖZ II

ACKNOLEDGEMENTS III

TABLE OF CONTENTS IV

LIST OF TABLES VI

LIST OF FIGURES VII

LIST OF SYMBOLS AND ABBREVIATIONS X

1. INTRODUCTION 1

2. PREVIOUS WORKS 3

3. BRIEF OVERVIEW 5

3.1. Radioactive Beam Facilities 5

3.2. New Instrumentation Required for In-Beam Experiments with Radioactive Ion Beams 7

3.3. Gamma-Ray Detection 8

3.3.1. Introduction 8

3.3.2. Interaction of Photons with Matter 10

3.3.3. Response Function 11

3.3.4. Bands in Solids 13

3.3.5. Inorganic Scintillators 16

3.3.6. High-Purity Germanium Detectors 18

4. The AGATA PROJECT 24

4.1. Arrays of Germanium Detectors 24

4.2. The γ-Ray Tracking Principles 27

4.3. Pulse Shape Analysis (PSA) 30

4.4. Review of the AGATA Project 32
4.5. The AGATA Detector 36
4.6. Preamplifiers 39
4.7. The AGATA Electronics 40
4.8. The AGATA Demonstrator 41
4.9. The AGATA Collaboration 43

5. EXPERIMENTAL WORK and RESULTS 46
5.1. The Test System 46
5.1.1. The TNT2 Digitizers 47
5.1.2. ENOB and SNR Measurement 51
5.1.3. Synchronization and Local Trigger 52
5.2. Characterization of Detector Noise and Disturbances 55
5.2.1. Application of the Fourier Transform to Characterize the Noise of the System. 57
5.2.1.1. Discrete Fourier Transform 57
5.2.1.2. Fourier Analysis of Signal Noise and Disturbances . . . 59
5.3. Work on the Detector 60
5.3.1. Spectra Alignment 61
5.3.2. Explanation of the Crosstalk. 63
5.3.3. Correction of Crosstalk. 66
5.3.4. Charge Sharing and the Bow Effect 71
5.3.4.1. Size of the Segmentation Lines 76
5.3.4.2. Correction of the Bow Effect 82
5.3.4.3. Combining the Segment and Core Spectra 85

6. DISCUSSION and CONCLUSION 90

REFERENCES 91

CURRICULUM VITAE 98

LIST OF TABLES **PAGE**

Table 3.1. Properties of Intrinsic Silicon and Germanium 21

Table 4.1. Geometrical characteristics of the configurations 35

Table 5.1. Geometrical characteristics of the configurations 82
Table 5.2. Energy resolution improvement 87
Table 5.3. Comparisons of the peak positions 87
Table 5.4. The peak area improvement 87
Table 5.5. The energy resolution improvement 88

LIST OF FIGURES **PAGE**

Figure 3.1. Description of the IFS and the ISOL method 5
Figure 3.2. Resolution of a detector 9
Figure 3.3. Major γ-ray interactions 10
Figure 3.4. Response function of a γ-ray detector. 12
Figure 3.5. Band structure in semiconductors. 13
Figure 3.6. Band structure of an inorganic scintillator. 14
Figure 3.7. Basic elements of a photomultiplier tube. 16
Figure 3.8. Concentration profiles for the *n*-*p* junction. 19
Figure 3.9. The variation in electron energy bands 20
Figure 3.10. Basic elements of an anti Compton shield. 22

Figure 4.1. The basic idea of the γ-ray tracking 25
Figure 4.2. Unsuppressed and suppressed spectra 26
Figure 4.3. γ-ray attenuation coefficients 28
Figure 4.4. Photopeak efficiency of an ideal germanium shell. 29
Figure 4.5. Pulse shape in segments 31
Figure 4.6. The investigated configuration. 33
Figure 4.7. The most attractive configuration of the array. 34
Figure 4.8. Calculated photopeak efficiency 35
Figure 4.9. The AGATA cryostat. 36
Figure 4.10. Segments effective size 37
Figure 4.11. The S001 prototype detector 38
Figure 4.12. Sketch of the AGATA test cryostat 38
Figure 4.13. The Preamplifiers 39
Figure 4.14. The Dataflow description 41
Figure 4.15. The AGATA Demonstrator efficiency 42
Figure 4.16. The AGATA Demonstrator Peak-to-Total ratio 43
Figure 4.17. Calculated peak FWHM of the AGATA Demonstrator Array 44
Figure 4.18. Absolute photopeak efficiency of the AGATA Demonstrator Array . . 44
Figure 4.19. Evolution of the AGATA project 45

Figure 5.1. A screen shot of the TUC program interface 49
Figure 5.2. Preamplifier signal and trapezoid 50
Figure 5.3. TNT2 cards performance 51
Figure 5.4. The TNT2 based data acquisition system. 54
Figure 5.5. Noisy and clean signals of the detector 55
Figure 5.6. Possible Fourier Transformations 58
Figure 5.7. FFT of the Noise 59
Figure 5.8. Energy spectra of different segments before gain alignment 62
Figure 5.9. Gain matched spectra for single-segment events. 63
Figure 5.10. Summed spectra of multi-segments events 64
Figure 5.11. Crosstalk effect of the 1.3 MeV gamma 65
Figure 5.12. Crosstalk effect of the cosmic ray 65
Figure 5.13. Comparison of the two crosstalk correction methods 69
Figure 5.14. Correlation between Seg. A1 and Seg. A2-A3 and A4 69
Figure 5.15. Crosstalk corrected sum-energy spectra for different numbers of fired segments. 70
Figure 5.16. After crosstalk correction, the amplitude in the “other” segments is 0 71
Figure 5.17. Bow effect on Segment A1-B1 72
Figure 5.18. The definition of the charge sharing 73
Figure 5.19. The bow effect in front segments. 74
Figure 5.20. The spectrum of the core for fold-1 and fold-2 events. 75
Figure 5.21. Statistic for interaction in segment A1, B1 and A1B1 for 60 keV . . . 75
Figure 5.22. The scanning table used to determine the size of the segmentation lines. 77
Figure 5.23. Sum of the gamma energies vs. corresponding difference for 60 keV 78
Figure 5.24. Intensity of the peak in segment A1 and B1 78
Figure 5.25. Geometrical draw of collimator 79
Figure 5.26. Intensity of the peak in segment A1 and B1 81
Figure 5.27. Intensity of the peak in segment A3 and B3 81
Figure 5.28. Correlation between core and sum of the segments. 83
Figure 5.29. Geometric model. 84

Figure 5.30. Correlation between core and sum of the segments after the bow correction. 85
Figure 5.31. Corrected spectra 86
Figure 5.32. Bow corrected spectra 86
Figure 5.33. Energy resolution of the average spectra 89

LIST OF SYMBOLS AND ABBREVIATIONS

A	Mass number
Z	Proton number
N	Neutron number
γ	Gamma radiation
β	Beta radiation
Ω	solid angle
σ	photoelectric absorption
μ	linear attenuation coefficient
θ	Theta angle
E_γ	Photon energy
FFT	Fast Fourier Transform
FET	Field Effect Transistor
$HPGe$	High Purity Germanium Detector
$CdZnTe$	Cadmium Zinc Telluride
$NaI(Tl)$	Sodium Iodide (Thallium)
BaF_2	Barium Fluoride
$CsI(Tl)$	Cesium Iodide (Thallium)
$DSSD$	Double-Sided Strip Detectors
BGO	$Bi_4Ge_3O_2$
ESS	Escape Suppressed Spectrometer
CSS	Compton Suppressed Scintillator
MWD	Moving Window Deconvolution
F	FOLD (Fired Segment number)
meV	Milielectronvolt
keV	Kiloelectronvolt
MeV	Megaelectronvolt
ΔE	Energy resolution
e	Electron charge
$\hbar$	Planck constant/2π
π	Pi number
$LN2$	Liquid Nitrogen

1. INTRODUCTION

Gamma rays emitted in nuclear reactions or in radioactive decays are the main probe for the investigation of the excitation structure of nuclei. From the energy and intensity of the emitted gamma rays it is possible to determine the position of the excited nuclear states; by measuring the emission times of the radiation it is possible to determine the lifetime and the deformation parameters of the emitting states; the angular distribution of the emitted gammas is connected to the spin of the emitting state and can be used to determine its nuclear magnetic and quadrupole moments; the polarization of the gamma rays gives the parity of the states. It is therefore not surprising that all major advances in the quality of the high resolution γ-rays detectors have resulted in important discoveries in nuclear structure.

The use of Germanium (Ge) detectors in γ-ray spectroscopy started in the early 1960s. These detectors led to a large increase in sensitivity and were used to determine the lowest excited states of many nuclei. The advent of the heavy-ions accelerators in the 1970s, made it clear that more detection sensitivity was needed to go deeper in spectroscopy studies. The solution adopted in order to improve the response function of the Ge detectors was the of use the escape suppression shield and the development of the detector arrays. The biggest detector arrays (EUROBALL and GAMMASPHERE), which were developed during the nineties, enabled to study the high multiplicity cascades of gamma rays emitted by nuclei populated in fusion-evaporation reactions.

The major challenge facing the γ-ray detection technique is the study of the most-exotic nuclei, at the limits of nuclear stability, which will be populated with radioactive beams provided by the next-generation high-intensity radioactive-beam facilities. The expected experimental conditions at such accelerators forced the development of a new detection techniques where, besides the energy of the absorbed radiation, the Ge detectors provide also the position of the interaction points within the crystal. Such information is later used to follow the scattering path of the gamma rays. This position sensitivity required by this new detection method comes from the recent development of large-volume highly-segmented Ge detectors and by major advances in digital electronics and computing enabling to manage the consequent huge increase in data processing. The main two projects that have taken up the challenge of building a γ-ray tracking detectors array are

AGATA in Europe and GRETA in USA. The projects and the related developments will be presented in Chapter 4.

The complex Germanium detectors used for γ-ray tracking present a series of complications and problems which must be solved and properly managed to obtain the requested performance. These problems and some of the proposed solutions are presented in Chapter 5.

2. PREVIOUS WORKS

Charge sharing between neighboring segments of multi electrode semiconductor detectors produces a degradation of the quality of the energy spectra due to the fact that the involved segments collect only part of the signal produced by the interacting radiation.

This is a serious issue in particular high resolution detectors like CdZnTe (Cadmium Zinc Telluride) or the HPGe (High Purity Germanium Detector) crystals which are the basic element of the modern large detector arrays used in high resolution gamma-ray spectroscopy. Several experimental studies have been carried out in the last years to understand the phenomenon and to find empirical methods to correct the detector signals so as to reduce the energy resolution losses.

One of these studies has been done by Chen (Chen et al., 2002) who investigated the effect of the segmentation geometry in various 8×8 pixel CdZnTe detectors with different inter-pixel distances. Together with the back-diagonal typical of shared detection, the energy-correlation matrix between two adjacent pixels displayed a "bow" due to charge loss in the inter-pixel gap. Chen et al. developed some numerical models which show that the amount of charge loss depends quite sensitively from the charge mobility and trapping time but they could not obtain a good fit of the data and did not suggest any method to correct for the charge losses.

Another study with CdZnTe detectors has been done by Kalemci (Kalemci and Matteson, 2002) who developed 2 mm thick position sensitive cross-strip detectors with 22 anode- and 22 cathode-strips and scanned the "gap" region with 10 μm precision by using a 30 μm collimated gamma-ray beam. Their studies have shown that charge sharing is a function of the interaction depth which depends on the energy of the incoming photon. They, found that, depending on the depth, a fraction of the electrons drifted to the inter-anode region causing incomplete charge collection. However, this study does not suggest a way to correct for the lost charge.

Some studies were also done using high-purity germanium detectors (HPGe). One of these is done by Hayward (Hayward and Weheb, 2008) who used double-sided strip detectors (DSSD) and simulated the dependency of the charge loss on the electric field. These simulation calculation show that the charge loss is strongly dependent on ratio of lateral-to-axial electric field E_l/E_z. Furthermore, they observed a greater charge loss

in the signals taken from the anode side, although anode and cathode of the detector underwent identical fabrication processes. According to their simulation this is due to some amount of charge immobilized on the surface of the gap which weakens the lateral field and inhibits the collection of carriers.

Coburn (Coburn et al., 2001) and Amman (Amman and Luke, 2000) used germanium strip detectors and agree on the fact that a small dead region under the gap is responsible for the incomplete charge collection and that the loss is related to the incident gamma-ray energy (i.e. to the depth of the interaction). They emphasized that to minimize the charge losses, the gap between strips should be as small as possible.

A similar effect was observed also in the MARS prototype detector (Nespolo, 2004). This detector was produced explicitly to study the effect of segmentation in large volume HPGe crystals. Although the gamma-gamma correlation matrices clearly indicated that charge loss is an issue for all these detectors, since now no viable solution was put forward on how to mitigate its impact on the quality of the gamma ray spectra.

3. BRIEF OVERVIEW

3.1 Radioactive Beam Facilities

It is clear that future developments in the Nuclear Structure field of research will depend strongly on the planned and under construction radioactive beam facilities. In fact, only using radioactive beam facilities it will be possible to access with sizeable cross sections very n–rich nuclei close to the neutron dripline, which is inarguably one of the most exciting challenges in Nuclear Structure.

There are basically two kinds of techniques to produce Radioactive Ion Beams (RIB): the In-Flight Separation (IFS) method and the Isotope Separation On-Line (ISOL) method. A schematization of the IFS and ISOL can be seen in Figure 3.1.

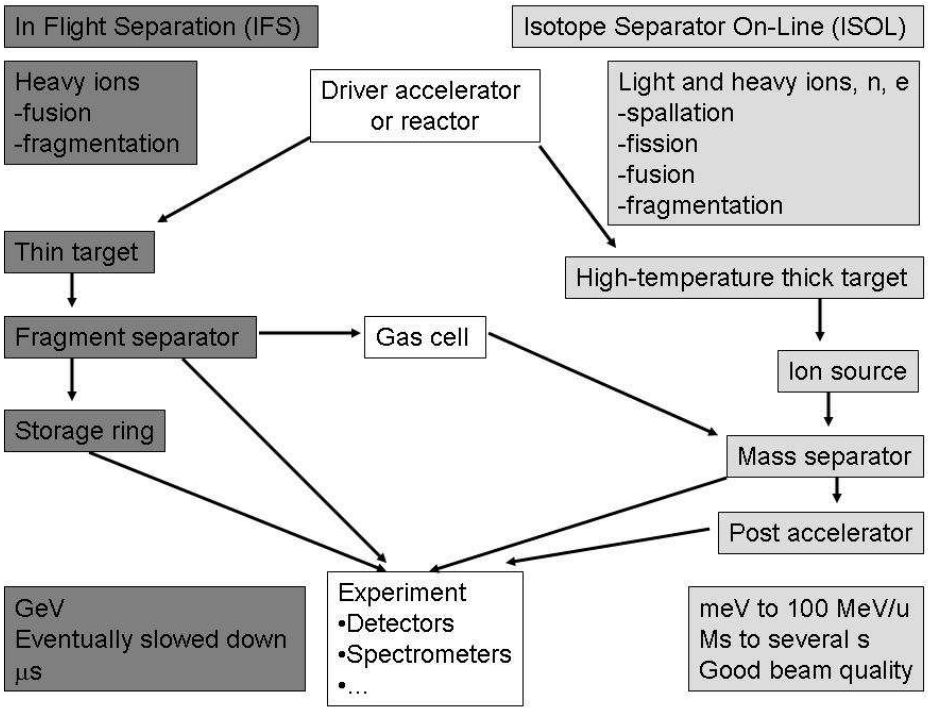


Figure 3.1 Description of the In-Flight Separation and the Isotope Separation On-Line method.

In the In-Flight Separation scheme, a heavy-ion beam at high energy (typically from 50 to several 100 MeV/u) collides with a thin target, resulting with high probability in projectile fragmentation. After the primary target area, a fragment separator system, com-

posed of electric and magnetic separators and degraders, selects the desired isotopes and focus them to the secondary target position for the studies of interest. With the In-Flight Separation method the secondary beam particles have a kinetic energy comparable to that of the primary beam; if needed they can be slowed down and stored in a storage ring. An additional advantage of this method lies in the fact that it is independent of chemistry so that all species with half lives greater than the flight time are available. The main disadvantages are a poor beam quality and a loss of intensity due to the use of thin targets. This technique is used, for instance, at the RISING facility of GSI Darmstadt (Wollersheim et al., 2005).

The experimental conditions at an IFS facility will be extremely challenging for γ-spectroscopy. The typically high energies and large emittance of the secondary beams point to a detector with very high effective granularity in order to perform good quality Doppler correction.

In an ISOL-type facility the radioactive nuclei are produced essentially at rest in a thick target by bombardment with particles from a primary source or driver-accelerator. After ionization and selection of a specific mass by electromagnetic devices, the radioactive nuclei are accelerated in a post-accelerator.

The two main advantages of the ISOL method are that it allows the use of a thick target and hence maximises the yield of nuclei of interest and provides beams of high quality, comparable or identical to that obtained with stable beams. The main disadvantage is that it depends critically on the chemistry of the species of interest. The ISOL technique is used, for instance, in the ISOLDE facility (Kugler, 2000) at CERN and it will be used in the planned EURISOL project (Cornell , 2003). It should be remarked that a project to build an ISOL facility at the Laboratori Nazionali di Legnaro has been recently approved. It is expected that the SPES (Study and Production of Exotic Species) (Prete, 2007) could be operational in the next few years.

The quality in terms of emittance of the beams produced by the ISOL method will be less critic than what is expected at an in-flight facility. Anyway, the low intensity and purity with respect to present beams will be a challenge for the detection and identification of the nuclei of interest. Also in this case, detection efficiency and selectivity turn out to be essential for γ-ray spectroscopy studies.

3.2 New Instrumentation Required for In-Beam Experiments with Radioactive Ion Beams

As anticipated in the previous sections, gamma ray spectroscopy experiments with exotic beams will shed light on many open problems in nuclear structure research. Performing this kind of measures means working in critical conditions due to the high amount of background radiation, relevant Doppler effects and low intensity of the beams.

For instance, in the case of secondary beams produced following projectile fragmentation, very high velocities (v/c up to 50%) and low beam intensities (a few pps in the case of the most exotic species) are expected. Therefore, in order to perform γ-ray spectroscopy experiments, high photopeak efficiency (larger than $\varepsilon_{ph} = 20\%$) should be combined with large granularity in order to keep the effective energy resolution, obtained following Doppler correction, below 1%. These values clearly exceed the possibilities provided by the existing devices, where the detection efficiency is typically lower than 10% for single photons and where, most importantly, such limiting resolution value is obtained at much lower recoil velocities, namely at $\beta \approx 5\%$. The situation is even worse at higher photon multiplicities, since in this case the detection efficiency of the "conventional" devices drops rapidly with the increasing photon multiplicity.

It is clear that the existing devices are not suited to perform γ-ray spectroscopy studies at the planned radioactive ion beam facilities, thus implying that new devices with much better performance should be developed. Following the discussion above, such new instruments should have:

- high efficiency (larger that 30–40%) also at high multiplicities to allow the use of radioactive ion beams and the study of nuclei produced with a low cross section;
- good position resolution for the individual photon interaction points in order to perform good quality Doppler correction in case of photons emitted by fast moving recoils ($\beta > 20\%$);
- high granularity to minimise the probability of multiple hits, even in case of high γ-multiplicity events;
- capability to stand a high count rate, to allow the use of high-intensity ion beams in

experiments where the nuclei of interest are produced with a low branching ratio;

- high efficiency (larger than 5%) also for high-energy γ-rays;
- capability to measure Compton scattering angles to allow the measurement of the linear polarisation of photons.

It is also clear that it will not be feasible to push the technology of Compton-suppressed arrays to its limits in order to meet the requirements posed by the future radioactive ion beam facilities. An alternative solution has been proposed and investigated since the mid-nineties, which implies developments on the (digital) signal processing software rather than on the detector hardware alone. This technique requires the use of highly electrically segmented germanium crystals combined with digital electronics in order to identify the positions of the single energy depositions within the crystals through a detailed analysis of the signal shape (*pulse shape analysis*). The energies of the individual photons will be subsequently extracted by powerful algorithms following (or *tracking*) the scattering sequences of each γ-ray.

Presently two major projects aim at the construction of an array of high-purity germanium detectors based on the novel concepts of *pulse shape analysis* and γ*-ray tracking*: AGATA (Gerl and Korten , 2001) in Europe and GRETA (GRETA Steering Committee, 2003) in the USA. These techniques will be reviewed in Chapter 4, together with a status of the AGATA project. It is convenient, in the rest of this Chapter, to provide a brief review of the concepts and definitions regarding γ-ray detectors.

3.3 Gamma-Ray Detection

3.3.1 Introduction

A detector is a device which converts an absorbed quantum of radiation into an electrical signal. The ideal detector should provide, for every incoming photon, a signal proportional to its energy and the precise time of its arrival. This, of course, cannot be achieved in practice. Real detectors do not provide an output signal for every incoming photon (Knoll, 2000).

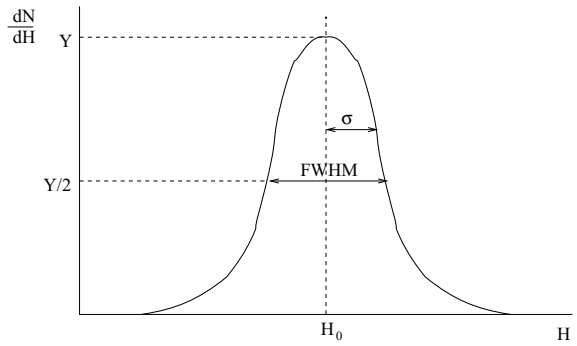


Figure 3.2 Definition of the energy resolution of a detector.

Accordingly, the *efficiency* of a detector can be defined as the ratio between the number of detected photons and the number of photons emitted by the source:

$$\varepsilon = \frac{detected\ photons}{emitted\ photons} \tag{3.1}$$

The *intrinsic efficiency* is defined as the ratio between the number of detected photons and the number of photons entering the detector:

$$\varepsilon_{int} = \frac{detected\ photons}{incident\ photons} \tag{3.2}$$

Due to the statistical nature of the processes in which the electrical signals are generated, real detectors do not provide a fixed amplitude signal for incoming photons of fixed energy. The *differential distribution of pulse height* $\mathrm{d}N/\mathrm{d}H$ is defined in a way that the total number of pulses with amplitude between H_1 and H_2 is:

$$N = \int_{H_1}^{H_2} \frac{\mathrm{d}N}{\mathrm{d}H} \cdot \mathrm{d}H \tag{3.3}$$

For fixed energy photons, this distribution will present a peak with nonzero width, centred at the value H_0 (Figure 3.2). The *resolution* of the detector is defined as:

$$R = \frac{\sigma}{H_0} \tag{3.4}$$

where σ is the width of the peak. Normally, the Full Width at Half Maximum (FWHM) of the peak is chosen instead of σ (Figure 3.2). The relationship between the two quantities is $FWHM = 2\sqrt{2ln2}\sigma = 2.355\sigma$

Real detectors do not provide signals at a fixed time with respect to the arrival of the radiation. A differential distribution of time pulses can be defined, where the time

pulse is the time interval between the pulse and a common "start" signal. The width of this distribution is usually taken as an estimate of the timing capabilities of the detector. A good detector should give signals at a fixed time with respect to the arrival of the photons, that is, the width of the time distribution should be small. This will be the case for detectors in which the signal is independent from the initial interaction point of the photon, that is for the *scintillators*. When the signal varies in shape depending on the position of the interaction point, as in *semiconductor detectors*, the collection times will vary greatly and the timing properties will be poorer.

3.3.2 Interaction of Photons with Matter

The microscopic processes in which charged and neutral particles release energy into matter are quite different. Charged particles release their energy continuously, interacting with the electrons of the stopping medium through the electromagnetic interaction. Neutral particles, as the neutron and the photon, release their energy in discrete steps, in which secondary charged particles are released and subsequently detected.

There are three main ways in which a photon with an energy in the range of interest for nuclear physics may interact with matter (Knoll, 2000), schematized in Figure 3.3:

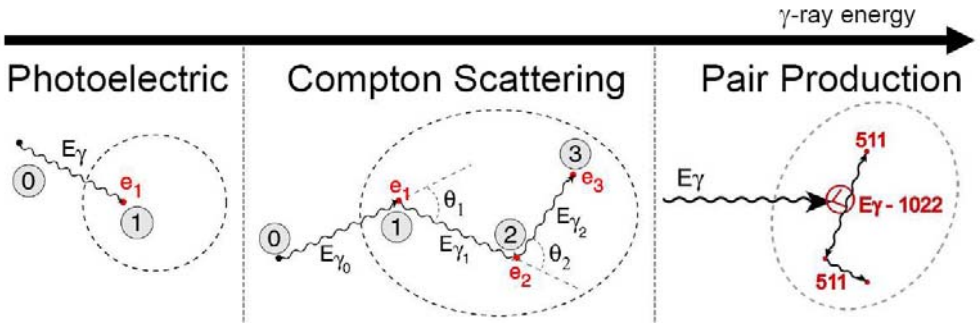


Figure 3.3 Three major types of γ-ray interactions

1. *Photoelectric effect*: the photon interacts with an atom, releasing all of its energy to one of the electrons. This *photoelectron* is emitted with energy $E_{e^-} = E_\gamma - E_b$, where E_b is the electron binding energy. Since normally the photoelectron comes from the inner shells, the excited ionized atom quickly de-excited emitting X-rays

or Auger electrons which are normally re-absorbed close to the emission site. Photoelectric effect is the dominant mode of interaction for relatively low-energy photons (below 100 keV); there is no analytic expression describing the probability of photoelectric absorption over all ranges of E_γ and Z, but, empirically (Evans, 1982),

$$\sigma \propto \frac{Z^n}{E_\gamma^{3.5}} \tag{3.5}$$

with $n \approx 4$–5: the probability of photoelectric absorption strongly increases with the atomic number Z of the material because of the increased electron density.

2. *Compton Effect*: an incident photon may transfer part of its energy to a free electron in an elastic scattering phenomenon, which is called the *Compton scattering*. The energy of the secondary photon E'_γ depends on its emission angle θ with respect to the direction of the incident photon of energy E_γ:

$$E'_\gamma = \frac{E_\gamma}{1 + \frac{E_\gamma}{m_e c^2}(1 - \cos\theta)} \tag{3.6}$$

The probability of Compton scattering per atom of the absorber increases linearly with Z, that is, with the number of available electrons; it decreases with increasing γ-ray energy.

3. *Pair production*: if a photon has an energy larger than twice the rest mass of an electron, it can interact in the electromagnetic field of an atomic nucleus and create electron-positron pairs. The probability for this kind of interaction is zero below $2m_e c^2 = 1.022$ MeV and stays low up to energies of several MeV, when it becomes the dominant mode of interaction. Roughly, the probability of pair production increases as the square of the atomic number Z of the absorber (Knoll, 2000).

3.3.3 Response Function

As a consequence of the various ways in which a photon may interact with matter, the response of a detector to incoming monoenergetic photons will normally be very different from the ideal differential pulse height distribution, which consists of an infinitely narrow peak centred at a value of H_0. Various features can be identified in a real spectrum, the most important of which are (Figure 3.4):

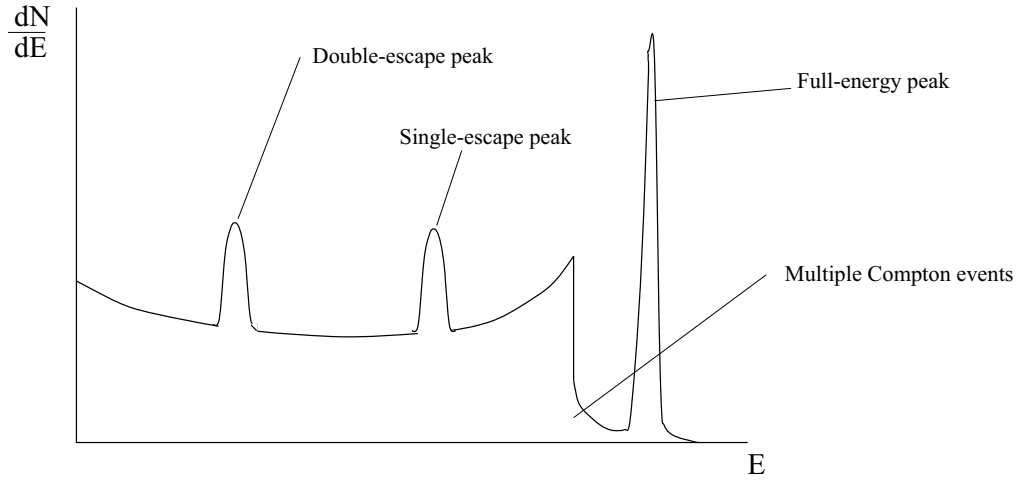


Figure 3.4 Schematic response function of a γ-ray detector.

1. *Full-energy peak*: this corresponds to events in which the photon released all of its energy inside the detector, directly (photoelectric effect) or through multiple-interaction events (for instance, a Compton scattering followed by photoelectric absorption of the residual photon).

2. *Compton continuum*: this corresponds to events in which the photon underwent Compton scattering without photoelectric absorption of the scattered photon. Neglecting events in which a photon is scattered two or more times, the continuum extends from zero energy to $E_\gamma - E_g$, where:

$$E_g = E_\gamma - E_{e^-}\big|_{\theta=\pi} = \frac{E_\gamma}{1 + 2E_\gamma/m_e c^2} \tag{3.7}$$

   In the limit of $E_\gamma \gg m_e c^2/2$, this reduces to $E_g \approx m_e c^2/2 = 0.256$ MeV. If multiple scattering events are considered, as it happens in practice, the Compton continuum extends up to the full-energy peak.

Other features of real spectra, such as escape peaks or the backscatter peak, are not important for the following, so they will not be described in detail.

An important parameter related to γ-ray detectors is the *Peak-to-Total Ratio* P/T:

$$\frac{P}{T} = \frac{N_{peak}}{N_{spectrum}} \tag{3.8}$$

where N_{peak} and $N_{spectrum}$ are respectively the number of counts in the full-energy peak and in the whole spectrum (working with monoenergetic photons). Since the events under

the Compton continuum do not allow to determine the energy of the incident photon, they are in practice an unwanted background, that can in many cases hide weak peaks. A good detector for γ-rays should therefore maximize the P/T ratio. This is essential in the case of multi-detector arrays.

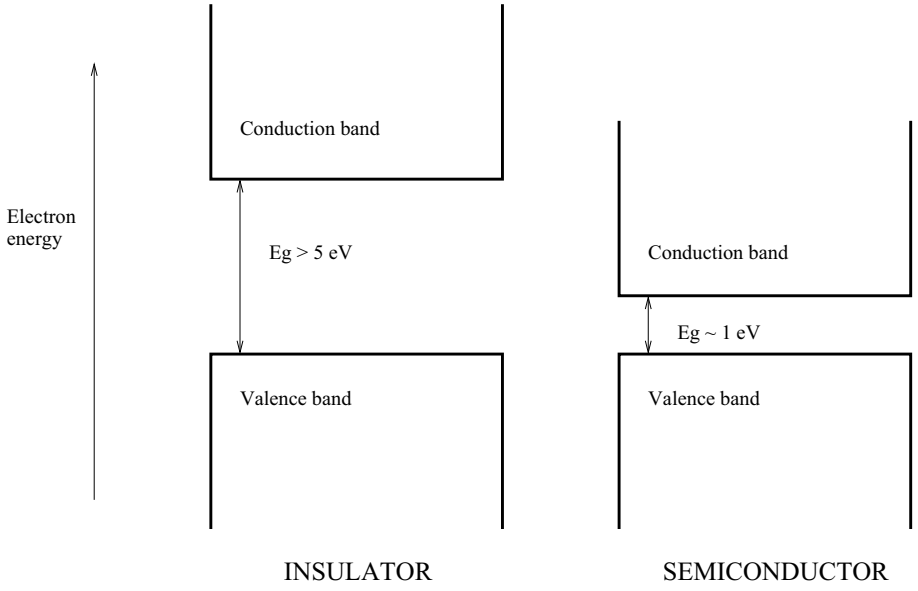


Figure 3.5 Band structure for electron energies in insulators and in semiconductors.

3.3.4 Bands in Solids

It is useful at this point to review some of the properties of crystalline solids, since they will be needed to describe the various classes of γ-ray detectors.

It is well known that electrons in crystals can occupy two discrete bands of energy (Figure 3.5). The lower band is called the *valence band* and is occupied by electrons bound at the lattice sites. As a result they cannot move across the crystal. The upper band is called the *conduction band* and is occupied by electrons that are essentially free to migrate across the crystal. The distance between the two bands is called the *bandgap* E_g.

In metals, the conduction band is partially occupied, and this explains the generally high conductivity of metals: small amounts of energy are required to displace an electron of the conduction band from one site to another inside the crystal. In insulators and semiconductors, the conduction band is almost empty, apart from electrons promoted

from the valence band through thermal excitation. The probability of thermal excitation depends critically on the temperature:

$$p(T) \propto T^{3/2} \exp\left(-\frac{E_g}{2kT}\right) \tag{3.9}$$

Typical values of the bandgap are $E_g \approx 5\,\text{eV}$ for insulators and $E_g \approx 1\,\text{eV}$ for semiconductors. At room temperature, it is almost impossible to excite electrons thermally in insulators, but it is quite probable in certain semiconductors (for instance, germanium). The absence of an electron in the valence band is called a *hole* and the promotion of an electron to the conduction band is equivalent to the generation of an *electron-hole pair*. Holes behave like positive charge carriers: very little energy is required to move an electron in the valence band and fill a hole, which will leave a hole behind. Since electrons move in opposite direction with respect to an applied electric field, the global effect is that holes move in the same direction as an applied electric field, just like a positive charge. Thus, electrons in the conduction band and holes in the valence band both contribute to the electrical conductivity of the material.

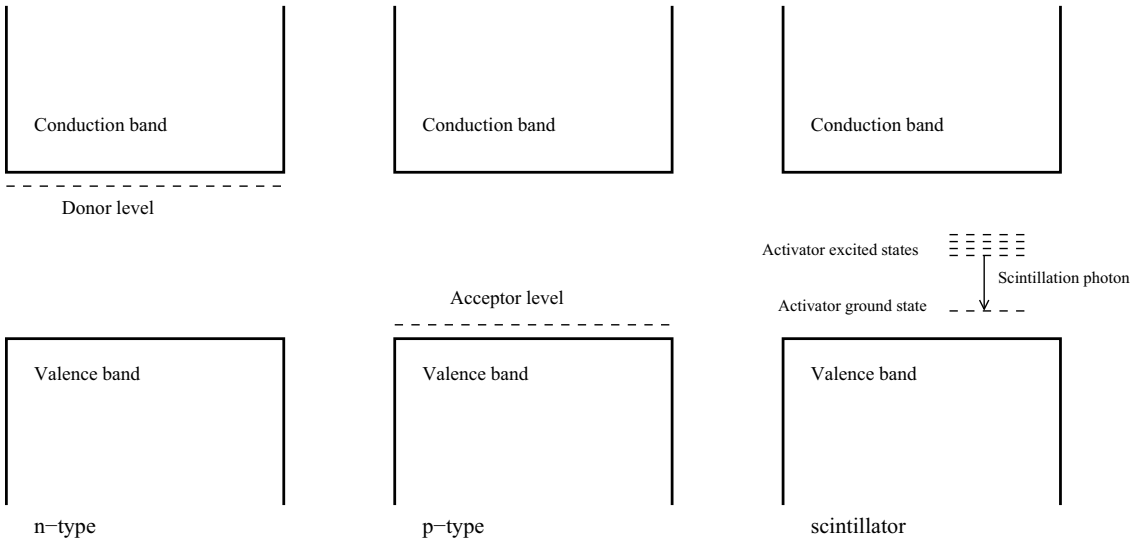


Figure 3.6 Band structure of a n -type crystal, of a p -type crystal and of an inorganic scintillator.

In a pure crystal (without impurities), free electrons and holes are produced thermally and therefore their concentrations are equal: $n_i = p_i$, where the subscript stands for *intrinsic*. Typical values in manufactured materials are $n_i \approx 2.4 \cdot 10^{13}\,\text{c}m^{-3}$ in germanium and $n_i \approx 1.5 \cdot 10^{10}\,\text{c}m^{-3}$ in silicon.

The presence of impurities (or *dopants*) deeply affects the electrical properties of a semiconductor (Figure 3.6). The most common semiconductor materials, silicon and germanium, are both tetravalent (that is, they possess four valence electrons). Adding a small concentration (a few parts per million, or less) of pentavalent atoms (for instance, phosphorus or arsenic) to the crystal, they will substitute for some atom in the lattice. These *donor* impurities have a valence electron more than the other atoms of the lattice, therefore this extra electron can occupy energy levels in the forbidden gap, close to the conduction band. It thus becomes easy to excite this extra electron thermally to the conduction band. Since $N_D \gg n_i$, the concentration of electrons in the crystal will be essentially equal to the concentration of donor atoms, $n \approx N_D$. Such an increased electron concentration leads to an increased pair recombination rate, so that the product of hole and electron concentration is equal to the value of the same product in the intrinsic material: $np = n_i p_i$. Assuming $N_D \approx 10^{17}\,\mathrm{c}m^{-3}$, it is clear that the concentration of electrons will be much larger than that of the holes: electrons will be the *majority carriers* and holes the *minority carriers*. The total number of charge carriers will be about $N_D \gg 2n_i$, that is, the electrical conductivity of the doped material will be much larger than that of the pure material.

A similar situation occurs if the impurities are trivalent *acceptor* atoms (boron or gallium), reversing the role of electrons and holes. The semiconductor is said to be of n-type in the former case, of p-type in the latter.

As mentioned before, in a pure crystal there are no states available for the electrons inside the gap. The arrival of a radiation quantum can generate one or more electron-hole pairs, which will later recombine. As a result of this process, photons may be emitted. However, since the energy of these photons corresponds to the bandgap, they will not be visible photons and they will have a rather high probability of absorption. To enhance the probability of visible light emission, impurities are normally added to the crystal. The atoms of such impurities (called *activators*) create energy levels inside the forbidden gap. Therefore, it will be possible that an electron excited to the conduction band decays to the valence band through intermediate steps involving the activator energy levels. Since now the distance between the band and these levels is lower than the bandgap, the emission of visible photons becomes possible. In this case, the crystal is said to be a *scintillator*. The

energy of the emitted photons is lower than the bandgap, therefore they cannot generate electron-hole pairs and the scintillator is transparent to the scintillation light. It must be mentioned that in some crystals the emission of visible photons does not involve activator atoms. This is the case, for example, of the Bismuth Germanate $Bi_4Ge_3O_{12}$ (Knoll, 2000).

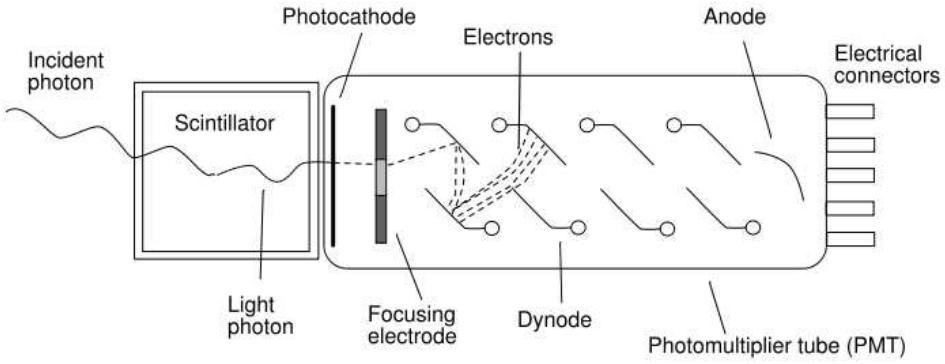


Figure 3.7 Basic elements of a photomultiplier tube.

3.3.5 Inorganic Scintillators

The first class of γ-ray detectors that we are going to describe in some detail is composed of *inorganic scintillators*. These materials emit visible photons following the interaction with radiation. The visible photons can subsequently generate an electric signal through devices called *photomultiplier tubes* or through *photodiodes*.

An important parameter to determine the performance of a scintillating material is the *light output*, that is, the number of emitted photons per unit of incident energy. Not all of the energy released in the scintillator will generate a light output: in many cases the recombination of the pairs occurs through non-radiative processes (*quenching*). The materials with larger light output will usually provide a better energy resolution, since the statistical fluctuations in the number of photoelectrons will be smaller.

The most common scintillating materials used for γ-ray spectroscopy are the alkali halides, in particular NaI(Tl) (Sodium Iodide (Thallium)), BaF_2 (Barium Fluoride) and CsI(Tl) (Cesium Iodide (Thallium)). NaI represents the standard against which almost all

of the detectors are compared in γ-ray spectroscopy, due to its excellent light output and to its relatively high density, which leads to very good detection efficiency.

Another material in widespread use is the *Bismuth Germanate* $Bi_4Ge_3O_{12}$, known simply as BGO. Its light output is relatively poor compared with NaI(Tl), but its high density and the presence of bismuth high-Z atoms makes it an excellent scintillating material in all of the situations in which high efficiency and compactness are required.

There are also *organic scintillators*, in which the emission of visible photons is a consequence of the electronic structure of the single molecule, rather than of the structure of the crystal as a whole, but these materials are generally not used for γ-ray detection due to low densities and low light outputs.

The conversion of the emitted photons into an electric signal is generally achieved through a photomultiplier or a photodiode. The functioning of a photodiode is very similar to that of a conventional junction semiconductor detector, which will be described in the following subsection, so we will not enter here into any detail. It is instead useful to describe the structure of a photomultiplier tube (Figure 3.7). The scintillation photons are absorbed by a *photocathode*, which emits electrons following the absorption. These *photoelectrons* are accelerated by a series of electrodes, called *dynodes*, at increasing electrical potential. Each electron that strikes a dynode produces other secondary electrons, that are also accelerated. The result of this *multiplication* process is that the charge collected at the anode is usually orders of magnitude larger than the charge originally produced in the scintillator. Currents of the order of 1 mA are reachable.

Since the paths followed by the photoelectrons are very similar, generally the timing properties of a scintillator crystal coupled to a photomultiplier are good, reaching a time resolution of the order of a few nanoseconds. On the other hand, the process of charge production involves many inefficient steps, generating first electron-hole pairs, then scintillation light and in the end photoelectrons. Ultimately, the resolution is determined by the fluctuations in the number of photoelectrons coming out of the photocathode. Typical resolution values are of the order of 10% for the 1332 keV line of ^{60}Co.

3.3.6 High-Purity Germanium Detectors

State-of-the-art γ-ray spectroscopy is performed using High-Purity Germanium (HPGe) detectors. These detectors generate the electric signal directly, without using a transducer like a photodiode or a photomultiplier. It is useful to understand the processes involved in more detail.

The basis of modern solid state detectors is the *p-n junction* (Figure 3.8). A junction is formed by putting in thermodynamic contact a *p*-type and a *n*-type crystal. Putting in contact two separate crystals will not suffice, the methods to form a junction start normally from an *n*-type crystal in which one face is exposed to vapours of acceptor type or is bombarded with ions (the so-called *ion implantation* technique).

At the junction, charge carriers find an abrupt discontinuity in their concentration. Therefore, electrons will migrate from the *n*-type zone to the *p*-type, to combinate with holes, and holes will migrate from the *p*-type to the *n*-type zone, to combinate with electrons. As a result of this migration-recombination process, immobile positive ions (the ionized donor impurities) remain in the *n*-type zone, and immobile negative ions (the acceptor impurities after capturing an electron) remain in the *p*-type zone. A zone in which there are no free majority carriers is formed, which is called the *depletion region*. The space charge in the depletion region creates an electric field (*contact electric field*) that diminishes the tendency for further charge diffusion (Figure 3.9).

The depletion region appears promising from the point of view of radiation detection: any electron-hole pair formed by the arrival of radiation will feel the contact electric field, which means that charges will migrate to the borders of this region, where it will be possible to collect them. The contact electric field, however, is of the order of 1 V, therefore the migration velocity of the charge carriers will be low and the probability of recombination will be high.

Normally, the depletion region extends for a very limited distance (of the order of a few microns), therefore the probability that a radiation quantum will interact with it will be rather low. However, it is possible to apply an external electric field to both sides of the junction. If the *p*-side is put at higher potential than the *n*-side, the external electric field will oppose to the contact electric field, and only small values of applied voltage will be required so that the junction may conduct large currents: the junction behaves like a

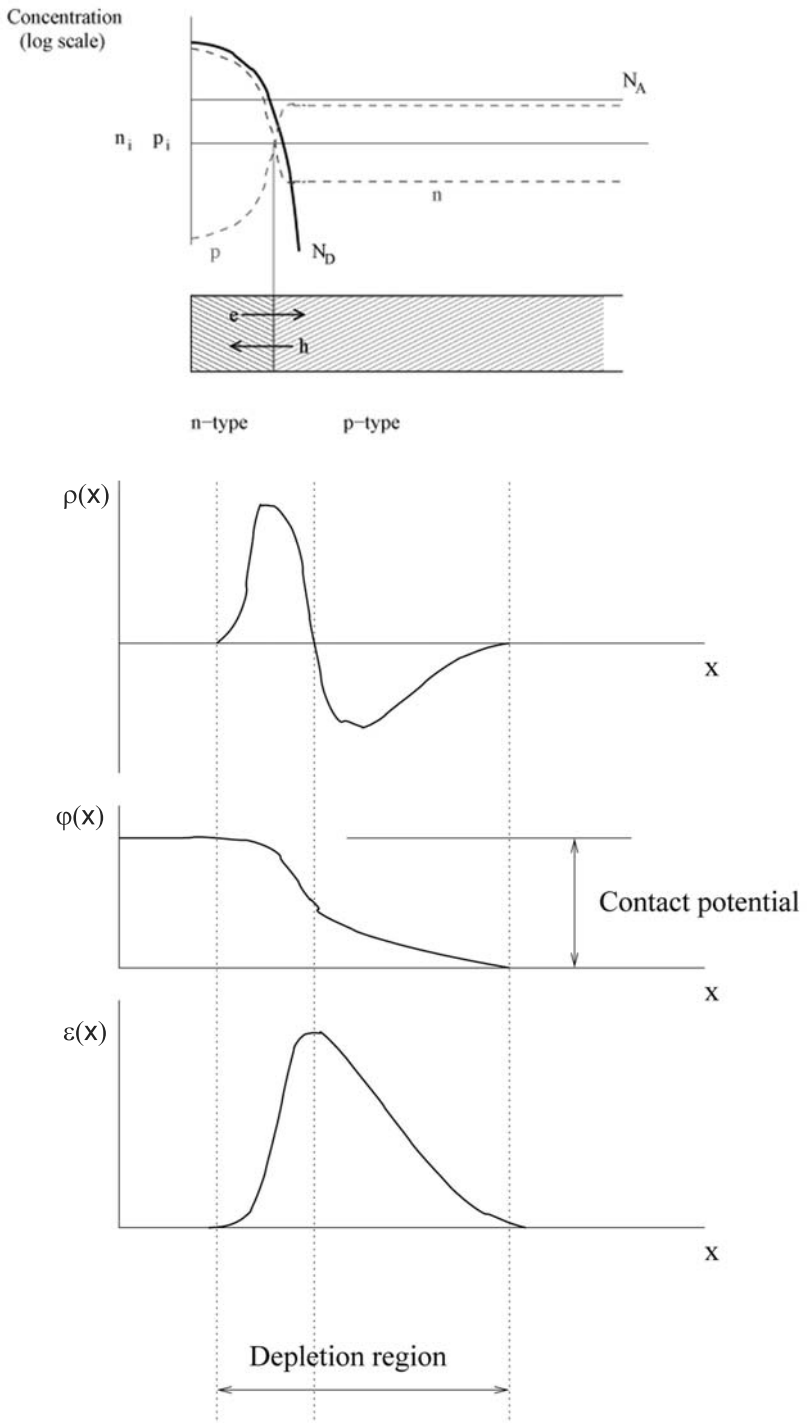


Figure 3.8 The assumed concentration profiles for the *n*-*p* junction. The effects of carrier diffusion across the junction give rise to the illustrated profiles for space charge $\rho(x)$, electric potential $\varphi(x)$ and electric field $\varepsilon(x)$ Knoll (2000).

forward biased diode. If instead the *n*-side is put at higher potential than the *p*-side, the external electric field will add to the contact electric field. This will cause other electrons

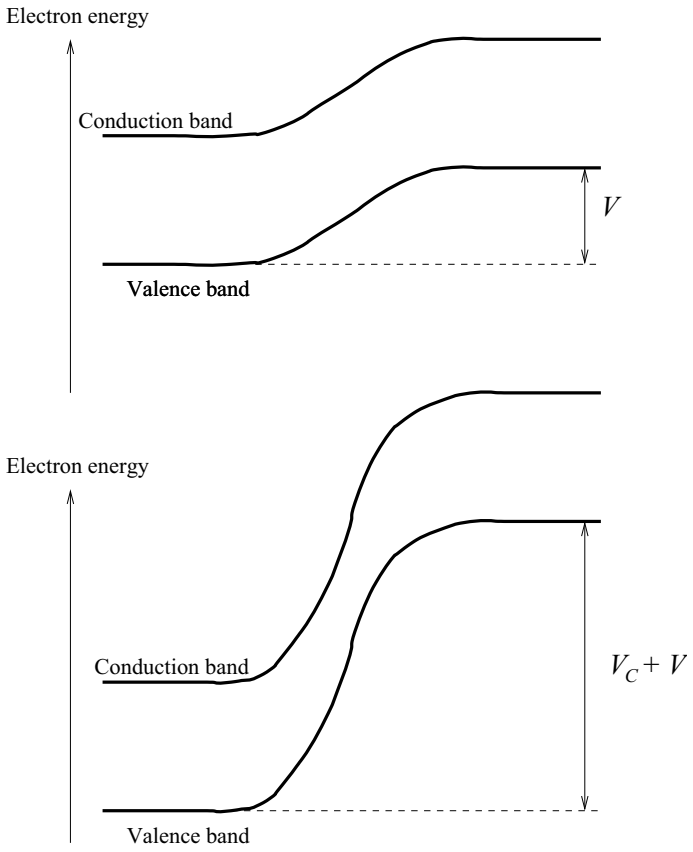


Figure 3.9 The variation in electron energy bands across a junction without (top) and with (bottom) an applied reverse bias V (Knoll, 2000)

to migrate from the n-side to the p-side and holes from the p-side into the n-side. The depletion region will extend gradually with increasing applied reverse bias. If the applied bias becomes too large, a destructive breakdown will happen generally, with a sudden increase in the reverse current.

The extended depleted region can be a very good detector: since there are no majority carriers and only a few minority carriers, the steady reverse current will be very low (implying that the resistivity of the depleted region is very high); any majority carriers produced by the interaction of radiation inside the depletion region will quickly migrate to its borders due to the applied external electric field. Eventually, if the crystal is not too large it may become fully depleted.

Normally, germanium is the semiconductor used for γ-ray detectors. Its atomic number is larger than that of the silicon, which gives it a higher photopeak efficiency and hence a higher detection efficiency. Comparison of silicon and germanium properties can be seen in Table 3.1. The best material produced presents a concentration of impurities

Table 3.1 Properties of Intrinsic Silicon and Germanium (Bertolini and Coche, 1968).

	Si	Ge
Atomic number	14	32
Atomic weight	28.09	72.60
Stable isotope mass numbers	28-29-30	70-72-73-74-76
Density (300 K); g/cm^3	2.33	5.32
$Atoms/cm^3$	4.96×10^{22}	4.41×10^{22}
Forbidden energy gap (300 K); eV	1.115	0.665
Forbidden energy gap (0 K); eV	1.165	0.746
Intrinsic carrier density (300 K); cm^{-3}	1.5×10^{10}	2.4×10^{13}
Energy per electron-hole pair (300 K); eV	3.62	
Energy per electron-hole pair (77 K); eV	3.76	2.96

of the order of $10^{10}\,cm^{-3}$, corresponding to 1 part over 10^{12}; it is called High-Purity Germanium, HPGe. Present technology allows the growth of rather large crystals (cylinders of the order of 8 cm diameter and 12 cm length) that can be fully depleted. This is still much smaller than we would like in the ideal case. Another major disadvantage in operating with germanium crystals is that, due to the low value of the bandgap ($E_g \approx 0.8$ eV), they have to be kept at liquid nitrogen temperature (77 K) in order to keep the probability of thermal pair generation at reasonably low values. This operational disadvantage is largely compensated by the excellent resolution achievable. Best resolution values are of about 2 keV for the 1332 keV line of the ^{60}Co source, compared to values of the order of 100 keV achievable with a NaI(Tl) scintillator coupled to a photomultiplier tube. This is because of the statistical nature of the process. The energy ε to produce a charge carrier in a HPGe crystal is much lower than in a NaI(Tl) crystal coupled to a photomultiplier, since in the latter case the process involves inefficient, low-statistics steps which dominate the final statistical fluctuation. Typical values of ε are about 3 eV in a germanium crystal and 100 eV in a scintillator + phototube system. On the other hand, the timing properties of HPGe detectors are rather poor, since in big crystals the charges may be produced in rather distant points, implying quite varying collection times.

Typical efficiency values for HPGe detectors are not very high, compared to the typical values for scintillators. The efficiency standard is a $3'' \times 3''$ NaI(Tl) crystal, coupled to a phototube, positioned at 25 cm from the source. Larger efficiency values can be reached

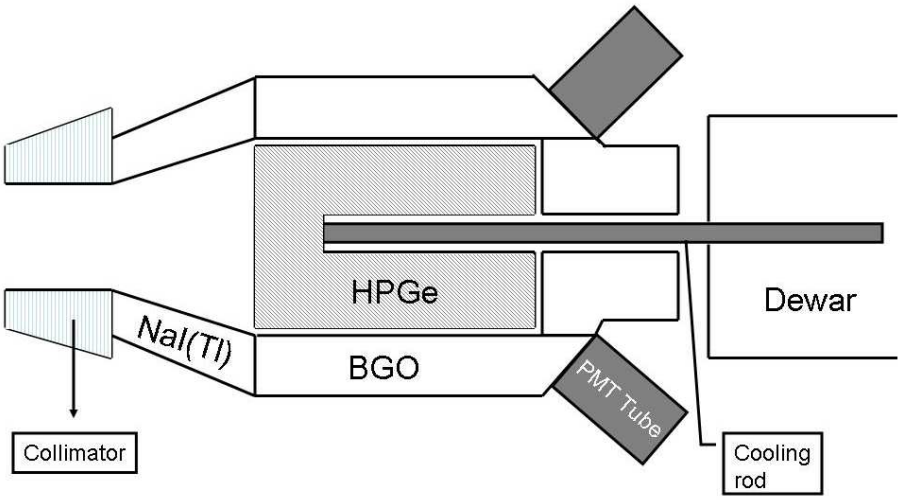


Figure 3.10 Basic elements of an anti Compton shield.

using composite detectors, that is, summing together the signals of two or more crystals.

The major problem in using HPGe detectors is that the atomic number of germanium ($Z = 35$) is not high enough to ensure a good probability of photoelectric absorption even at rather low energies. The atomic number of iodine is $Z = 53$ and therefore photoelectric absorption is far more probable in NaI(Tl) scintillators. The dominant mode of interaction in HPGe crystals is Compton scattering, implying that the larger fraction of the events will not generate a useful signal, but will simply form part of the background. Typical values of P/T for commercial detectors are of the order of 0.2–0.3. Such values are low in themselves, but this situation is worsened when *coincidence spectra* are taken, that is, when two or more detectors are operated and signals are taken under the extra condition that at least two detectors fire within a fixed time window. Requiring the coincidence between two detectors, the P/T ratio in the coincidence spectrum will simply be the square of the P/T ratio for a single spectrum. Assuming $P/T \approx 0.2$, it will be $(P/T)^2 \approx 0.04$, that is, only 4% of the events will be useful for the analysis. The situation grows dramatically worse for higher-order (or *higher-fold*) coincidences.

The common solution to these problems relies on the use of *anti Compton Shields* (Figure 3.10). The HPGe detector is almost completely surrounded by a highly efficient detector that is shielded from the direct source of radiation, using a high-Z collimator. Normally, NaI(Tl) will be used if there are no space restrictions, while BGO is preferred

when compactness is needed, for instance, in the modern arrays of many HPGe detectors. If the shielding is effective enough, the scintillator will see radiation only when an interaction occurs in the HPGe crystal that does not contribute to the full-energy peak, that is, when photons escape from the HPGe crystal. It is clear that, requiring an *anticoincidence* between the scintillator and the germanium, it is possible to get rid of most of the events that would have formed unwanted background. In this way it is possible to reach P/T values of the order of 60%, which allow the analysis of multiple-fold spectra with reasonable statistics.

4. The AGATA PROJECT

In this chapter the principles of γ-*ray tracking* and *pulse shape analysis* will be presented. The status of the AGATA project, aiming at the construction of an array based on such technologies, will be reviewed.

4.1 Arrays of Germanium Detectors

New discoveries in the field of γ-spectroscopy are often triggered by the improvement of the detection devices. Following early works with inorganic scintillators, such as NaI(Tl), high-resolution γ spectroscopy was made possible by the development of solid-state detectors, in particular Ge(Li) and HPGe crystals. The early stage of this technology, the volume of these crystals was limited to a few cm^3, resulting in low photopeak efficiencies (10-20% relative efficiency). Even with larger HPGe crystals (60–80% relative efficiency), the relatively low atomic number of germanium results in P/T ratios of the order of 30% for a single crystal. In order to improve the P/T ratio, the most common solution was, as discussed in Chapter 3, to use an anti Compton shield. Through the use of an anti Compton Shield, sketched in Figure 4.1, values $P/T \simeq 50-60\%$ can be reached as shown for instance in Figure 4.2.

The next breakthrough in the field of γ spectroscopy occured at the end of the 1980s with the use of arrays of germanium detectors with anti Compton shields (or Compton-Suppressed Spectrometers). These devices have later become kind of standard tools and many valuable results have been obtained with devices such as GASP (Rossi-Alvarez, 1993; Bazzacco, 1992), EUROGAM (Beausang et al., 1992), EUROBALL (Simpson, 1997; Rossi Alvarez, 1998) and GAMMASPHERE (Deleplanque and Diamond, 1988; Lee, 1990). It is apparent that the future developments as well will rely on arrays of HPGe detectors and therefore it is convenient here to provide methods to properly characterise these devices.

The quantity characterising multi-detector arrays is known as the *resolving power* of the array. The expression of the resolving power R is:

$$R = \left(\frac{SE_\gamma}{\Delta E_\gamma} \frac{P}{T} \right) \tag{4.1}$$

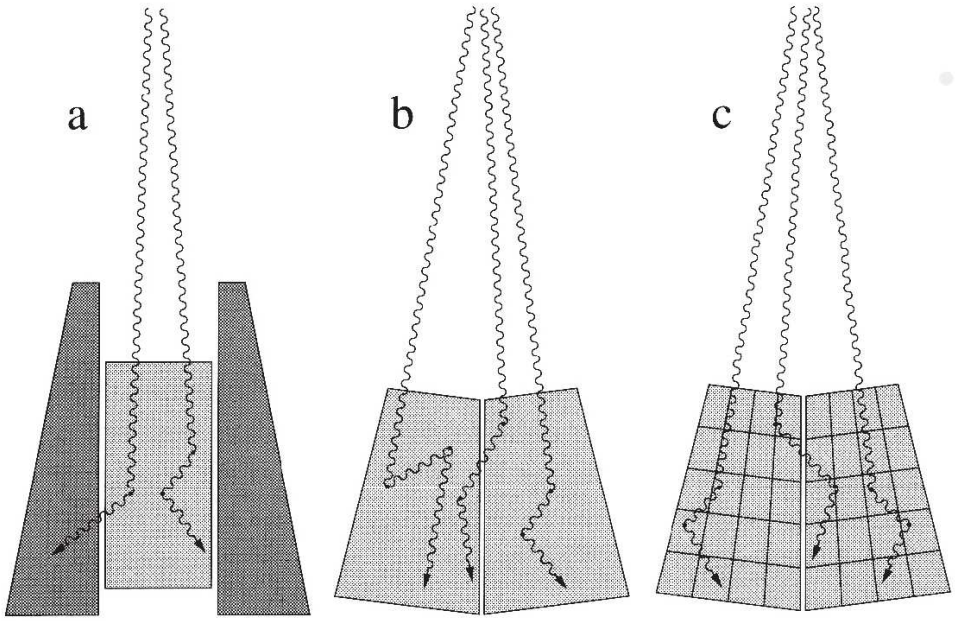


Figure 4.1 The Figure is showing (a) the basic idea of how the Compton-suppression shield surrounding an individual Ge detector works, (b) how signals from Compton scattered events detected in various parts of a composite detector can be added together and (c) the idea of γ-ray tracking, section 4.2 (Julin, 2005).

where SE_γ is the average separation of the γ-ray peaks in the spectrum, P/T is the peak-to-total ratio and ΔE_γ is the effective energy resolution of the detector. Thus, the resolving power is proportional to the P/T ratio in the spectra and inversely proportional to the effective energy resolution of the detectors.

We can have a look at some numbers to get an idea of what has been reached so far. The EUROBALL array (Simpson, 1997; Rossi Alvarez, 1998) was composed of 239 crystals, resulting in a photopeak efficiency $\varepsilon_{ph} \approx 9\%$ and in a $P/T \approx 60\%$. In this case $R \approx 9$ was achieved.

It is clear that in developing an array of HPGe detectors a careful balance must be found between two contrasting needs. In order to keep the effective energy resolution to acceptable values, the detectors should be placed at large distances from the target. This implies that a very large number of crystals might be needed in order to obtain the desired detection efficiency. The mere presence of the Compton-suppression shields limits the solid angle where the high-resolution detectors could be placed and therefore the maximum attainable detection efficiency. A partial solution to this problem consists in

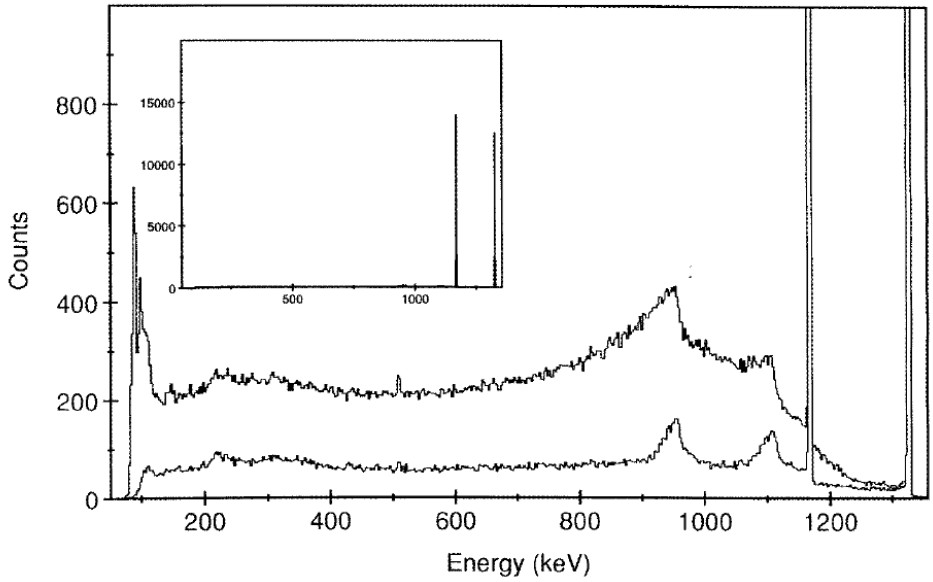


Figure 4.2 Unsuppressed and suppressed spectra of ^{60}Co (Beausang and Simpson, 1996)

using composite detectors, namely more crystals sharing the same cryostat and the same Compton-suppression shields. Efficiency and peak-to-total can be recovered by summing (adding back) the energy deposited in neighbouring crystals. Examples of composite detectors are the Clover (Duchêne et al., 1999) and the Cluster (Wilhelm et al., 1996) developed within the EUROBALL Collaboration.

Taking this process to its extreme, we could conceive an array composed solely of germanium detectors and perform Compton suppression through some "intelligent" add-back as depicted in Figure 4.1-b. The results from Monte Carlo simulations (Gerl and Korten , 2001) suggest that thousands of crystals would be needed to obtain a photopeak efficiency of the order of 25-30% and keep the effective energy resolution to acceptable values. As a matter of fact, the P/T ratio of such an array would be approximately 30%, hence obtaining a resolving power no larger than the EUROBALL array.

Similar conclusions were drawn considering more compact arrays composed of electrically segmented crystals similar to those developed for MARS (Kröll and Bazzacco, 2001), MINIBALL (Warr et al., 2003), SeGA (Mueller et al., 2001) or EXOGAM (Shepherd et al., 1999). It is thus clear that new techniques should be developed to obtain an array with photopeak efficiency larger than 30%, $P/T \approx 60\%$ and effective energy resolution better than 1%. These techniques imply using the detectors in a "smart" way as

depicted in Figure 4.1-c.

Research and development on these new techniques, namely γ-*ray tracking* and *pulse shape analysis*, is being carried out since the mid nineties. Presently two projects, AGATA in Europe (Gerl and Korten , 2001) and GRETA in USA (GRETA Steering Committee, 2003), aim at the construction of an array of highly-segmented HPGe detectors based on these techniques, which will be briefly reviewed in the following sections.

4.2 The γ-Ray Tracking Principles

As it has been outlined in Chapter 3 the interaction of photons with matter is quite different than the interaction of charged particles. Charged particles deposit their energy through a continuous ionisation track. On the other hand, the distance of gamma ray interaction points inside an HPGe detector are of some cm or less and the time resolution of such a detector is of some ns, Therefore the different interaction points are seen as simultaneous.

In principle, if the individual interaction points are known with sufficiently high precision, the scattering sequence of each photon could be disentangled and followed (tracked).

The algorithms performing γ-*ray tracking* must take into account both the physical characteristics of the interaction mechanisms of γ-rays and the geometry of the detector. As discussed in Section 3.3, in Nuclear Spectroscopy the energy range of interest is from 10 keV to a few tens of MeV and the main interaction mechanisms that a photon can undergo in a solid state detector are restricted to photoelectric absorption, Compton scattering and electron-positron pair production. The relevance of each interaction mechanism as a function of energy is depicted in Figure 4.3.

Figure 4.3 shows that the most probable interaction for a photon in germanium is Compton scattering. Typically, a γ-ray releases its energy in 3 or 4 places within a detector by two or three Compton scattering and a final photo-absorption. The energy of the scattered photons can be calculated by using the Compton scattering formula Eq. 3.6.

In principle a γ-ray tracking algorithm should check which of the possible sequences within a set of points is compatible with the Compton scattering formula. This is not feasible, in practice, in case of high-multiplicity events because of the computational requirements. It should be reminded that the mean free path in germanium of photons with

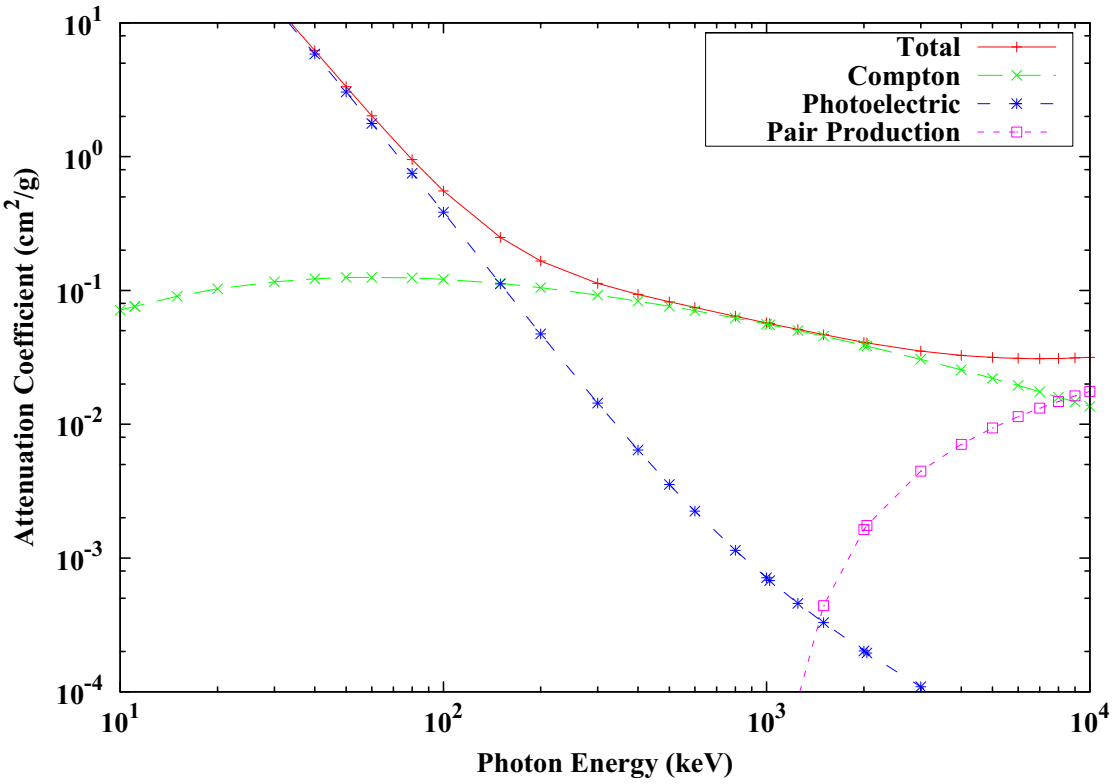


Figure 4.3 γ-ray attenuation coefficients for Compton, Photoelectric and Pair Production interactions in Germanium material as a function of γ-ray energy (Berger et al., 1998).

an energy around 1 MeV is approximately 3 cm, hence one order of magnitude smaller than the dimension of the full array. It is therefore expected that the interaction points generated by a single photon will be localised in a small portion of the spectrometer. In other words, clusters of interaction points generated by the same photon can be identified through several techniques, based either on angular proximity or on linear proximity, taking into account the amount of material in between the interaction points.

Actually, two alternative approaches are possible to follow the γ-ray path: forward tracking (Schmid et al., 1999; Piqueras et al., 2004) algorithm and back tracking algorithm (Milechina and Cederwall, 2003; van der Marel and Cederwall, 1999, 2002).

Forward tracking is the approach followed with the GRETA Collaboration (Schmid et al., 1999) as well as in the Orsay Tracking code (Lopez-Martens et al., 2004) and in the Mars Gamma Tracking (mgt) code developed earlier in Padova (Bazzacco, 2004). The mgt code was used to calculate the overall performance of the AGATA array. The agreement of each possible scattering sequence with the scattering formula is evaluated

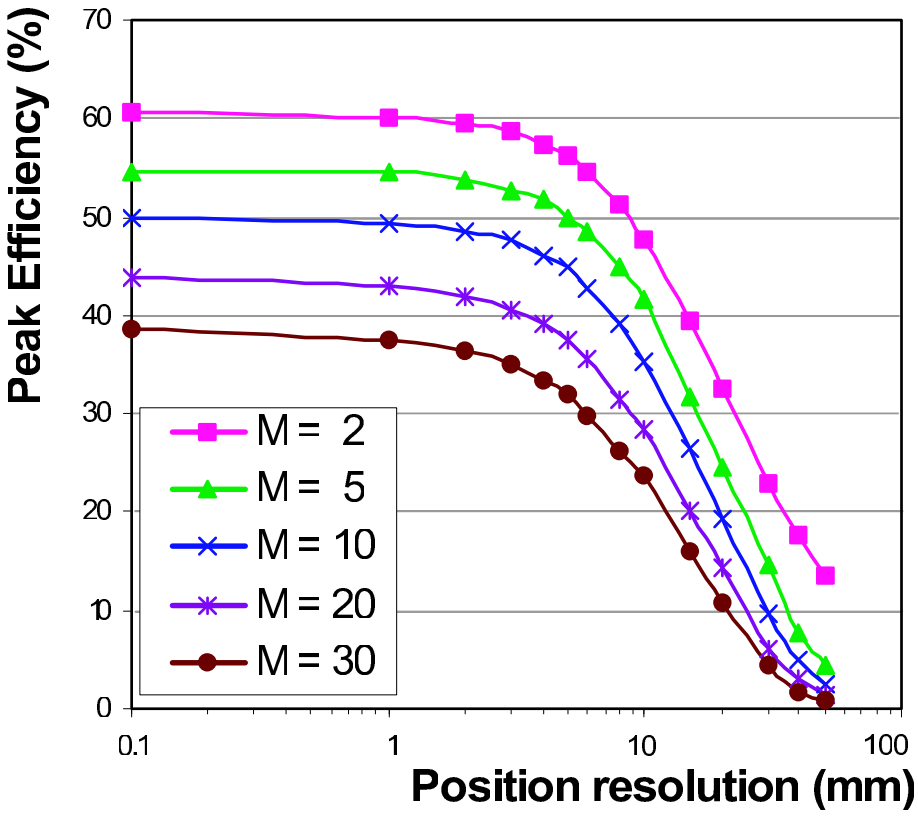


Figure 4.4 Photopeak efficiency of an ideal germanium shell for 1.332 MeV photons as a function of the position resolution. Tracking is performed. The different colours give the performance for different photon multiplicity.

assuming a given origin for the photons. The probability that a photon could cross a given amont of material without interacting is taken into account, as well as the probability of Compton scattering and the total interaction cross section. The pattern of energy deposition following pair production is quite characteristic, thus making it possible to identify such events. The interaction points not corresponding to a scattering sequence nor to pair production are tested for photoelectric absorption according to the traveling path inside the detector.

The alternative back tracking approach relies on the empirical observation that the energy deposition in a photoelectric interaction usually lies within a narrow energy band between 100 and 250 keV. The idea is to identify a candidate for a photoelectric absorption point and then to reconstruct a track back to the point of origin of the photons.

So far, the existing tracking algorithms have been developed on the basis of simulated data sets. The plot of Figure 4.4 gives the photopeak efficiency of the ideal germanium

shell. It was assumed to localise the individual interaction points with different position resolution and to perform γ-ray tracking. It is clear that in order to obtain photopeak efficiencies close to the limiting values (obtained with zero positional error) the interaction points should be measured with a precision of a few millimetres at most. This means that techniques to identify the interaction points at sub-segment precision should be developed. These techniques are briefly discussed in the next section.

4.3 Pulse Shape Analysis (PSA)

The Pulse Shape Analysis is one of the fundamental features of the gamma ray tracking detector arrays. The performance of the AGATA is strongly related to the capacity of the position determination within a few mm. The task of the PSA algorithm is to extract the position and energy of each interaction point of the detected event.

The basic idea is that, following an interaction within the crystal, the drifting motion of the charges induces a signal not only in the segment where the interaction took place, with a non-vanishing integrated current over the collection time, but also in the neighbouring segments. The main difference is that the integrated current in these segments is vanishing, in other words these signals are transient. Since their amplitude depends on the location of the primary interaction, this information can be used to determine such a position. For instance, in Figure 4.5 a 36-fold of AGATA detector is considered. A photon deposited energy in segment A4 and C6, inducing transient signals in the neighbouring segments. The interaction which takes place in A4 is producing transient signal in A3-A5-B4 and B5 while the other interaction is producing in B5-B6-C4-C5-D5 and D6. The signal in the segment B5 is the results of the overlap of two transients. From the amplitude of the transients a first estimation can be made about the places of the interaction points. For example the interaction which takes place in C6 produce higher transient in B6 and C5 than D5 and D6, which mean the interaction take place in the left down corner of the C6.

These intuitive observations are made quantitative by calculating the expected pulse shapes for specific detector geometry. This is based on the knowledge of the electric field produced by the applied high voltage and the parametrization of the mobility of the charge carriers (Kröll and Bazzacco, 2006; Bruyneel et al., 2006). Due to the irregular shape of

the crystals, the electric field has to be calculated numerically over the whole crystal. The transport of the charge carriers from a given starting point to the collecting electrodes is also performed numerically and the shape of the signal is given by the charge induced on the collecting electrodes and (for the transients) on all the other segments during the transportation time. The calculation of expected shapes can be performed systematically over a fine grid of starting points inside the crystals and the resulting data set is known as the "signal basis".

PSA identifies the starting point of a specific experimental signal by comparing its shape with all the shapes of the signal basis and by selecting the one that fits best.

This search is rather simple for single-interaction events but becomes much more difficult for events with more than one interaction in the same crystal, in particular if the multiple interactions are close to each other and their charge is collected in the same segment: on the average, a 1 MeV γ-ray interacts three times in the same crystal. The PSA algorithms cannot proceed like in the single–interaction case because unrealistic amounts

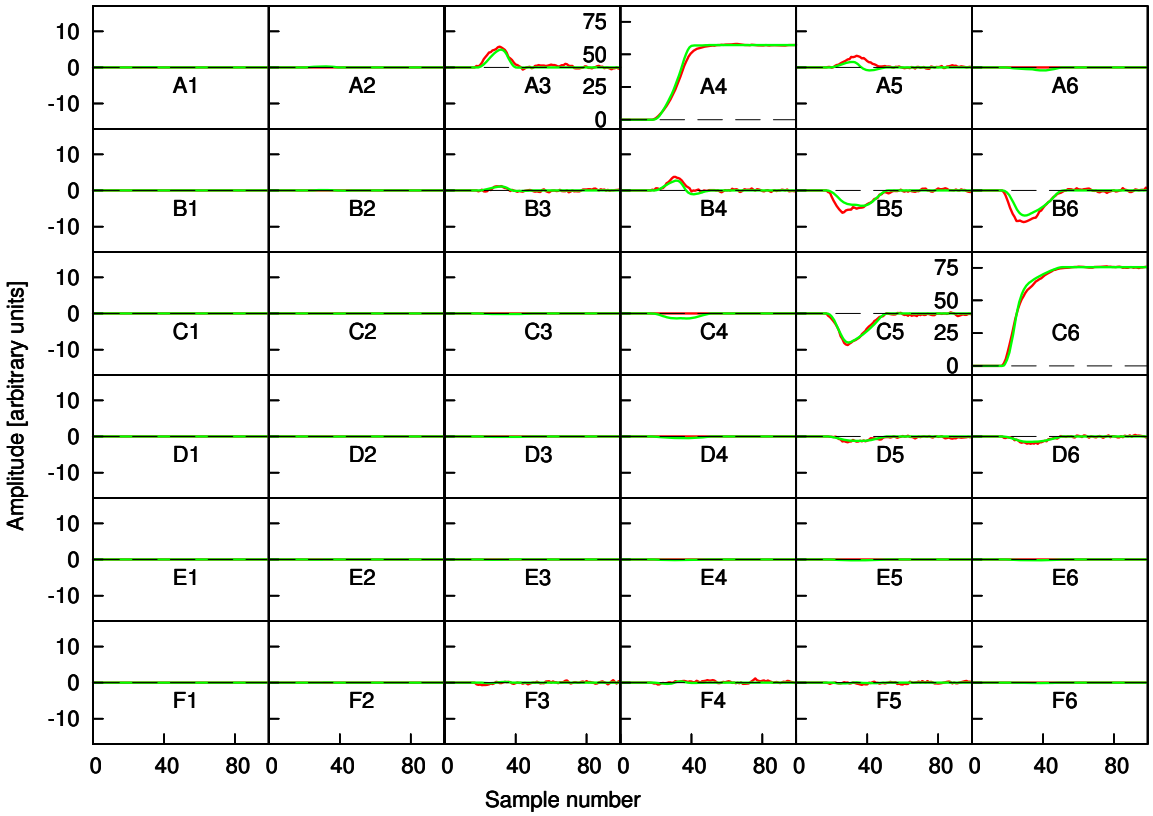


Figure 4.5 Net charge signals in segments A4 and C6 are producing transient signals in the neighbour segments. The interaction points can be determined by the PSA algorithms. The real signal is shown in red while the PSA signal from a grid search algorithms is shown in green lines.

of CPU power will be needed. This is proportional to the number of comparisons that have to be made for each event. Let's consider this problem for double interaction, using a 3D grid with a typical step of 2 mm. The resulting number of points is $\sim 10^3$ per detector segment and consequently 10^3 comparisons have to be made for a single interaction event. If the problem is not seperable into 2 independent search for the case of a double–interaction event in two different segments, the number of comparisons is 10^6 because all possible positions for the first interaction must be combined with all possible positions for the second interaction. The situation is more complicated if the two interactions are in the same segment because one needs also to test all possible partitions of the energy between the two partners.

To keep the analysis time to an acceptable level special signal decomposition techniques have been developed over the years (AGATA-Collaboration, 2007). The method which will be implemented in the initial phase of the AGATA project is a simple grid search (Venturelli and Bazzacco, 2005), which assumes that there is at most one interaction per segment and decomposes multi–segment events into separate single–segment ones. With this algorithm, it has been possible to obtain a position resolution of approximately 4 mm FWHM for 1380 keV photons (Recchia, 2008), which is consistent with the parameters used to estimate the overall performance of the array with the Monte Carlo (MC) simulations.

4.4 Review of the AGATA Project

The AGATA project has been proposed by an European collaboration to construct a 4π spectrometer based on γ-ray tracking and PSA as outlined in section 4.2 and 4.3. Such an array will be suitable for Nuclear Structure studies at the planned radioactive ion beam and high-intensity stable beam facilities. The design goals for the array can be summarised as follows (Gerl and Korten , 2001):

- efficiency larger than 40% for events with a photon multiplicity 1 and larger than 25% for events with a photon multiplicity 30,
- P/T ratio around 60%,
- position resolution better than 5 mm FWHM for the single interaction point,

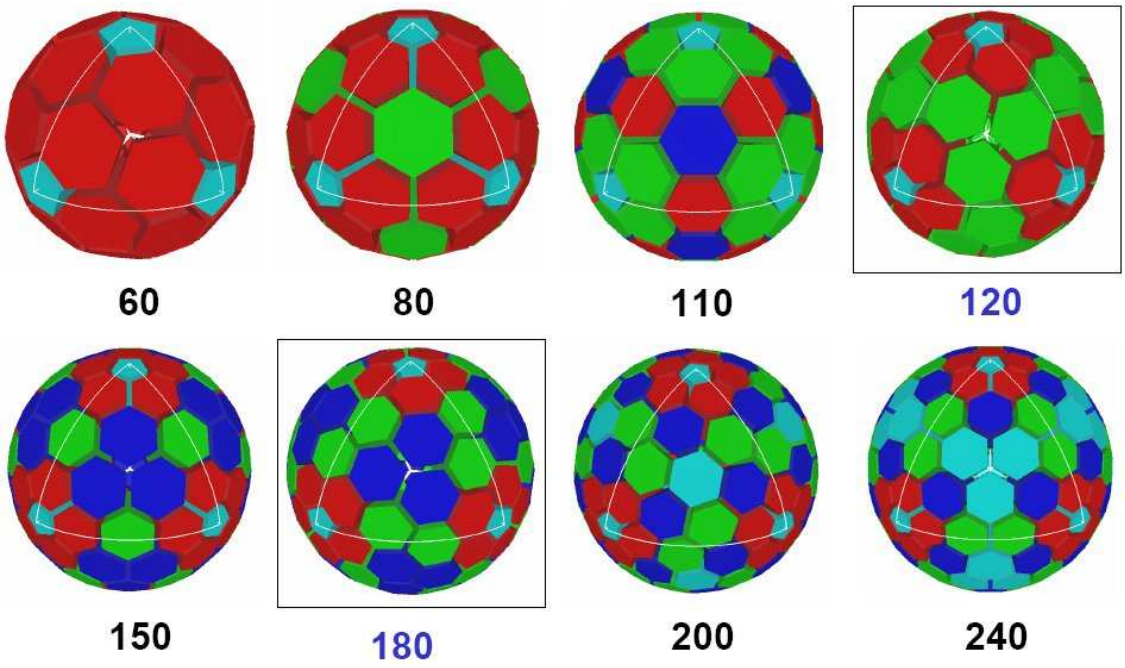


Figure 4.6 The investigated configurations. The light blue triangle reflects the underlying icosahedral structure that defines the 20-fold symmetry of the construction (Farnea, 2004).

- capability to stand a counting rate up to 50 kHz for each germanium detector when used with high intensity stable beams,
- enough internal free space to host ancillary detectors.

As a consequence of the tracking process, the AGATA array will have as well:

- high efficiency for high-energy γ-rays;
- capability to measure the polarisation of the detected photons.

The high photopeak efficiency values required to the AGATA array can be obtained only by covering almost the full 4π solid angle with germanium detectors. The amount of passive materials can be reduced by grouping more crystals, for instance three or four, inside the same cryostat. In order to increase the reliability of such complex objects, it was decided to use encapsulated detectors, namely detectors hermetically sealed inside an aluminium can, similarly to the EUROBALL cluster detectors (Wilhelm et al., 1996).

Using a few crystal shapes, the solid angle coverage can be maximized in an elegant way by projecting the same simple pattern on an icosahedron, this being the “platonic” solid with the largest number of faces. The choice of a pattern with regular hexagons

leads to the best approximation of circular figures. This tiling will always end up with $N_P = 12$ pentagons and with $N_H = 20 \cdot n$ hexagons, where $n = [i^2 + 3j^2 - 4]/8$, $i + j$ even, $2n$, i and j integers (Gerl and Korten , 2001). Some of the resulting configurations are shown in Figure 4.6.

Not all the possibilities are attractive for the AGATA array. The configuration which has small n values have very small radius and it is impossible to place any ancillary device inside. On the contrary, some of the configuration with larger n values have sufficient inner spaces, but it becomes impossible to group easily the detectors into triple or quadruple clusters.

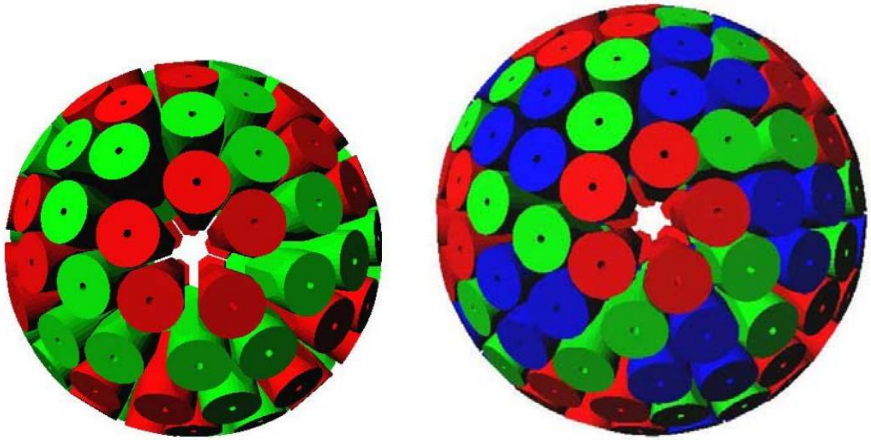


Figure 4.7 The most attractive configurations of the AGATA spectrometer. To cover the maximum effective solid angle around the target 120 or 180 detectors array was designed.

The configurations corresponding to $N_H = 120$ or $N_H = 180$ depicted in Figure 4.7 have been soon identified as the most attractive for AGATA. Their performance was evaluated and consistently compared (Farnea, 2004) by means of a simulation code based on the GEANT4 toolkit (Geant4 Collaboration, 2003), as reported for instance in Figure 4.8 and in Table 4.1. The A180 configuration corresponding to $N_H = 180$ has the best performance and was therefore chosen for the full AGATA array. As a matter of fact,

variants of the A120 configuration based on $N_H = 120$ could cover the same solid angle as the A180 configuration, but in the latter case the tracking algorithm performs better, leading to larger efficiency values. This can be explained by noting that the detectors of the A180 configuration are placed at a larger distance from the target and the direction of

Table 4.1 Some of the relevant geometrical characteristics of the configurations.

	A120	A120F	A120C4	A180
Number of crystals	120	120	120	180
Number of crystal shapes	2	6	2	3
Number of cluster types	2	2	1	1
Covered solid angle (%)	70.97	77.79	78	78.36
Volume of Germanium (cm^3)	43590	42225	43160	70243
Mass of Germanium (kg)	232	225	230	374
Initial mass of Germanium (kg)	289	289	289	434
Centre to Detector face distance (cm)	19.7	18	18.5	24.6

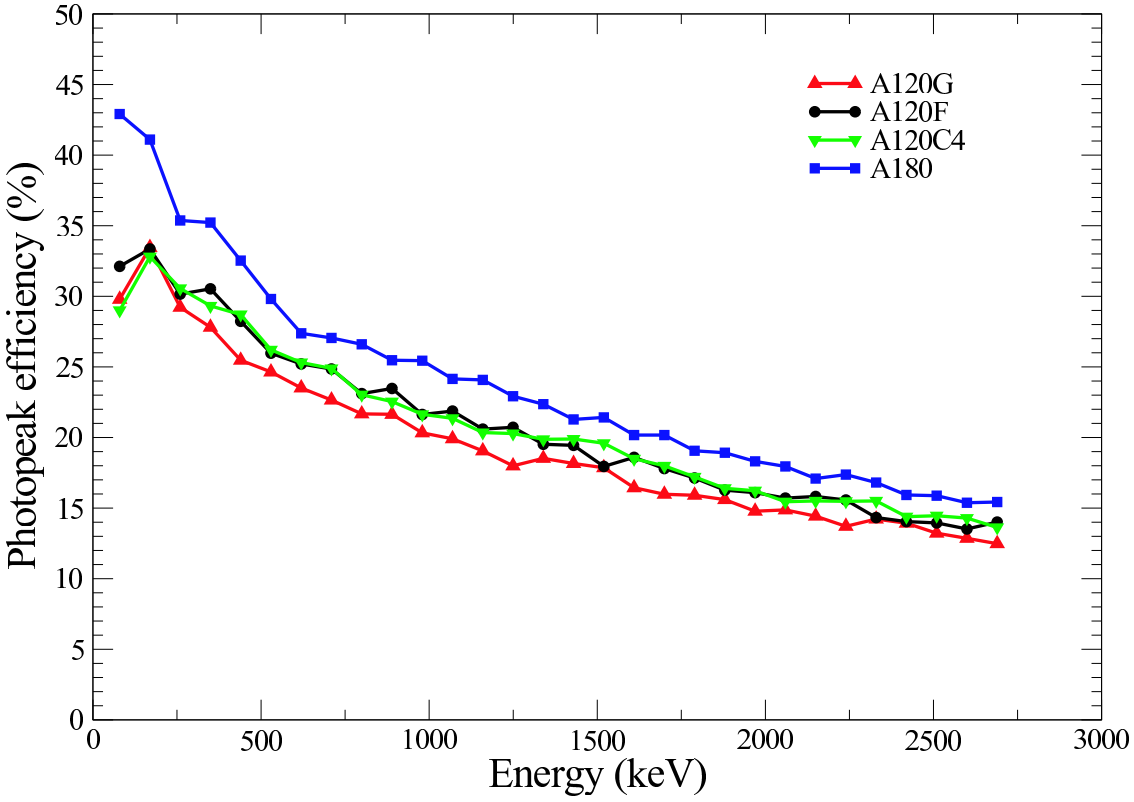


Figure 4.8 Calculated photopeak efficiency, in the case of a point source at rest in the geometrical center of the array, for the proposed configurations of AGATA (Farnea and Bazzacco, 2004; Farnea, 2004).

the photons is better defined, since the position resolution is assumed to be the same in both cases. A schematic drawing of the triple cluster composing the A180 configuration is shown in Figure 4.9 together with a photograph of the actual detector.

4.5 The AGATA Detector

As discussed in the previous Section 4.4 the AGATA array will be built out of irregular hexagonal prisms. The detectors are obtained by tapering a cylindrical crystal having 80 mm diameter and 90 mm length. Since the reliability and the stability of performance of the detectors was considered of paramount importance, it was decided to rely on the encapsulation technology (Eberth et al., 1996) developed within the framework of the EUROBALL collaboration. The individual crystals will be closed and hermetically sealed by electron welding into an aluminium can 0.5 mm thick. As mentioned previously, the AGATA detectors will be 36-fold segmented in order to exploit the pulse shape analysis techniques. The details of the segmentation scheme were optimized through extensive electric field calculations. Being the detectors hexagonal prisms, a 6 sectors x 6 slices



Figure 4.9 The simulation (left) and real (right) AGATA triple cluster.

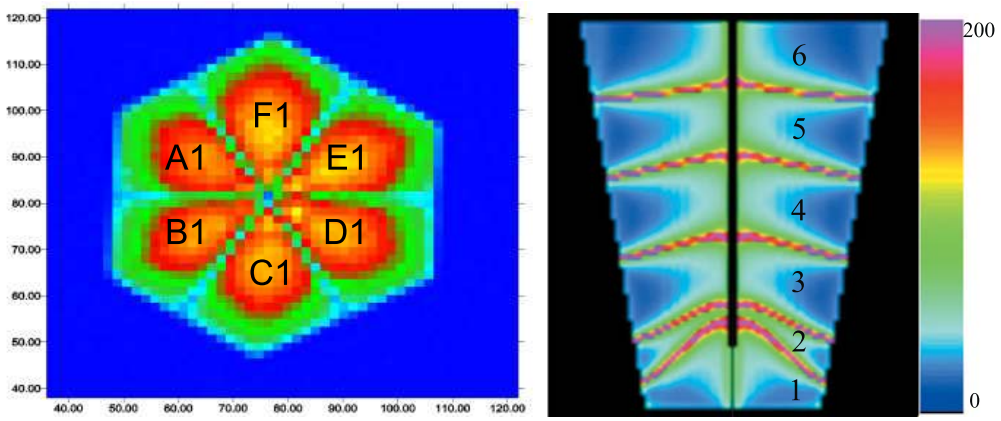


Figure 4.10 Simulation of the effective segmentation of the AGATA detector with color scale. The colour scale represents in arbitrary units the position sensitivity of the AGATA prototype crystal (Görgen, 2003). The effective volume of the segments in the front part of the crystal is much larger than the value deduced from the segmentation scheme because of the distortion of the electric field. At variance with the names reported in the figure the order of the sectors of the actual detector is clock wise when looking to front hexagonal face of the crystal.

scheme results naturally, where sectors are labelled from “A” to “F” and slices from “1” to “6”. The outer segmentation for the slices is not regularly spaced in the attempt to balance the effective volumes of the segments. As a matter of fact, the distortion of the electric field in the front part of the detector, shown in Figure 4.10, makes the effective volume of the segments different than the geometrical volume.

Since the exact details of the AGATA detectors have been decided quite in a late stage of the project, some prototype detectors of a roughly similar shape were bought from Canberra France in order to check the quality of such complex objects and to gain experience in handling them. Hence, the first three prototypes (S001, S002 and S003) have a regular hexaconical shape. A picture of the prototype S001 AGATA detector used in the present work is shown in Figure 4.11 together with the resolution values for all of its segments. Figure 4.12 shows instead a schematic layout of the test cryostat.

As discussed previously, the detectors of AGATA will be grouped into triple clusters in a common cryostat. Each cryostat will contain also the preamplifiers for 111 channels (36 segments + core for each crystal). A picture of the prototype cryostat, built by the company CTT, is shown in Figure 4.9. With its 111 high resolution channels ($\sim$3 times more than GASP, $\sim$50% of the whole EUROBALL) this cryostat is an extremely complex object and its performance and reliability are critical for the success of the project. Its

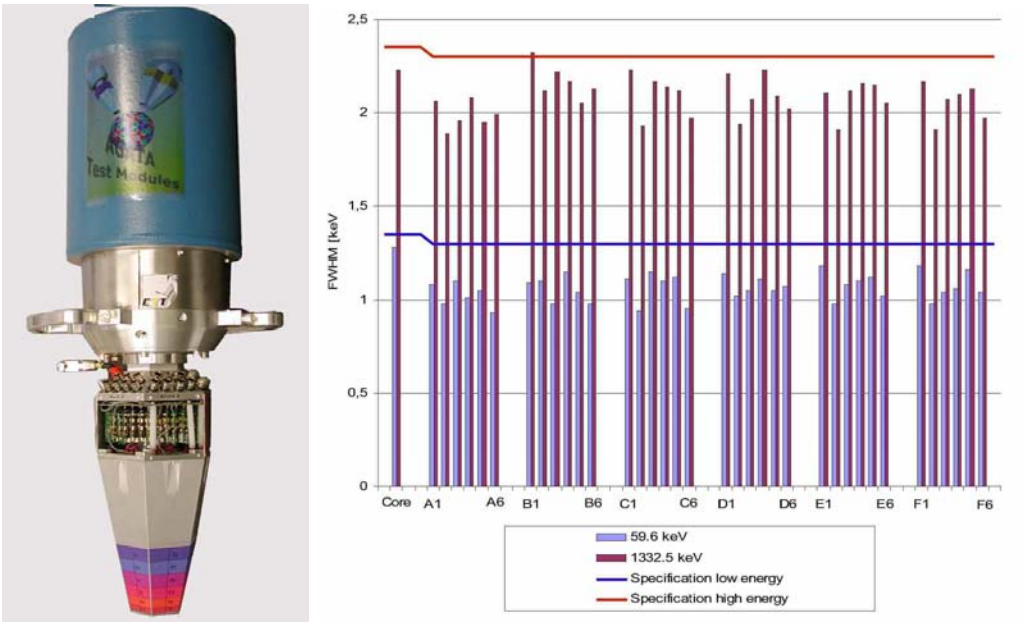


Figure 4.11 Photo of the prototype S001 AGATA detector and resolution values of its 37 channels for 60 and 1332 keV photons.

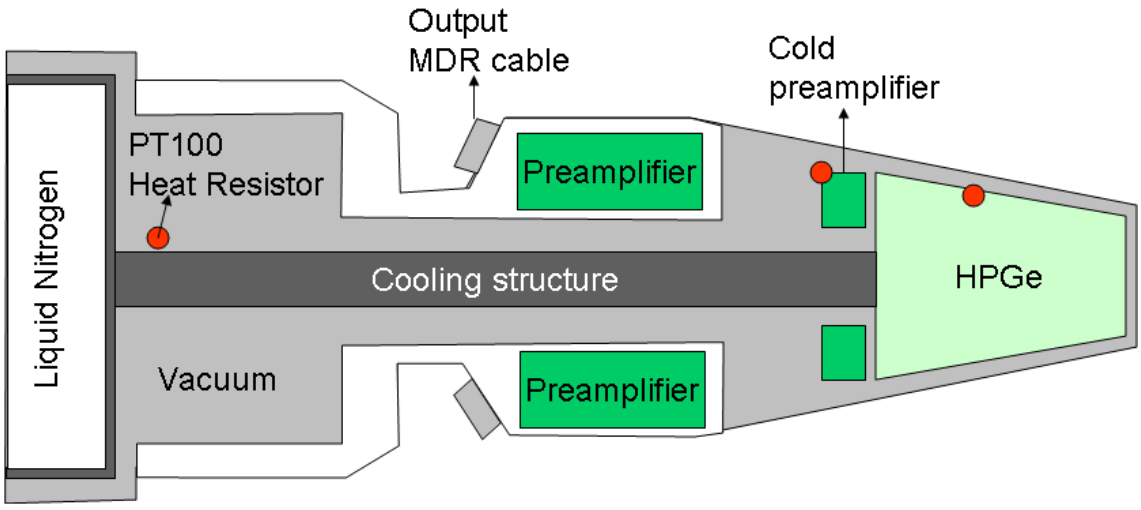


Figure 4.12 Sketch of the AGATA test cryostat.

development has been carried out in close collaboration between the manufacturer and the AGATA-detector working group.

4.6 Preamplifiers

The AGATA preamplifiers have been developed in collaboration by INFN (Istituto Nazionale di Fisica Nucleare) Milano, GANIL (Grand Accelerateur National Ions Lourds) and IKP Cologne. They will have a critical role to achieve a good system performance and to preserve pulse-shape integrity. (Pullia et al., 2006). Special care has been taken in keeping a sufficiently large bandwidth, so that the information on the position of the interaction, which is contained in the early part of the signal, is not lost.

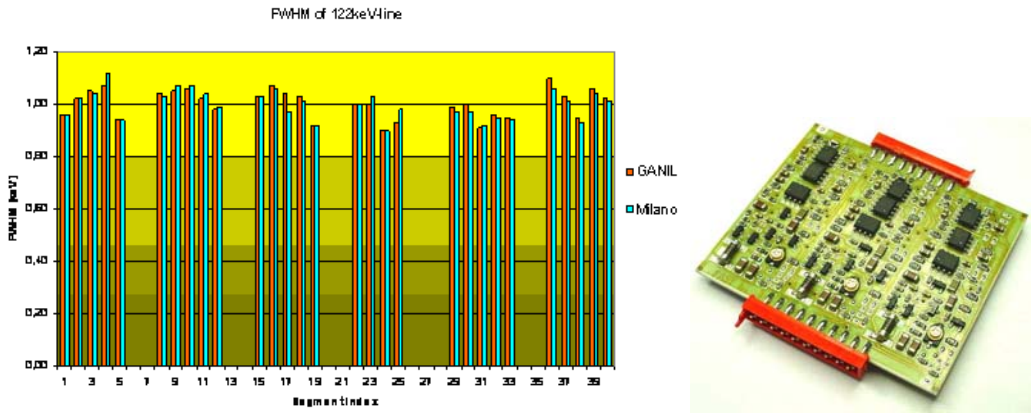


Figure 4.13 Noise measurement of the “GANIL” preamplifiers (left) and ”Milan” preamplifiers (right), (Zocca, 2008).

Following the experience of previous HPGe detectors the most important requirements for the preamplifier can be summarized as follows (Zocca, 2008):

- Low noise, in order to ensure good-quality spectra.
- Low power consumption, in order to have high number of Field Effect Transistors (FETs) cooled in the same cryostat.
- Wide bandwidth: preamplifier response to a fast input pulse must have a fast rise time to preserve the shape of the transition edges of the slower signals released by the Ge detectors, which is needed to apply the pulse shape analysis algorithms.
- Large dynamic range (from a few keV up to 10-20 MeV), in order to detect the radiation emitted by nuclei under very extreme conditions.

- Short fall time ($\sim 50\mu s$ for the segment and $\sim 30\mu s$ for the core), in order to reduce event-to-event pileup. This is necessary in the case of high events rates (up to 50 kHz)

Two kind of preamplifiers have been produced by the AGATA collaboration and a comparison of the energy resolution is shown in Figure 4.13. Their performance is quite similar and indeed the detectors are equipped with preamplifiers of both type.

4.7 The AGATA Electronics

As discussed earlier, the information on the position and energy of the individual interactions will be extracted by applying pulse shape analysis (PSA) algorithms to the digitized signals. In order to keep the relevant information, a sampling frequency of at least 100 MHz with 14 bits ADCs is needed. Assuming a singles rate of 50 kHz per crystal, as specified in the design goals for AGATA, the expected flux of data is too high to be stored and handled, (6660 segments x 200 MB/s) and therefore methods to extract the relevant information in real time, thus reducing the data flow to acceptable values, have to be applied. The scheme of the AGATA Data Acquisition System (DAQ) is outlined in Figure 4.14.

A time stamp from a central clock generator (Global Trigger and Synchronization, GTS) (Bellato, 2007) is distributed to all of the digitizers, as well as the same 100 MHz clock to ensure synchronization. The digitized signals are sent over optical fibres to the pre-processing electronics which analyzes each crystal independently through algorithms implemented into powerful highly-parallel FPGAs (Field Programmable Gate Arrays). This includes a digital trigger applied to the anode (core) signal and energy calculation through the so-called Moving Window Deconvolution (Georgiev and Gast, 1993; Gast et al., 2001). At this stage, up to 160 samples (1.6 μs) of the rise time of the pulse are kept, discarding the rest. This process reduces the data flux to approximately 95% of the original values, but in some cases a further reduction is needed and a second level trigger, which might include highly selective conditions from ancillary devices, should be applied.

The validated pre-processed events are passed to the PSA computing farm, where the

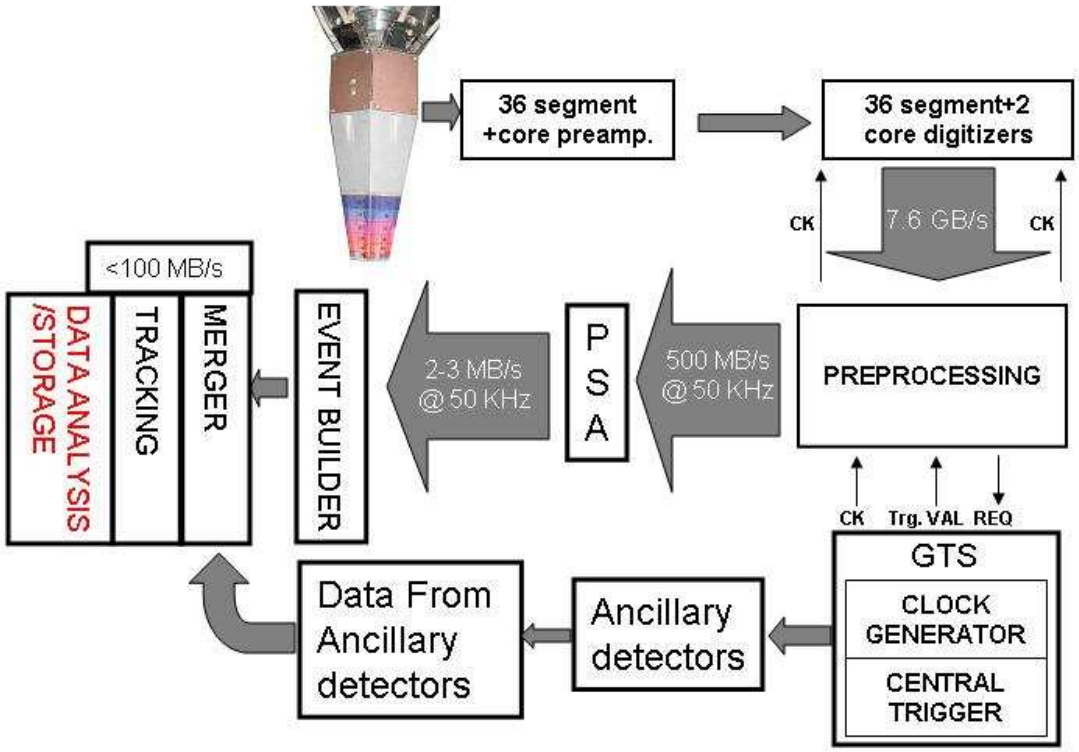


Figure 4.14 Dataflow description and DAQ steps for AGATA.

coordinates of the interaction points are extracted from the pulse rise-time samples. Following this process, the data throughput can be further reduced by discarding the original traces. The fastest PSA algorithms developed so far need a few milliseconds to process an event, this being the bottleneck of the whole data processing sequence.

Following PSA, which is still performed at detector level, the global event is built by collecting together the information from all firing detectors. Event fragments are recognized on the basis of the event number and/or of the time stamps. The tracking algorithm can process the global event to extract the full information (number, energy, first and second interaction points) on the detected photons. This information can be saved to permanent storage for the final off-line data analysis.

4.8 The AGATA Demonstrator

Since the design assumptions used to develop the AGATA array were quite challenging, it was considered mandatory, while defining the project, to provide a “proof of prin-

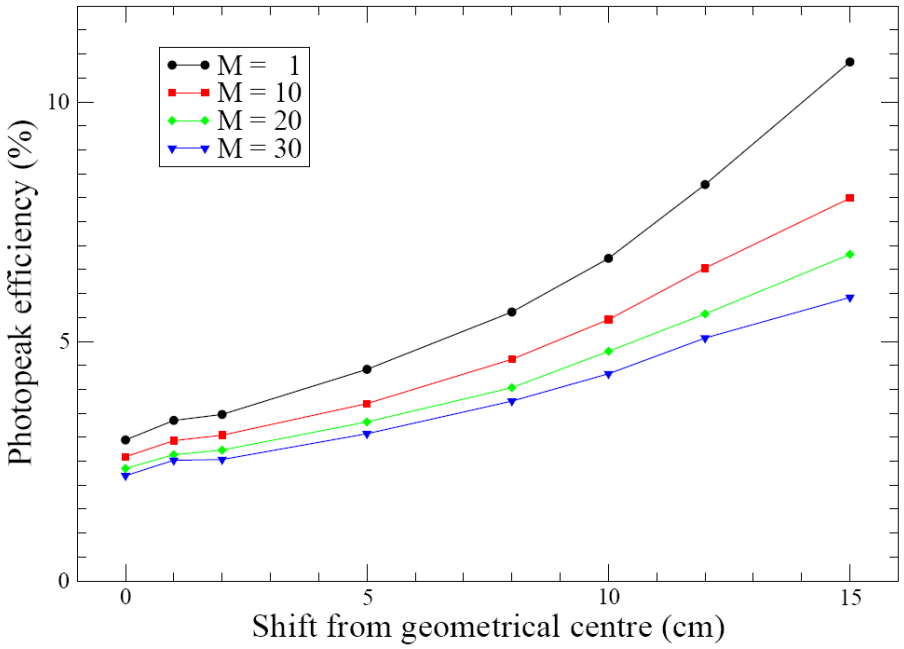


Figure 4.15 Absolute photopeak efficiency of the AGATA Demonstrator Array for 1 MeV photons emitted from a point source at rest. It is assumed that the whole array can be moved rigidly towards the source position

ciple" that it is indeed possible to operate in real time an array of germanium detectors based on the pulse shape analysis and γ-ray tracking techniques. Therefore, it was decided to build, in the initial phase of the project, a subset of the whole array, known as the AGATA Demonstrator Array, which will provide such a proof of principle.

The AGATA Demonstrator Array is an arrangement of five triple clusters of the same kind of the 60 modules which will be used to form the final AGATA array. The performance of such an object will depend in a critical way on its placement relative to the target position. In particular, given the lack of a spherical symmetry, it is reasonable to place the detectors closer to the target position compared to the "reference" distance of the full array, which is 23.5 cm (Farnea, 2005). The photopeak efficiency and the P/T ratio as a function of the shift from the geometrical centre are shown in plots of Figure 4.15 and Figure 4.16, where it is assumed that 1 MeV photons are emitted from a point source at rest in the Laboratory reference frame. The shift from the geometrical centre is calculated assuming to move the Demonstrator as a whole towards the source position.

It is important to observe that the quality of the spectra is not lost even if quite high source velocities are assumed, as shown by the calculated peak FWHM values presented

in Figure 4.17. Actually, the photopeak efficiency of the Demonstrator Array placed at forward angles increases with the average recoil velocity, reflecting the increased solid angle coverage produced by the Lorentz effect, as shown in Figure 4.18.

The first installation site of the AGATA Demonstrator array will be the Laboratori Nazionali di Legnaro, where it has replaced the CLARA (Gadea et al., 2003) array in coupled operation with the PRISMA spectrometer.

4.9 The AGATA Collaboration

The AGATA Collaboration consists of 12 countries: Bulgaria, Denmark, Finland, France, Germany, Hungary, Italy, Poland, Romania, Sweden, Turkey, UK. The first Memorandum of Understanding of the collaboration covered the period up to the end of 2008 and new agreement is presently under discussion. It is foreseen that several campaigns will be run with partial subsets of the array as shown in Figure 4.19, up to its final completion which could happen around 2018.

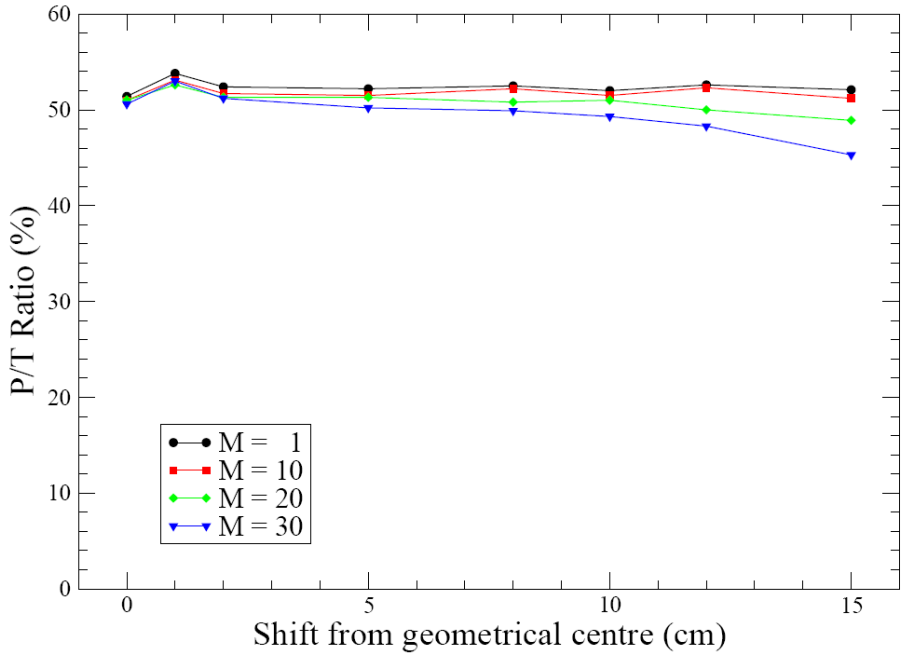


Figure 4.16 Peak-to-total ratio of the AGATA Demonstrator Array for 1 MeV photons emitted from a point source at rest. It is assumed that the whole array can be moved rigidly towards the source position.

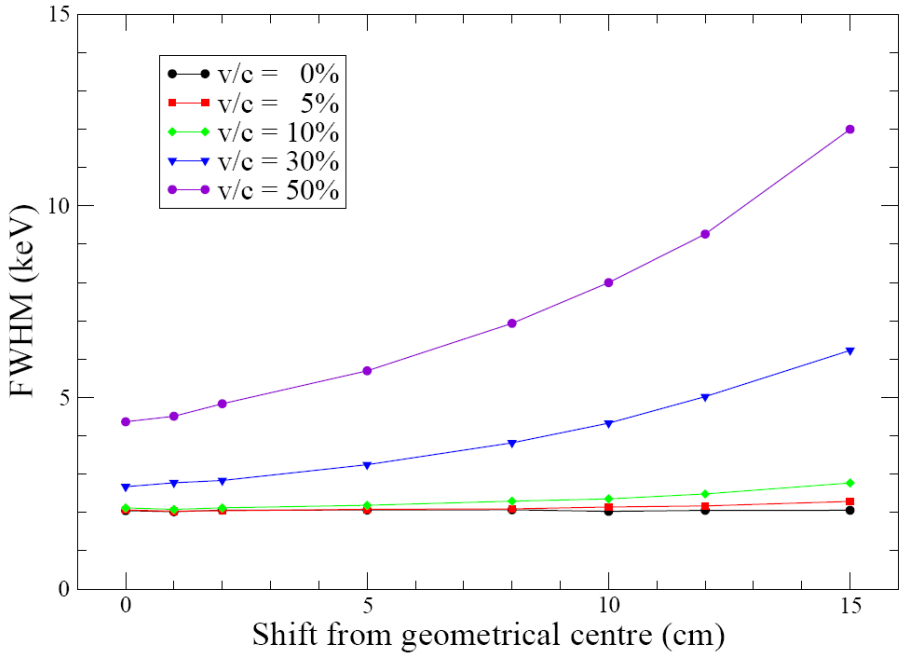


Figure 4.17 Calculated peak FWHM for 1 MeV photons emitted by a point source recoiling along the z axis and detected with the AGATA Demonstrator Array placed at forward angles.

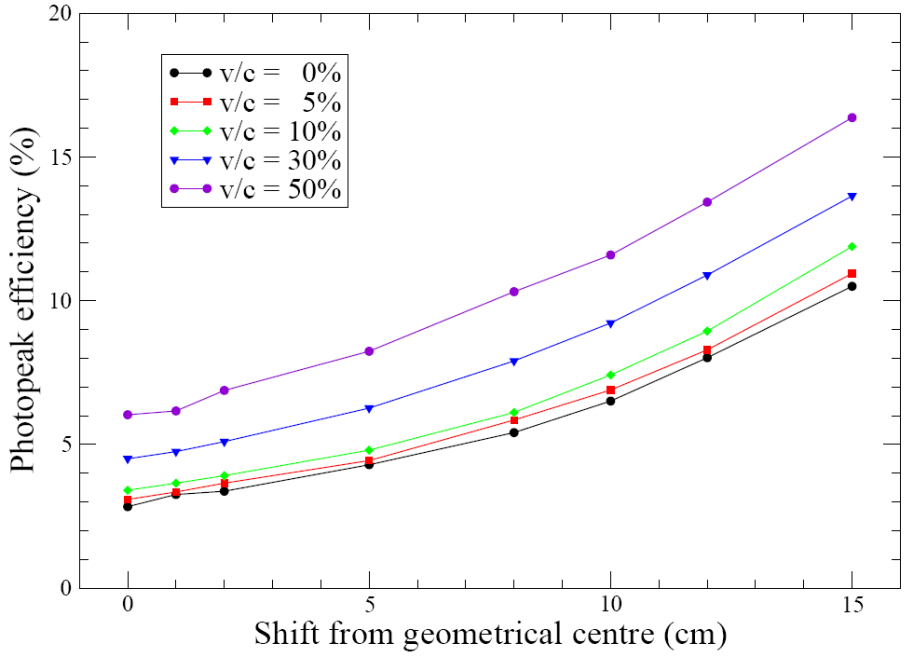


Figure 4.18 Absolute photopeak efficiency of the AGATA Demonstrator Array placed at forward angles for 1 MeV photons emitted by a point source recoiling along the z axis.

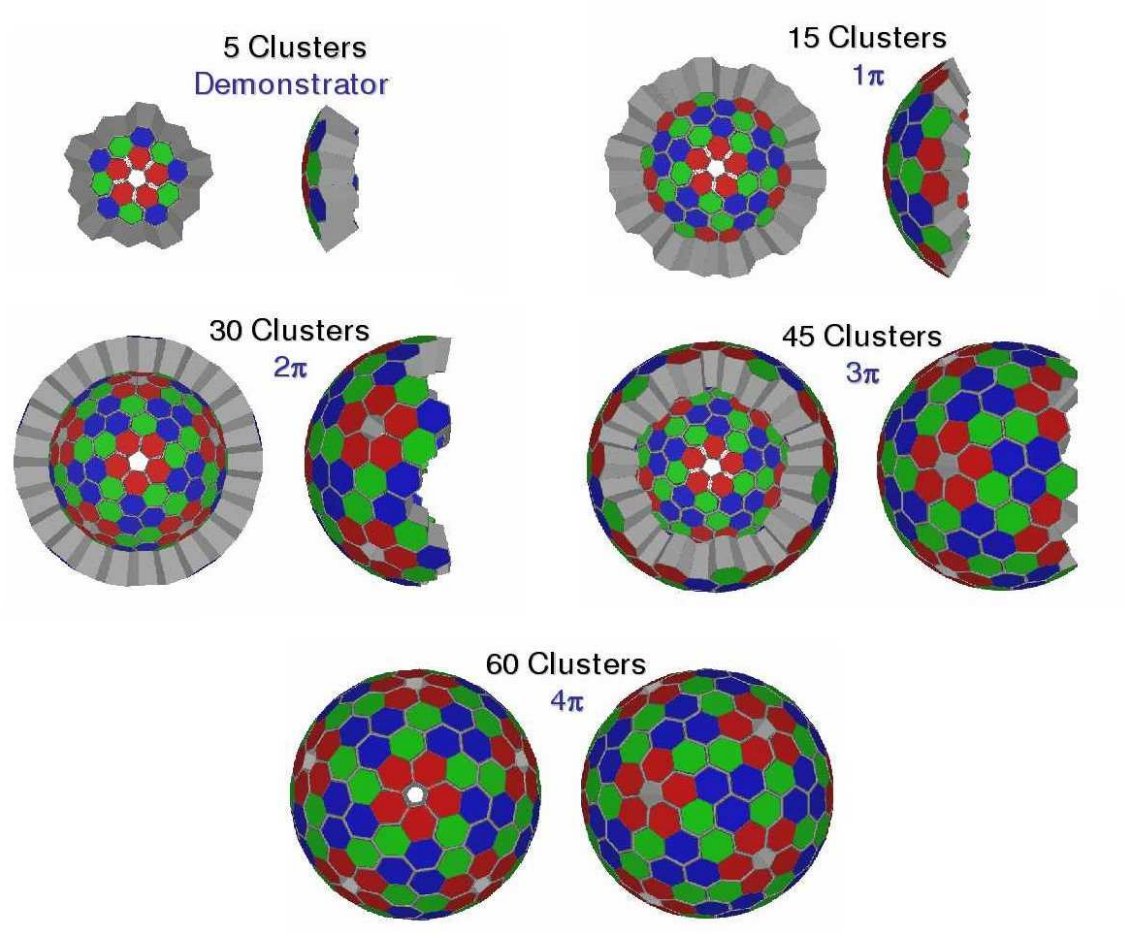


Figure 4.19 Evolution of the AGATA project from the demonstrator to the full 4π array.

5. EXPERIMENTAL WORK and RESULTS

Experimental nuclear physics is facing the new challenges posed by the use of radioactive nuclear beams. As stated in previous chapters, the achievement of the performance required to detect the gamma radiation in such environments is critical, with particular reference to efficiency and effective energy resolution. Germanium detectors technology is a forced choice for such detection systems because, in the 100 keV to 10 MeV energy range it provides the highest energy resolution together with a short radiation length.

A revolution is occurring in these years to the detection systems used for in-beam γ-ray spectroscopy: putting together the state-of-the-art technology of digital processing and germanium detector segmentation we are constructing the first array composed of germanium detectors with position sensitiveness. While the foreseen performance of the new generation devices will allow an improvement of many orders of magnitude in experimental sensitivity, their development is posing qualitatively new problems.

The number of high resolution electronics channels that have to be acquired and analyzed in these new detectors is two orders of magnitude higher with respect to the previous generation arrays. In fact, just one of the AGATA detector will have approximately the same number of channels of CLARA (Gadea, 2005) or GAMMASPHERE (Lee, 1990). As it will be discussed in this chapter, such a "high-density" poses new problems of couplings and correlations between channels, which, if not properly dealt, will result in a poor energy resolution. This thesis was devoted to study and solve some of such problems.

5.1 The Test System

As explained in the previous chapter, the final shape of the germanium crystals used in AGATA will be that of an irregular hexa–cone with an average tilting of the flat side surfaces of about 8 degrees. In view of the long time needed to optimize such a complicated shape, the community started working on the signal and electronics aspects of the γ-ray tracking concept, with a simpler prototype detector. This is a single crystal detector with a regular hexa-conical shape and with a larger tilting angle of 10 degrees. Apart from the geometrical details, this crystal has the same length and radius and, most important the same number of segments as the final AGATA detectors. An AGATA "symmetric triple

cluster" composed of 3 of symmetrical crystals has been assembled in 2005 and used for an in-beam test at the Institute of Nuclear Physics of the Cologne University to measure the position resolution and compare the performance of the present pulse shape analysis algorithms (Recchia, 2008).

After this experiment, the triple cluster was disassembled and its 3 crystals were mounted in single cryostats. Since then, the three crystals have been used in various laboratories to better understand the effects of segmentation and to pursue the development of electronics, signal shape analysis (for example 3D scanning) and data analysis methods. One such single cryostat, named "S001", is in the Legnaro National Laboratories since the end of 2006 and has been used for most of the developments reported in this thesis.

It should be clear that using such a complicated object is a big challenge in terms of needed equipment because of the many electronics channels that must be managed. In particular, the fact that the final AGATA electronics is not yet available implies the need of setting up a replacement that can manage 37 high-resolution channels in a fully digital way. The studies reported here, such a system has been built out of ten 4-channels NIM digitizer boards with real time digital data analysis capabilities developed at IReS Strasbourg under the name of TNT2 (Arnold et al., 2005) and commercially available as N1728A by CAEN (CAEN, 2007).

The most important features of these cards will be introduced in following section.

5.1.1 The TNT2 Digitizers

The aim of TNT2 boards is to digitize up to 4 input signals at sampling frequency of 100 MHz with 14 bits per sampled points and to achieve real-time processing of the sampled data, becoming an effective replacement of a standard spectroscopy amplifier plus peak-sensing ADC data acquisition system. Similar or even better performance than the classical analogue systems has been achieved by using up-to-date digital signal processing methods (i.e. trapezoidal shaping with baseline restoration and digital fast trigger) implemented in real time in FPGA (Field Programmable Gate Array) modules. Event readout is performed through a fast universal serial bus (USB2) and the data can be acquired by the use of a standard PC. The throughput of the system can go up to 100 k events per

second per channel. If only the energy seen by each channel is readout.

An important feature of these modules for the work reported here is the possibility to readout long traces of sampled data (up to 1 M samples, corresponding to 10 ms) which allow for a detailed off-line analysis of specific signal features. In this operation mode, the data acquisition speed is limited by the bandwidth of the USB2 bus to about 30MB/s/module but most of the time the real limit is in the speed and amount of available hard-disk storage.

Also important is the possibility to work in the so-called mixed mode where both the energy built in real-time in the FPGA and a short piece of sampled traces in correspondence with the charge collection are readout. This gives the possibility to perform off line the pulse shape analysis for example to study the position sensitivity of the detector.

The TNT2 board is operated by a slow-control and data acquisition software called TUC which has been developed by the Strasbourg group in the Java programming environment so as to be able to run it both with Linux and Windows PC's. The TUC system allows to change and monitor the setup parameters of multiple TNT2 cards, can display the sampled signals (like a digital oscilloscope) and the energy spectra built from the data readout flow and, finally, it is in charge of the storage of the data.

A screen shot of the graphical interface of the TUC program is presented in Figure 5.1. As shown in the upper part of the figure, this window is used to select the input channels, the data acquisition mode and the trigger type and parameters. A second window, which can be partly seen in the lower part of the figure, is used to define the parameters of the real-time energy calculation algorithm.

It is known (Knoll, 2000) that the best energy resolution can be achieved by the so-called cusp shaping. Such shaping, however, does not find practical application as a consequence of the finite collection time (causing ballistic deficit) and infinite duration. A triangular shaping was proposed by Gatti (Gatti et al., 1982). Such solution has the advantage of being implementable in FPGA but again presents the ballistic deficit problem. The optimal choice is the trapezoidal shaping, which has the good characteristics of the triangular one but contains a flat top that compensates for the finite rise time of the signals (Stein et al., 1996; Smith, 1999). This shaping is very difficult to achieve with analogue electronics and indeed the spectroscopy amplifiers for high resolution gamma-ray spec-

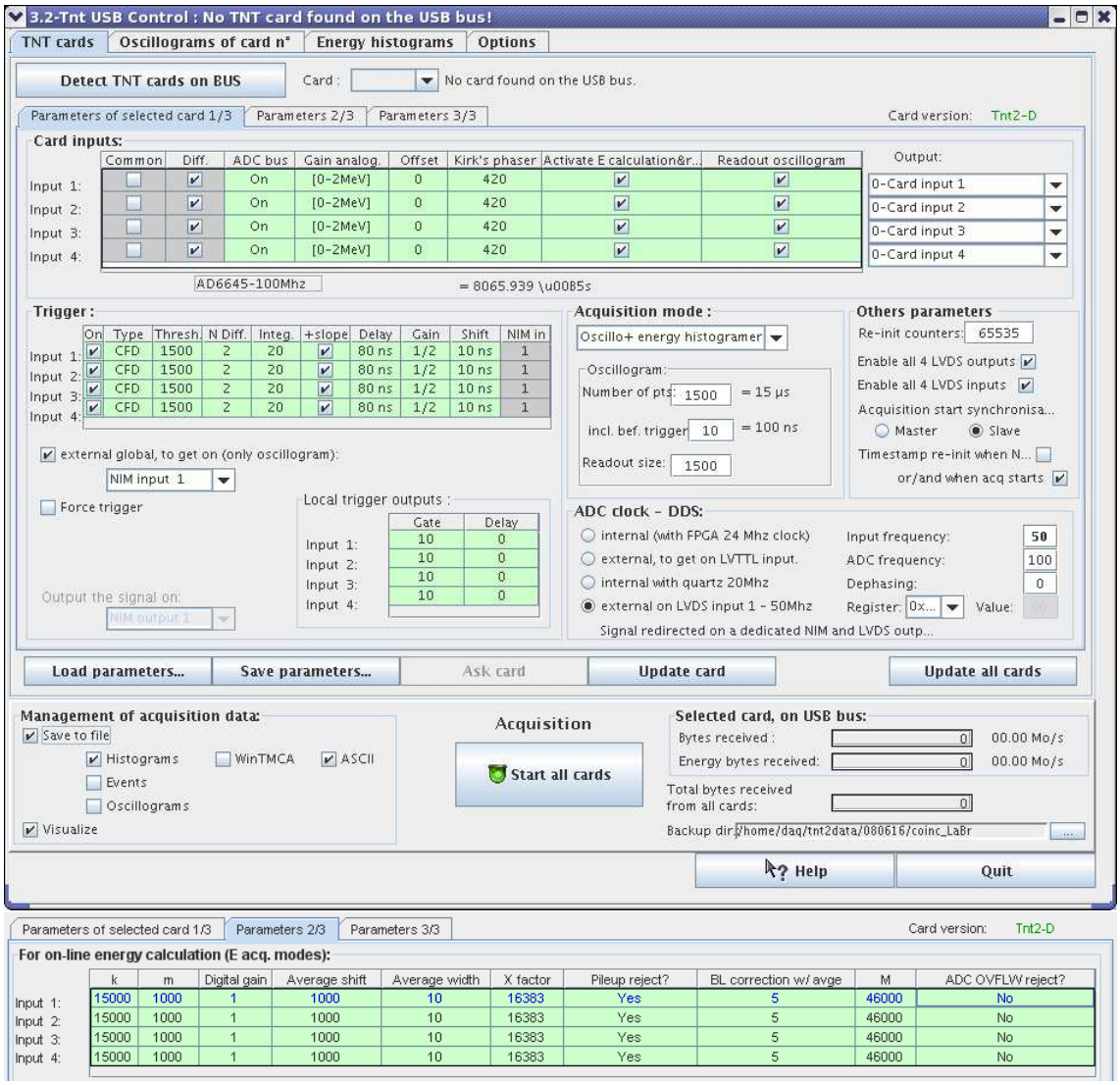


Figure 5.1 A screen shot of the TUC program interface

troscopy use a pseudo-Gaussian shape with pole-zero compensation. On the other side, with digital electronics the trapezoidal shaper is easily implemented and its superior filtering with respect to what is used in analogue electronics is a reason to expect that the new detector systems will have an improved energy resolution.

The actual version of the trapezoidal algorithm implemented in the TNT2 follows the Jordanov (Jordanov and Knoll, 1994) formulation, even if in the AGATA community this data treatment is known in the equivalent formulation of Gast (Georgiev and Gast, 1993) as Moving Window Deconvolution (MWD). This name points out that, in order to achieve the trapezoidal shape, the exponential-decay of the charge-sensitive preamplifiers signals has to be removed (deconvolved).

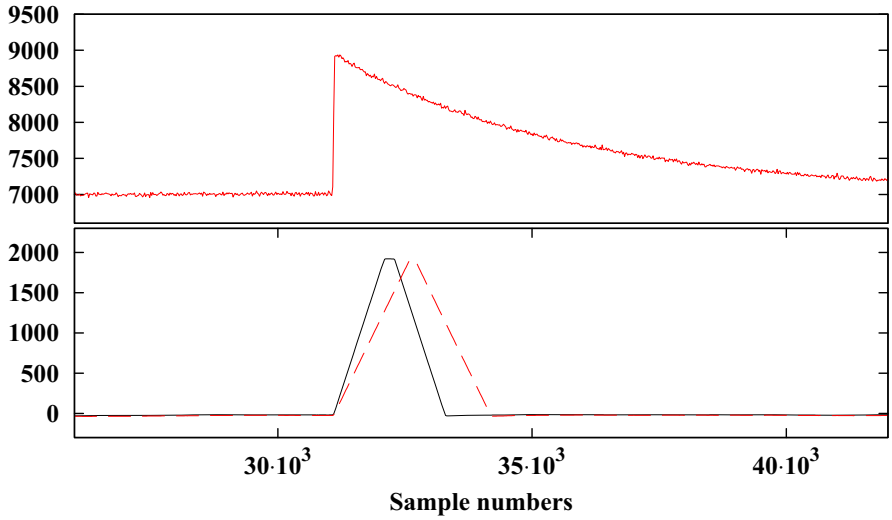


Figure 5.2 The Exponential signal of the preamplifier converted to a trapezoidal shape by the MWD algorithm. The amplitude of the signal is taken from the flat top of the trapezoid. For the two trapezoids it was used 10 μs rise time and 2 μs flat top (black) and 15 μs rise time and 1 μs flat top (dashed red).

The relation of the trapezoid to the signal from the preamplifier is presented in Figure 5.2 which shows the effect of the two important parameters, rise time and flat top, that must be optimized to obtain the best energy resolution. In many cases our energy spectra have been obtained by using 15 μs (1500 samples) raise time and 1 μs (100 samples) flat top of the trapezoid.

Another crucial parameter is the decay time of the preamplifier used for the deconvolution of the original exponential. This parameter, if not perfectly matched, can produce a non-flat top of the trapezoid and long undershoots or overshoots on the shaped signals. These last are particularly dangerous for the energy resolution because they falsify the amplitude of the next signals arriving before the base line has returned to zero.

Finally, the other important signal treatment for achieving the best possible energy resolution is the removal of low frequency fluctuations in the baseline of the shaped trapezoidal, which are due to always-present low-frequency noise. In the graphical controls of TUC the names of the various parameters are k (rise time of the trapezoid), m (duration of flat top), M (fall time of the exponentials) and BL (base line restorer calculation window).

5.1.2 ENOB and SNR Measurement

Of the large amount of work done to qualify the TNT2 modules, the part related to the characterization of their effective number of bits (ENOB)[1] and the related signal-to-noise ratio (SNR)[2] is reported in the following. This characterization is important because it defines the dynamic range of signals that can be properly digitized without loss of information. In fact, if the maximum accepted amplitude is defined by the manufacturer, the minimum amplitude signal is the one that stands out of the noise.

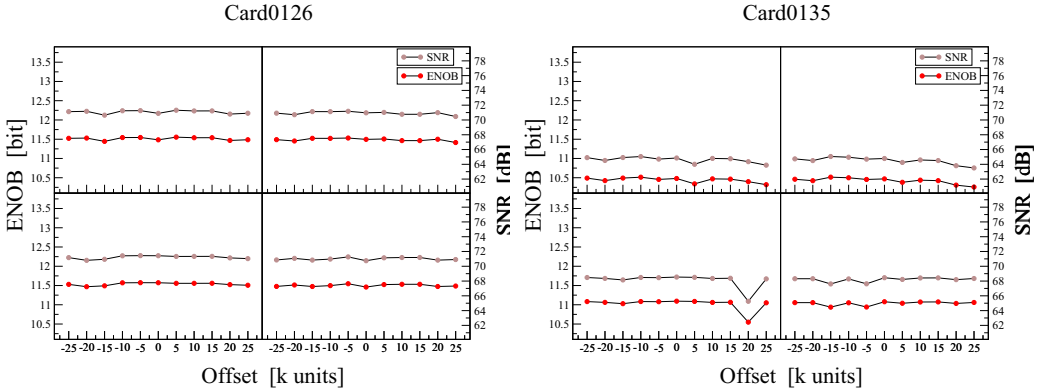


Figure 5.3 ENOB and SNR of two TNT2 modules. Card0135 has worse ENOB and SNR, probably due to problems of some internal components.

These checks have been done by recording long traces from all channels of the modules without any input signals and by moving the internal offset-controls so as to span the whole range of accepted amplitudes. In absence of noise, the expected output from the

[1] ENOB is explained as the quality of an analog-to-digital converter and it is given by (Gielen, 2006);

$$ENOB = \frac{SNR - 1.76}{6.02} \tag{5.1}$$

which is related to the SNR value.

[2] SNR is explained as the ratio of a signal power to the noise power corrupting the signal in units of dB. The expression of the SNR (Gaddy and Kawai, 2000) is;

$$SNR = 20 \cdot Log_{10}\left(\frac{V_{rms}}{\sqrt{\sigma_{rms}^2 + \frac{(\Delta)^2}{12}}}\right) \tag{5.2}$$

where Δ is least significant bit,

$$\sigma_{rms} = \frac{FWHM\ of\ the\ noise}{2.355} \tag{5.3}$$

and

$$V_{rms} = \frac{Full\ scale\ of\ the\ card}{2\sqrt{2}} \tag{5.4}$$

digitizer is a unique value for each of the selected offsets. Of course this is not what happens in practice, because one gets a Gaussian distribution of amplitudes with a FWHM that, once inserted in the proper formulas (5.1 and 5.2), translates into the SNR and ENOB figures. These results are presented for two digitizers in Figure 5.3. As it can be seen, there are differences in the modules and in their channels and, occasionally, there is some dependence on the amplitude of the signal. However, all measured values are consistent with the specifications of the manufacturer and good enough for the work done in this thesis where the dynamic range of the signals is rather small due to the use of low energy radioactive sources.

5.1.3 Synchronization and Local Trigger

A segmented germanium detector is equivalent to a multi-detector system and it is clear that its data must be properly synchronized. This has to be done even if one is interested only in single energy spectra because in order to account for the crosstalk between the electronics channels (segment-segment and core-segment) which can degrade significantly the energy resolution if not properly managed.

In a sampling electronics system like the one used here, the main correlation among the channels is provided by distributing a common clock and trigger to the various digitizer channels and by marking each recorded item of information with an absolute time reference (usually called “time stamp”) which is obtained by the system counting the number of clock pulses received by the common source.

In a common-clock time-stamped sampling system the various channels can be recorded independently, even in different acquisition systems, because in the analysis phase the data can be correlated by looking to this label.

For the TNT2 digitizers, the synchronization of the 4 channels of each board is trivial (they are operated and controlled by the same hardware) but the management of different boards is a problem because there is no system bus and the USB2 readout is not synchronous over different ports. The developer of the TNT2 board provided the possibility of distributing a common clock (via a flat cable in the back of the modules) but each module has its own internal counter for the time-stamp and one must be sure that all of them stay in phase for the whole data acquisition period. Fortunately the practice shows that

losses of synchronization due to the time-stamping system are rather rare.

Even if the synchronization of the various electronics channels is guaranteed, one has to consider the consequences of the limited amount of data that the acquisition system can read out. It is clear that this is a general problem for all present (and near future) data acquisition systems because at a sampling frequency of 100 MHz, each digitizer channel produces a dataflow of 200 MB/s which sums up to the huge value of 7.4 GB per second for a segmented AGATA detector.

Considering that the typical recording speed of a normal PC is of the order of 10-50 MB/s it is clear that the storage of the whole data flux can be done only for a very limited period of time determined by the amount of high speed memory of the digitizer modules. The TNT2 boards can store 1 M samples for each of the four channels (corresponding to 10 ms), giving a total amount of 74 MB of data for 37 channels. This takes at least one second to be readout and stored, giving an overall efficiency of 1% or a system dead time of 99%.

It is clear that, in order to increase the efficiency to a reasonable level, the system must have a trigger that allows to select the events of interest, ignoring the (long) time intervals when nothing relevant happens in the detector.

For the AGATA detectors, which have a segmented electrode (the outer cathode) and a common anode (the inner core) such trigger is naturally derived from the anode because this always sees a signal for interactions happening anywhere in the germanium crystal.

In the TNT2 based system used here, this trigger is generated by an external analogue electronics (but could also be done digitally in one of the boards) and fires only when a signal of sufficient amplitude is detected. The trigger signal is distributed via a front panel daisy-chain to the 10 boards which are forced to process the data even if the served channel has not been interested by that particular event. Each processing channel contains also a register, called “event number” that counts the triggers and can be used as an extra check to validate the consistency of the events.

Finally, to guarantee that all channels are again ready to process the next trigger, a busy signal is generated by each TNT2 card to inhibits the core from generating new triggers during the time needed to process and readout the previous one. This part of the system is rather complicated and not 100% reliable due to some inconsistency in the busy

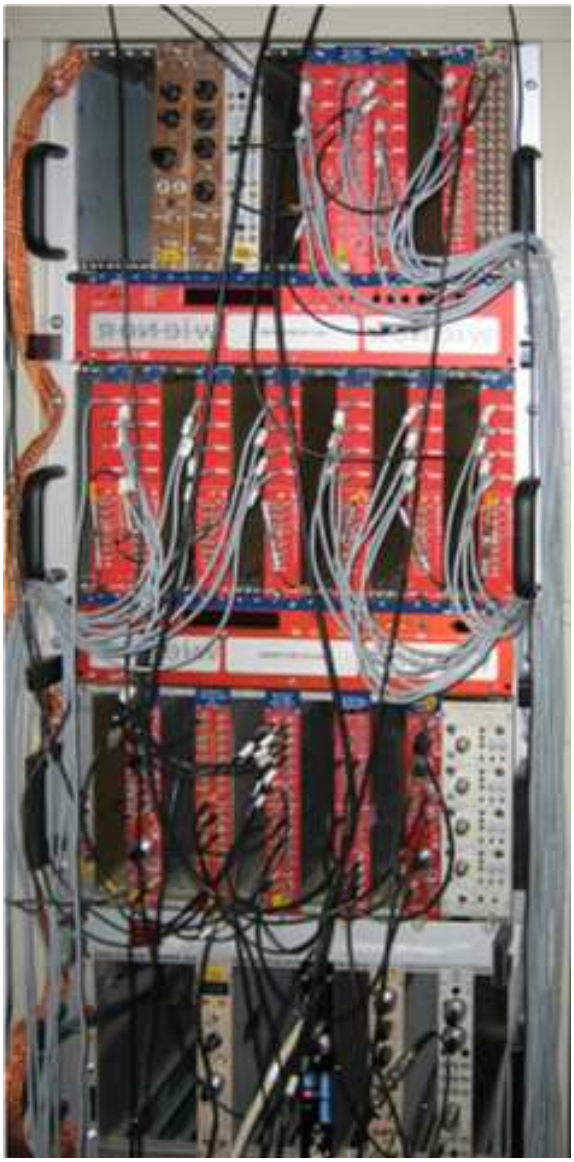


Figure 5.4 The TNT2 based data acquisition system used in this thesis.

signals provided by the TNT2 modules during the data readout phase. The consequence is that about 10% of the recorded events are incomplete and have to be discarded during the off-line analysis phase.

The final validation of the events during the off-line analysis is always done by comparing their time stamp and by requiring that all 36 segments and the core are present. Figure 5.4 shows a picture of the TNT2 based digitizer and data acquisition system.

5.2 Characterization of Detector Noise and Disturbances

Provided that the front-end electronics is adequate, the performance of a detector is limited by the fundamental noises (e.g. charge collection statistics and thermal noise) and by various disturbances picked up from the operation environment.

Over the years, the fundamental noise has been studied theoretically and the signal processing has been optimized to take into account. On the other hand, all other sources of perturbation damaging the measured signals have to be studied empirically on the actual detectors and have to be minimized in order to reach a performance as close as possible to the best possible one.

Consequently, quite a lot of effort has been invested in the characterization of the detector noise by studying its frequency spectrum. By using the TNT2 boards which have

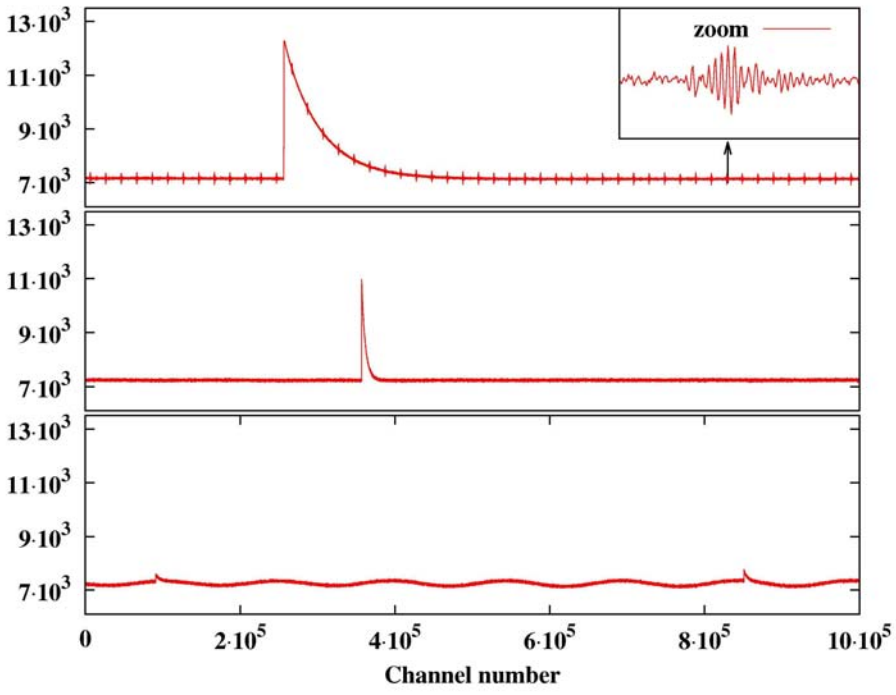


Figure 5.5 A comparison between a clean signal (middle panel), a noisy signal dominated by high frequency disturbances (higher panel) and a low frequency microphony (lower panel).

the capability to record long sequences of digitized data, this characterization comes as a natural extension of the traditional tools consisting essentially of observing the detector signals with an oscilloscope and determining the energy resolution using known radioactive sources.

The noise of the system can be schematically divided into two parts: a low-medium frequency range (10–100 kHz, see the lower panel of Figure 5.5) which has an impact on the energy resolution and a high frequency region ($>$ 100 kHz as exemplified in the upper panel of Figure 5.5) which affects the performance of the pulse shape analysis (PSA) and reduces the achievable position resolution.

Effect on the Energy Resolution: As mentioned in a previous section, the energy of the incident gamma is given by the amplitude of the trapezoid produced by the shaping algorithm running in the FPGA of the TNT2 modules, subtracted by the baseline calculated on the signal-free region preceding the pulse. High frequency noise is smoothed out by the filter but any disturbance with a frequency corresponding to the rise time of the trapezoid ($\sim$ 50 kHz for a shaping time of $\sim 10\mu s$) will pass through unfiltered and will overlap in a random way with the amplitude of the actual signal, resulting in a worse energy resolution. Very low frequencies will also cause fluctuations of the baseline but, as their amplitude does not vary significantly during the shaping time, they will be effectively suppressed by subtracting the baseline calculated before the arrival of the signal.

Effect on the PSA: Although the high frequency disturbances are not affecting the energy resolution, they can have a strong impact on the performance of the pulse shape analysis. In fact, this analysis must be performed on the unfiltered original signal because any filtering will cancel out the variations in the shape of the rise time, which contain the information on the position of the interaction. This is easily understood from the example reported in the upper panel of Figure 5.5, showing a 10 MHz disturbance modulated with a repetition period of 50 kHz. If such a large perturbation happens at the same time of the detected event, it will sum with the actual signal, spoiling completely its shape.

These qualitative observations can be quantified by means of the Fourier analysis of the signal. It is clear that due to the perturbation by the large exponential-tail signals this analysis should be performed in the absence of real interactions.

5.2.1 Application of the Fourier Transform to Characterize the Noise of the System.

The basic idea behind the Fourier analysis is that any function $f(t)$ can be represented as series of properly weighted sine and cosine terms. In other words, the time-domain behaviour of the function is expressed by the amplitude of the frequencies of the Fourier series and the two representations are equivalent. The use of one or the other representation is just a matter of convenience and depends on what one wants to study. If the goal is to represent periodic features of the signal, the frequency domain is better, while the time domain is more useful to determine the sudden arrival of a pulse or its amplitude. The formulas to go from one representation to the other are:

$$f(t) = \int_{-\infty}^{\infty} F(w) e^{2\pi i w t}\, dw \tag{5.5}$$

and

$$F(w) = \int_{-\infty}^{\infty} f(t) e^{-2\pi i w t}\, dt \tag{5.6}$$

where $F(w)$ is Fourier transform or frequency spectrum of the pulse which can be obtained by inversion of equation 5.5.

The use of Fourier transform methods is quite common in physics and there are essentially four different variants, depending to whether the signal is continuous or discrete and whether it is periodic or a-periodic. These two features can be described as illustrated in Figure 5.6. In this thesis mainly the Discrete Fourier Transform (DFT) has been used which is introduced in the next subsection.

5.2.1.1 Discrete Fourier Transform

The Discrete Fourier transform (DFT) is used with digitized signals with a finite number of samples. This transform maps a discrete periodic sequence $f[k]$ with the integer k ranging over N to another discrete sequence $F[j]$ of the same length, according to the following expressions:

$$F[j] = \sum_{k=0}^{N-1} f[k] e^{2\pi i k j/N} \qquad 0 \leq j \leq N-1 \tag{5.7}$$

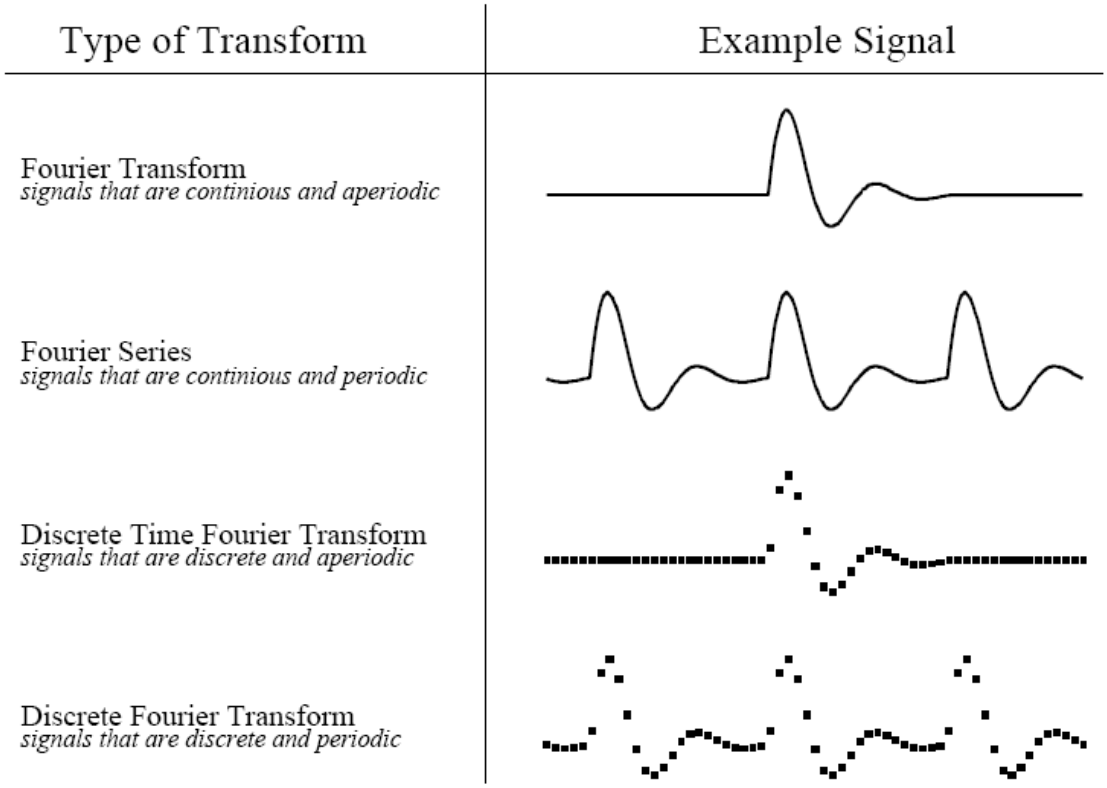


Figure 5.6 Four possible variants of the Fourier transform (Smith, 1999).

$$f[k] = \frac{1}{N}\sum_{j=0}^{N-1} F[j]e^{2\pi ikj/N} \qquad 0 \leq k \leq N-1 \tag{5.8}$$

The explanation of equation 5.7 and 5.8 is that, at point k, the sequence value $f[k]$ is a linear combination of the values of N sinusoids, $e^0, ..., e^{(2\pi/N)k(N-1)}$. The amplitudes of the sinusoids are $F[0], ..., F[N-1]$ respectively, and their frequencies are j/N cycles per sample or $2\pi j/N$ radians per sample (where $0 \leq j \leq N-1$) (Shatkay, 1995).

According to the Nyquist theorem ((Nyquist, 1924)) the maximum measurable frequency is one half of the sampling frequency, corresponding to 50 MHz for the TNT2 digitizers used in this thesis. Given that the bandwidth of the AGATA preamplifiers is limited to about 10 MHz, this is more than sufficient.

The frequency resolution of the transformed spectrum depends on the sampling frequency and on the number N of samples of the input signal. For the TNT2 digitizers, this is $100MHz/N$. Therefore, to have a frequency resolution of 1 kHz we need 10^5 samples. As the maximum length of a recorded trace is 10^6, the minimum detectable frequency is

100 Hz, which is low enough to see the microphony of the detector.

5.2.1.2 Fourier Analysis of Signal Noise and Disturbances

To determine the noise characteristics of the signals from the detectors, the data should be digitized and care has to be taken to be as free as possible from real detected gammas because their large amplitude would cover the details of the noise. This is usually done by removing the radioactive sources and by surrounding the detector with some lead shield, reducing the background gammas from the surrounding environment according to its thickness. Of course, as it is impossible to reduce the signal "background" to zero, some recorded traces have to be discarded and this is done automatically by the analysis programs.

As explained before, the AGATA detectors must be free of noise both at low and at high frequency. A typical frequency spectrum, such as the one presented in Figure 5.7, shows instead a series of spurious peaks that must be removed as much as possible.

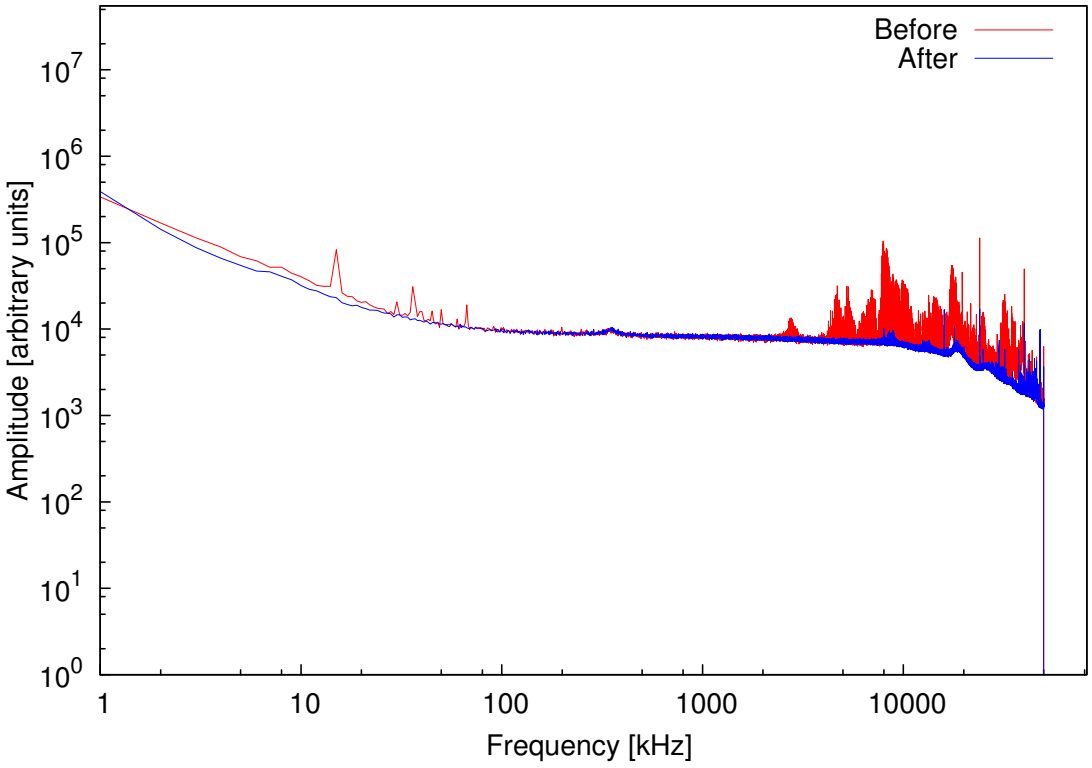


Figure 5.7 Improvement of Fourier spectra of the detector obtained by better grounding and filtring.

The lowest part of the spectrum is studied by recording the longest possible traces (1 M samples, corresponding to a resolution of 100 Hz) and the main sources of noise are connected to some microphony of the detector, mostly induced by boiling and bubbling of the liquid nitrogen (LN_2) used to cool it. The microphony is due to the mechanics of the cryostat and there is not much that we could do to reduce it. Fortunately, the main component for the S001 detector is at $\sim$ 700 Hz (not visible in Figure 5.7, which is limited to 1 kHz), low enough to be effectively suppressed by the base line restorer of the amplifier.

The high frequency disturbances are important for the PSA and are usually reduced by increasing the grounding and/or adding some inductance to the cables from the low voltage power supplies.

The two components of Figure 5.7 correspond to the spectrum before and after such a treatment.

5.3 Work on the Detector

As introduced in previous chapters, the AGATA detector is more complex than any previous detector used in γ-ray spectroscopy and it not surprising that the increased complexity can be the source of new problems that should be understood and solved. One general problem is that the amount of data and the complexity of data management is much bigger than in the past. More specifically and clearly connected to the fact that the detectors are segmented, is the crosstalk between the many electronics channels and the so-called "bow effect" corresponding to some amount of charge loss affecting interaction events that take place very close to the segmentation lines. These effects are not evident in the original spectra of the segments and of the core because, due to unavoidable differences in the analogue parts of the electronics, they have different energy gains which must be compensated before being able to perform any detailed comparison. The energy calibration procedure is described in the next sections.

5.3.1 Spectra Alignment

The standard non-segmented Germanium detectors provide the energy of the incident gammas from the amplitude of the signal collected in the central contact (the anode for n-type crystals). The new generation of segmented detectors produce signals from the central core and also from each of the segments of the external cathode.

When the incoming gamma is absorbed in a single interaction, the output of the electronics will be a signal in the core and a signal in the segment collecting the charge. As it has been shown before, there are transient signals also in the neighbours of the charge-collecting segment but these do not produce an energy value. In fact, because of their very short duration, their amplitude is averaged to zero by the long shaping time of the energy filter. Obviously, the energy determined from the core should be the same as that seen by the only net-charge segment.

When the gamma is absorbed in multiple hits, the generated charges can be collected in different segments and it is to be expected that the sum of the individual energies gives the same value as the core.

In all cases, instead of only one, the segmented detector provides two energy values. Therefore, we can use the one with the best energy resolution or, as shown at the end of this work, we can combine them to produce a better value.

Summing the energy of the segments is not as simple as it might first appear. In general, each spectrum has different gain or/and zero-offset which means that the same energy peak will be in different positions in the various segments (Figure 5.8).

A simple correction is done by looking at the peaks obtained from a well known radioactive source, like ^{60}Co or ^{152}Eu. These peaks, corresponding to events where the incoming gamma releases its energy in only one segment, can be moved to the same place by applying a linear correction (Eq.5.9) where the coefficients a_i and b_i are specific of each segment and are determined by fitting the position of at least two known peaks (e.g. from the ^{60}Co source)

$$E_i = a_i + b_i.ch_i \tag{5.9}$$

The term a_i is due to offsets in the amplifier-ADC electronics and is normally present in analogue systems. With digital electronics, where the amplitude of the signal is the

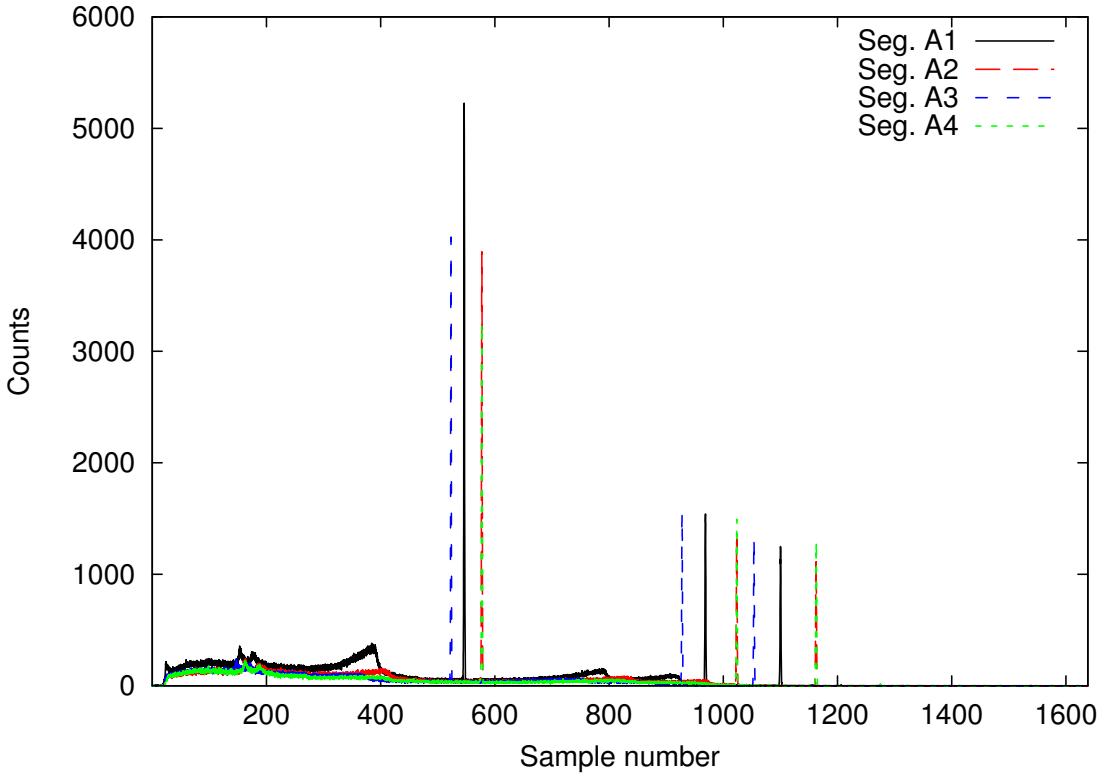


Figure 5.8 Energy spectra of different segments before gain alignment.

difference between the flat-top of the trapezoid and the base-line the value of this term is usually very small and it is convenient to assume that it is exactly zero.

The results of the alignment procedure can be seen in Figure 5.9. Clearly, the peaks are now in the same position for all of the segments as it was expected.

The coefficients obtained by the calibration procedure can be applied to stretch the spectra to the desired common position but it is more productive to apply them event-by-event to the individual increments (by analyzing again the same data if this has been stored or for new data taken afterwards) so that in future the produced spectra are already gain-matched.

Of course now we can also sum together the gain-matched energy values from the segments fired by every specific event and build the energy spectrum of whole crystal. This procedure is called (event-by-event) add-back and the obtained sum-spectra are shown in Figure 5.10. Although we are summing energy-calibrated data, the peaks in the sum spectra are in different positions in a way that is clearly dependent on the number of fired segments (fold).

There are two conclusions we can draw form this results: either the coefficients determined from single-segment events are not valid for multi-hit events, or there are some other effects on the amplitude of the signals that are seen only when more than one segment is fired. The first conclusion is against intuition because, although not detectable, multiple-hit events exist also in non-segmented detectors where the total spectrum is free from such shifts.

The more reasonable explanation seems to be the second one, and, indeed, the fold-dependent shift of the peaks is interpreted as a crosstalk in the electrically-coupled system of the 36 segments and the core.

5.3.2 Explanation of the Crosstalk.

In electronics, the term crosstalk refers to undesired effects of a signal generated and/or transmitted in one part of a circuit on other signals in other parts of the system. Such effects are caused by capacitive or inductive coupling from one circuit or channel to

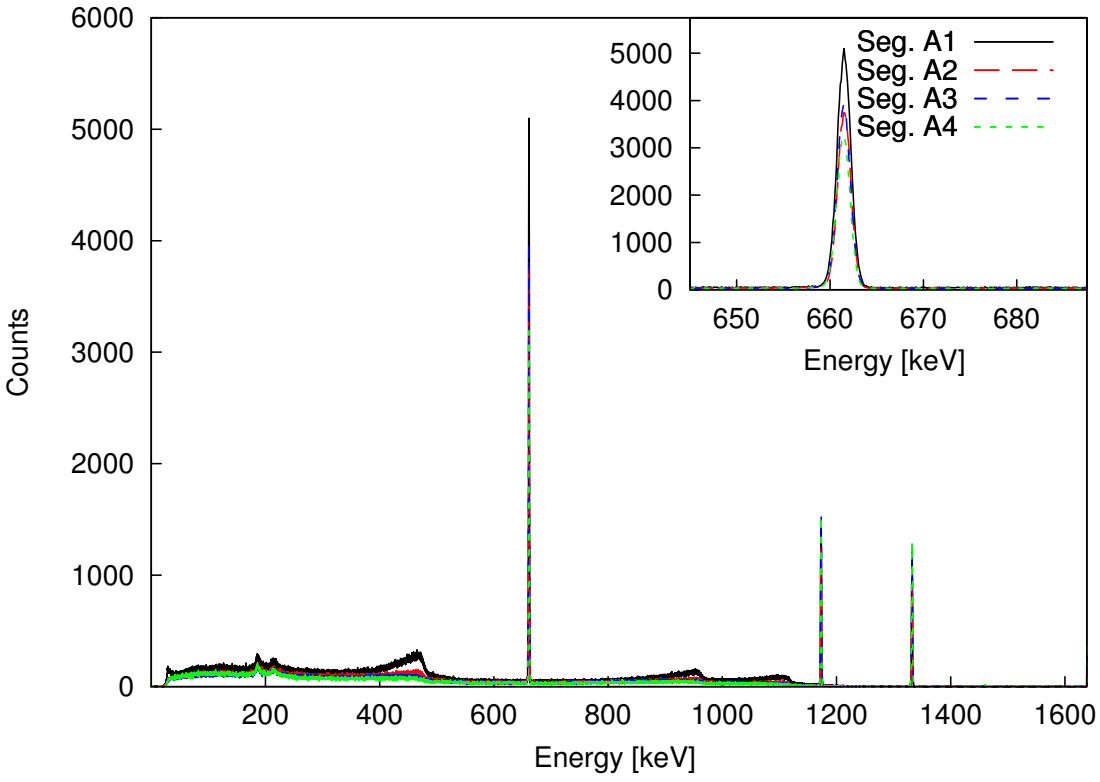


Figure 5.9 Gain matched spectra for single-segment events.

another.

The evolution of the detector technology is going in the direction of smaller and more densely packed detectors. As in such systems the coupling between adjacent channels is big and the signals tend to be smaller, the treatment of the crosstalk effects become a relevant issue. This is in fact the situation of the AGATA detectors with their 36 segments and core signals influencing each other. Clearly, also the transient signals that are generated in the neighbours of the net-charge segment are due to mutual influences between the channels. However, as this influence is part of the physics of the detection and provides useful information, it should not be mixed with the crosstalk, which is just a useless and annoying complication.

Crosstalk in large-volume highly-segmented germanium detectors was observed first on the MARS prototype (Venturelli et al., 2002). A similar crosstalk behaviour is of course observed in all other segmented germanium detectors like MINIBALL (Bruyneel et al., 2006), TIGRESS (Svensson et al., 2005) and SEGA (Mueller et al., 2001).

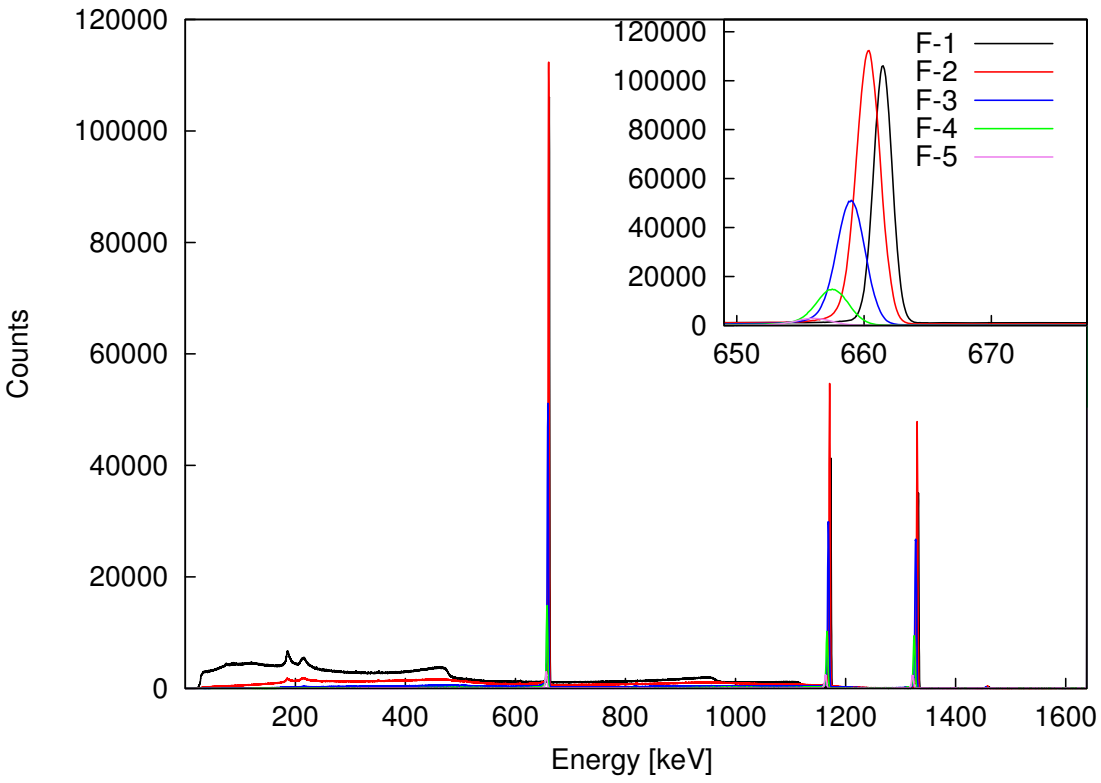


Figure 5.10 Summed spectra of multi-segments events, the shift of the inset due to the Crosstalk effect

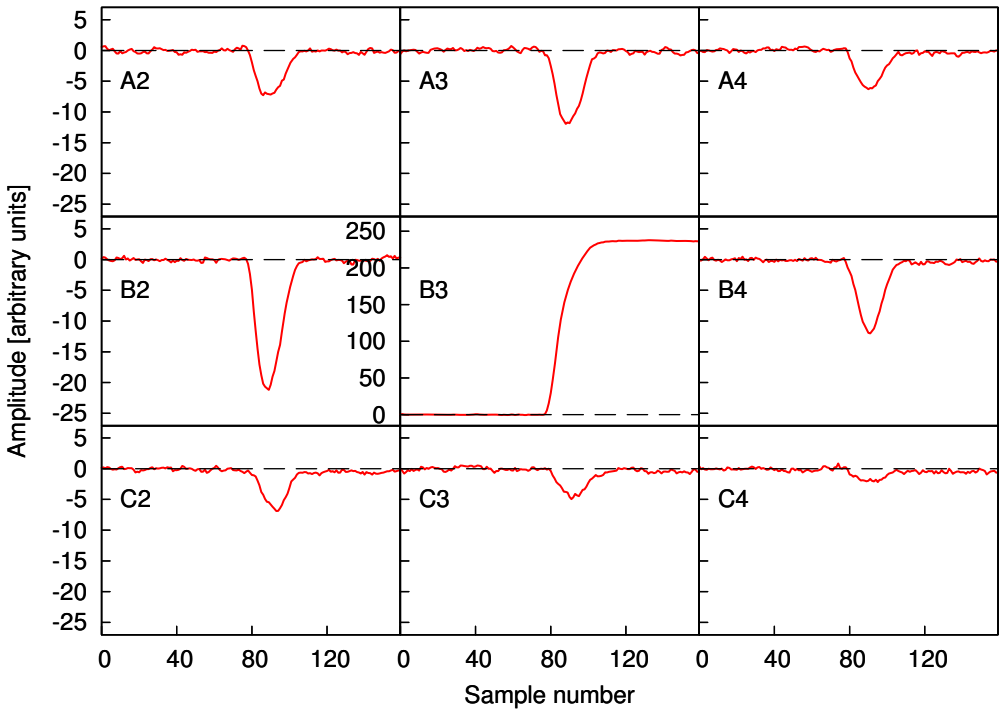


Figure 5.11 A single segment event with a 1.3 MeV ^{60}Co gamma detected in segment B3. The surrounding segments see the expected transient signals. Crosstalk is presented but difficult to appreciate.

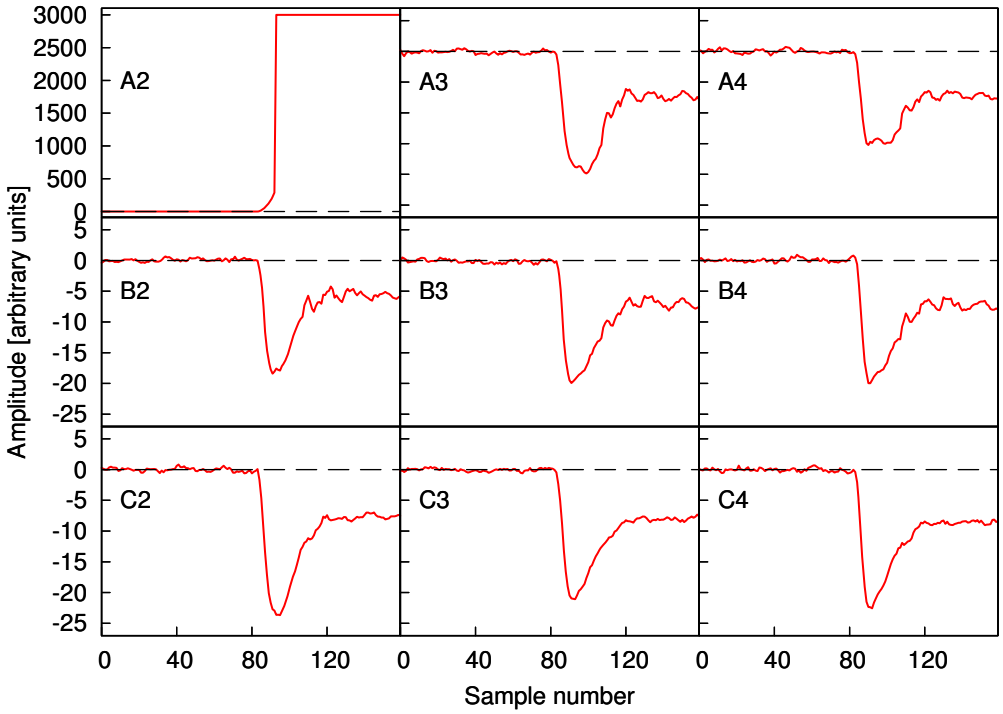


Figure 5.12 A very large signal detected in A2 induces transient in its neighbours. The non zero amplitude after transient is the effect of the crosstalk.

The characteristic feature of crosstalk is easily seen in Figure 5.11 and Figure 5.12. When a signal is collected in one segment we know that the other near segment should see the transient signals which are present only during the collection time. The mid panel of the Figure 5.11 corresponds to the detection of a 1.33 MeV gamma in segment B3 and, as expected, the neighbours have only the small transient signals. Figure 5.12 corresponds to the detection of a very large signal (probably a cosmic ray) which saturates the electronics in the charge collecting segment(s) and generates very large transients in the neighbours. In this case, it is clear seen that the signal in the neighbours does not finish with the transients but stays at a negative level. As this level returns to zero with the characteristic decay time of the preamplifier ($\sim 46\mu s$ for the AGATA detectors) it is completely equivalent to a negative net-charge signal of the seen amplitude and the (analogue or digital) amplifier will generate a negative value. Figure 5.12 is an extreme case but the negative component is present also in Figure 5.11 with the same ratio of amplitudes. The fold-dependent energy shift of Figure 5.10 is intuitively explained by the fact that every segment participating in the sum contributes its small negative amplitude due to the other ones.

The quantitative explanation of the effect is done following a linear model proposed by Bruyneel (see (Bruyneel et al., 2008)). In this model, the main component of the crosstalk is has a relative amplitude of $\sim 0.1\%$ and is due to the AC-coupled core preamplifier. This model shows also that between adjacent segments there is a smaller segment-to-segment coupling of opposite (i.e. positive) with relative amplitude of $\sim 0.04\%$ that counteracts the main component.

5.3.3 Correction of Crosstalk.

As it is indicated before, the relationship between measured amplitude and energy of the interaction is just the scaling factor derived in the energy-calibration procedure.

$$E = B \cdot A \tag{5.10}$$

If crosstalk is not an issue ,this is valid independent form the number of segment participating in the specific event and can be expressed in compact form by considering E and A as vectors and B as a diagonal matrix of calibration coefficients. The total energy

of the event is given by summing the energy of all fired segments (In principle the sum could be done on all segment of the detector but the non-fired segments would contribute to the sum with their noise disturbing the energy resolution of the total signal).

The existence of crosstalk has the consequence that the energy obtained from the Fold-1 calibration is perfect (by construction) for single events but only an approximation for higher fold events: to be able to obtain the total energy of the event as sum of the measured values, these values must be adjusted (re-calibrated). Assuming that the electronics and the crosstalk effects are linear, the needed recalibration can be obtained by expressing the result of a generic interaction event with "real" energy in the various segments of the detector as :

$$\begin{bmatrix} E_{Seg1} \\ E_{Seg2} \\ E_{Seg3} \\ \dots \end{bmatrix}_{Measured} = \begin{bmatrix} 1 & \delta_{12} & \delta_{13} & \dots \\ \delta_{21} & 1 & \delta_{23} & \dots \\ \delta_{31} & \delta_{32} & 1 & \dots \\ \dots & \dots & \dots & \dots \end{bmatrix} \cdot \begin{bmatrix} E_{Seg1} \\ E_{Seg2} \\ E_{Seg3} \\ \dots \end{bmatrix}_{Real} \tag{5.11}$$

This is an identity for Fold-1 events and our problem is to find the $N \cdot (N-1)$=1260 off-diagonal coefficients. Once the "crosstalk correction matrix" is determined we can apply its inverse to the vector of "measured" energies and obtain the "real" energies, which can than be directly summed to get the correct total energy. The fact that our crosstalk produces an energy deficit implies that the off-diagonal coefficients of the eq.5.11 matrix should have a small negative value. For the same reason, the coefficients of the inverse matrix used for the actual calibrations will be small and positive.

The normal way to derive the coefficients is to produce peaks in the sum spectra of higher fold events and to determine how much they are away from the "known-energy" position. For a segmented detector with N segments there are $\binom{N}{i}$ possible sum spectra for each fold i. With 36 segments the 1260 off-diagonal coefficients must be provided by the 630 pair spectra, 7140 triple-spectra and so on. It is clear that so many spectra cannot be analyzed by hand. Furthermore, as the full energy events seen by the detector are spread into so many possible combinations it will take a lot of time to collect enough events to produce analyzable peaks.

a-Coefficients from Fold-2 events: Following Venturelli (Venturelli et al., 2002), the crosstalk matrix is assumed to be symmetric and the 630 correction coefficients are

derived using the peaks observed in the 630 Fold-2 sum spectra. The peak in the (i,j) sum spectrum is observed at an amplitude of $\overline{E}_{ij}$ which is smaller than the real amplitude E_{ij} by an amount Δ_{ij}. For this pair 5.11 gives

$$\begin{aligned} \overline{E}_i &= E_i + \delta_{ij} \cdot E_j \\ \overline{E}_j &= E_j + \delta_{ji} \cdot E_i \end{aligned} \tag{5.12}$$

with the assumption $\delta_{ij} = \delta_{ji}$. The measured sum is

$$\overline{E}_{ij} = \overline{E}_i + \overline{E}_j = E_i + E_j + \delta_{ij} \cdot (E_i + E_j) = E_{ij} + \delta_{ij} \cdot E_{ij} \tag{5.13}$$

The energy deficit Δ_{ij} is

$$\Delta_{ij} = E_{ij} - \overline{E}_{ij} = -\delta_{ij} \cdot E_{ij} \tag{5.14}$$

Hence

$$\delta_{ij} = -\frac{\Delta_{ij}}{E_{ij}} \tag{5.15}$$

where it is again seem that the diagonal coefficients of the direct matrix are negative.

b-Coefficients from negative energy peaks: A more clever way of obtaining the off-diagonal events was suggested by Bruyneel and derives by observing the result of expression 5.11 when applied to an event with only one segment fired. Assuming that this is segment 1 we get the array of values $E_1, E_1\delta_{12}, E_1\delta_{13}...$

Considering that the off-diagonal elements of the crosstalk matrix are negative, all the "other" segments should see a small negative energy. In a classical data acquisition system, the output of these segments would be discarded because the detection threshold is usually set positive above the noise level. However, in the TNT2 based system described in section 5.1.1 all segments are forced to produce an output when a local trigger is generated. So, besides the normal positive value of the net-charge segment(s) there is an output (slightly negative, according the model) also for all the other segments. As shown in Figure 5.14 this is really what happens. This figure shows a 2-dimensional energy spectrum for the 3 combinations of segments A1-A2, A1-A3 and A1-A4 by selecting single-segments events with energy released only in segment A1.

The spectrum of A1 has the expected shape of the ^{152}Eu source, used for the test; the distribution of points along the vertical axis for the other 3 segments is not centred on zero

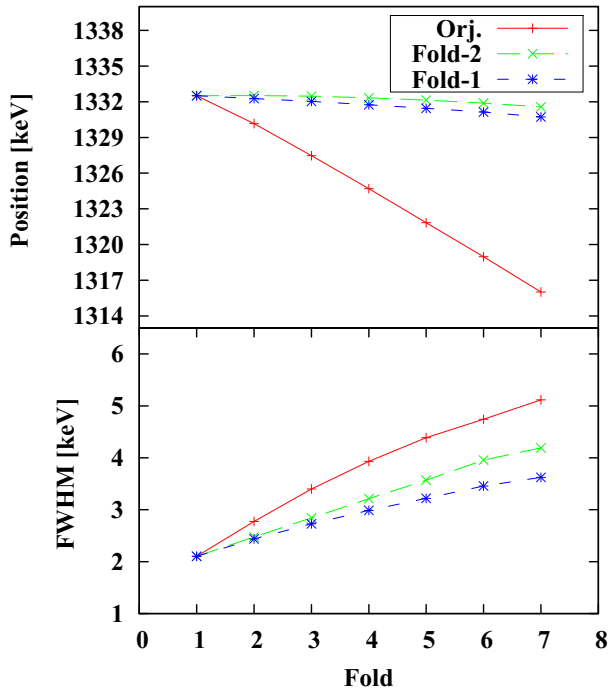


Figure 5.13 Comparison of the two crosstalk correction methods for 1.3 MeV of ^{60}Co source. The label Fold-1 refers to using the coefficients extracted from the negative energy peaks and label Fold-2 refers to using Fold-2 events.

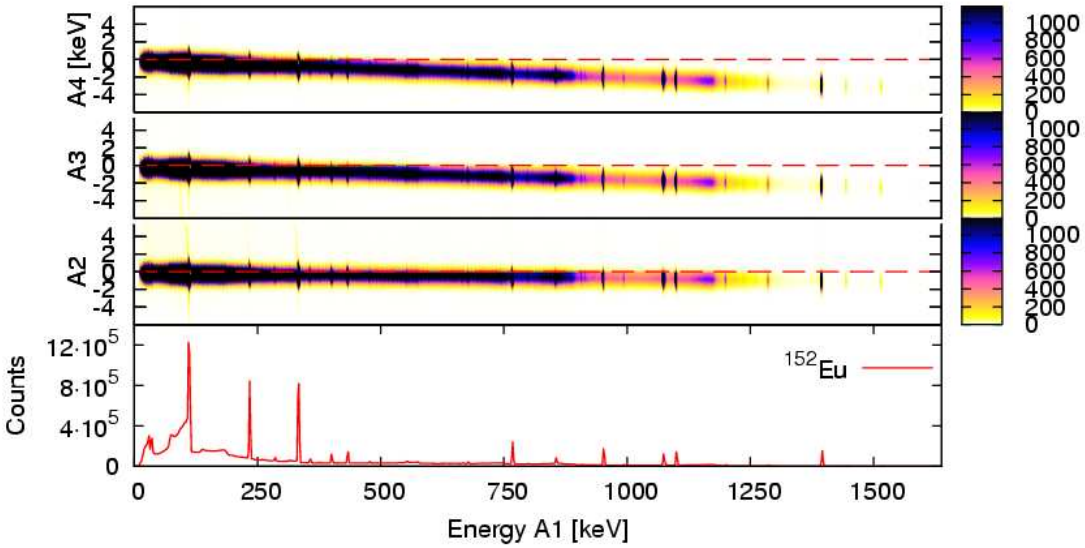


Figure 5.14 The Correlation matrix of A1 vs A2, A3 and A4 has a “negative energy” region in the segments A2, A3 and A4. The zero energy in the A2-A3 and A4 segments is marked by the red dashed line.

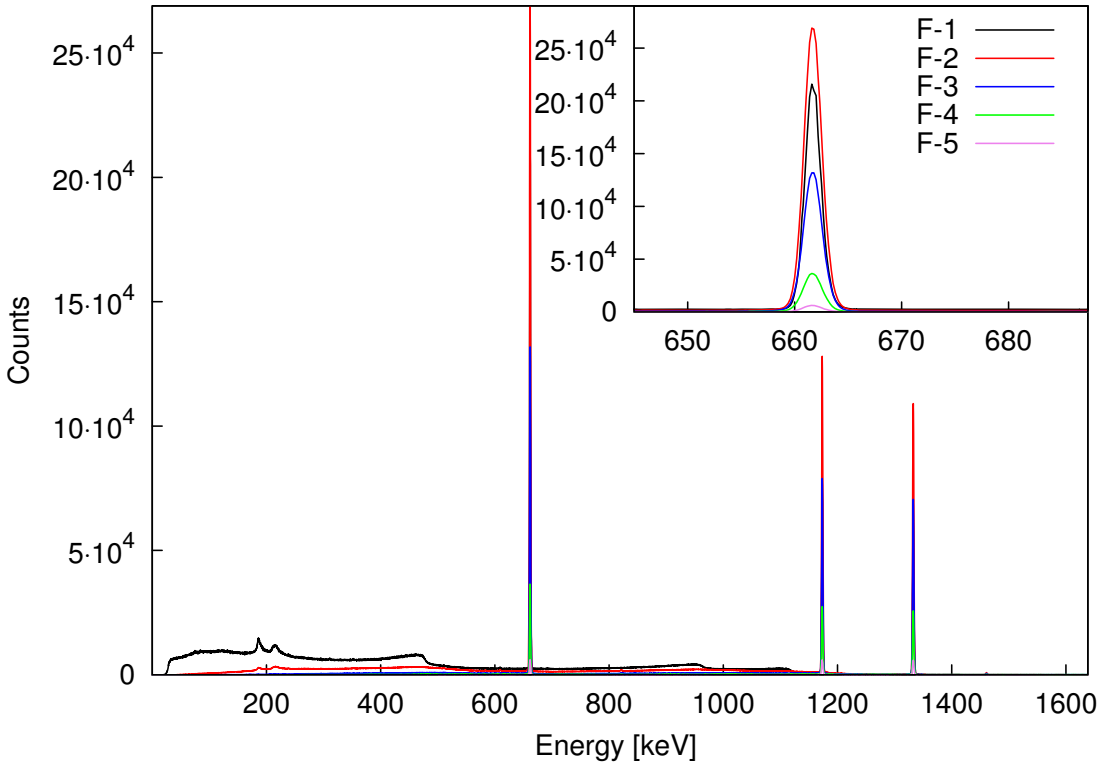


Figure 5.15 Crosstalk corrected sum-energy spectra for different numbers of fired segments.

(noise) but is slightly negative, with amplitude proportional to the energy seen in segment A1. The slope of this correlation is a direct measure of the $A1 - A_i$ crosstalk matrix element. The actual value of the coefficient is obtained by dividing the amplitude of the "negative-energy" peak by the amplitude of the peak seen in the fired A1 segment. The automatic calibration procedure produces the [hit-segment, other segment] correlation matrix for all possible 1230 combinations and the coefficients of the crosstalk matrix are obtained by an automatic fit of the "negative-energy" peaks. This direct method is now preferred to the one using the Fold-2 sum spectra because it does not need to assume that the matrix is symmetric. Besides, it is much faster because every single-segment event produces one increment all other 35 segments. The quality of the correction is good as seen from Figure 5.15 where now the sum-energy peak is in the same position for all segment folds. Another way to see this, is that after applying the correction to the [hit-segment, other-segment] single-hit matrices the correlation is exactly on the y=0 axis, Figure 5.16.

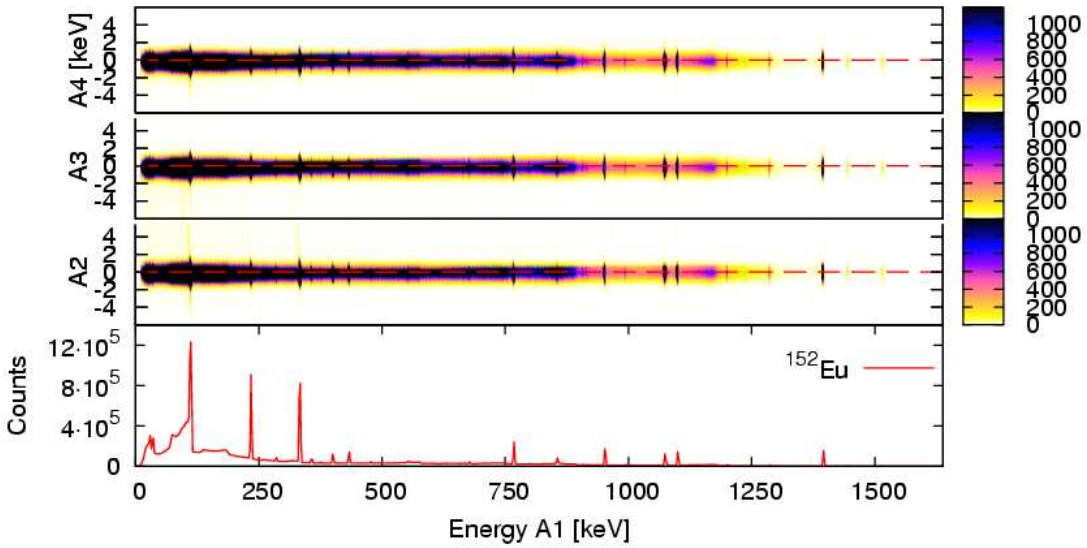


Figure 5.16 After crosstalk correction, the amplitude in the ”other” segments is 0 and lies on the y=0 axis.

5.3.4 Charge Sharing and the Bow Effect

As introduced in Chapter 2, charge sharing can happen if the incoming radiation interacts with very close to the border between the two segments, where the direction of the electric field lines changes form one to the other segment. Given that the resulting cloud of electrons and holes has a non-null size, a part of these charge carriers can be attracted to one of the segments while the rest goes to the other. Considering only the resulting net-charge signals in the two segments, it is not possible to distinguish this kind of events from events with two real interactions in the two segments. It is clear that this feature is a problem because the γ-ray tracking algorithms will try to reconstruct a single interaction event as double interaction one.

Figure 5.17 shows the usual $\gamma-\gamma$ correlation matrix for the neighbouring segments A1 and B1, using a weak ^{152}Eu radioactive source positioned very close to the inter-segment separation. The dominant characteristics of this matrix are the cross-diagonal lines corresponding to full-absorption of a specific γ-ray with one Compton scattering interaction in one segment and a full absorption of the scattered gamma in the other segment.

The vertical and horizontal lines are events with two different gammas detected si-

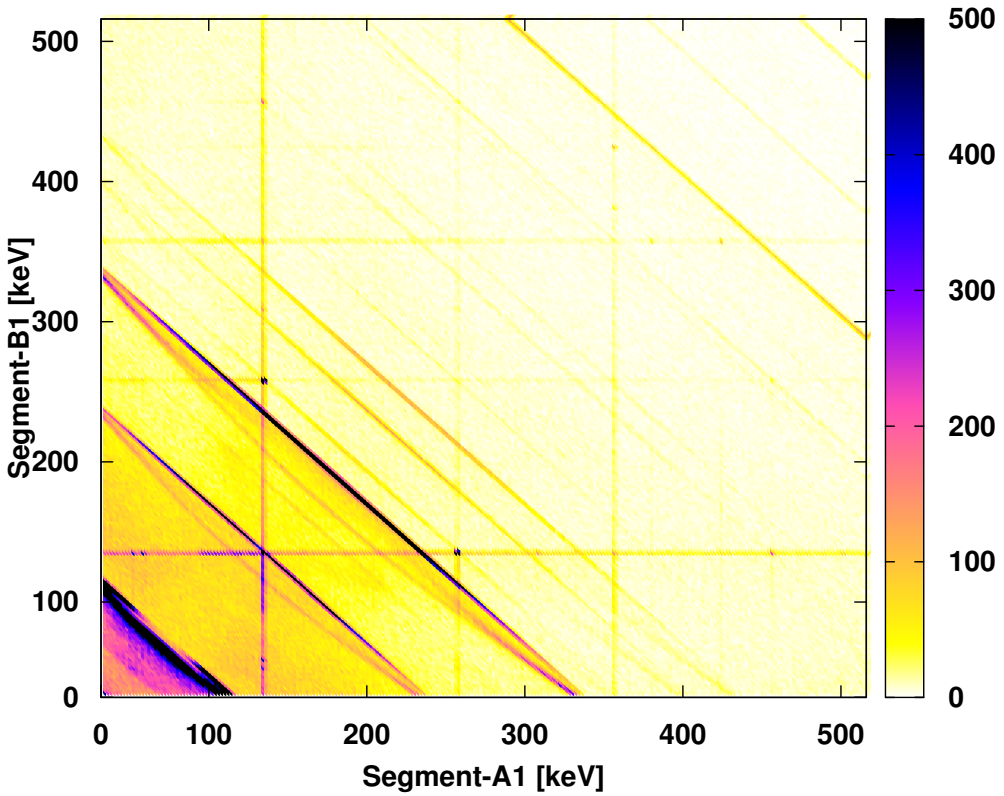


Figure 5.17 Low-energy part of the γ-γ correlation matrix produced by a ^{152}Eu source in the front neighbouring segments A1-B1. The strong bow structures correspond to gamma rays that are fully absorbed by a photoelectric interaction in close vicinity of the segmentation line. The cloud of generated charge carriers (holes) splits between the two collecting segments and is partly lost to the signal amplitude.

multaneously in the two segments. These can be two gammas emitted in cascade by the ^{152}Eu source (e.g.121 keV and 244 keV, 121-1408 keV, 344-778 keV) or two gammas that are emitted by two different decays taking place very close in time. In both cases one gamma can be fully absorbed in one of the segment (e.g 121 keV in A1) while the other releases only part of its energy in the other segment. If both lines are fully absorbed in the two segments the coincidence shows up as a 2-dimensional spot (e.g. 244 keV in A1 and 121 keV in B1).

What is unusual in is the persistence of the cross-diagonals down to very low energy. As the dominant detection mechanism below $\backsim$ 200 keV is photoelectric absorption in one single interaction, only one segment should see a signal and the lower left corner of the segment-segment correlation matrix should be essentially empty. The fact that it is not empty means that both segments were fired and we must conclude that they shared the full amplitude of the single possible interaction.

By looking more carefully to the Figure 5.17 it is possible to see another type of



Figure 5.18 Types of charge collection that can take place for a γ-ray interaction event that occurs between two electrodes. The charge can be (middle) completely collected by either electrode, or can be shared (right) between the two electrodes. Some part of the charge can also be collected to the surface between the two electrodes.

correlation that is not expected both for real two-segment events and also for single hits with charge sharing. This correlation is in the extra-intensity to the left of the cross diagonal: the events sitting in this "bows" are close enough to the cross diagonal line to be classified as real full-absorption double hits (or single hits with charge-sharing) but it is clear that they are missing part of the released energy.

A convenient explanation of this phenomenon can be found, for instance, in the work by Amman (Amman and Luke, 2000) and is sketched in Figure 5.18. An interaction within the crystal releases a cloud of electron-hole pairs. The electrons drift towards the non-segmented core contact while the holes move towards the segmented cathode. In most of the cases the holes are collected by one or the other segment and are therefore assigned as an event in that segment (Figure 5.18, left and centre panels). But if the interaction takes place very close to the separation line, the cloud of holes can be split in two parts and end-up in both segments (Figure 5.18, right panel). It should be remarked that in the inter-segment region the electric field is rather week and its direction is mainly transverse. This means that the drift velocity of the holes is small, giving more time to the charge cloud to expand by diffusion and reinforcing the probability of charge sharing. Furthermore the motion can be so slow that part of the holes will not be collected within the time of the energy-processing shaper, resulting in a (ballistic) deficit of the amplitude of the signals.

This simple model explains the fact that very low energy γ-rays, which cannot pene-

trate very deep into the detector where the electric field is stronger, are assigned as events in both segments. In this case the full energy signal can be recovered by summing two segment signals, corresponding to the typical diagonal. Furthermore, the model explains the bows as the consequence of very slow charge collection, resulting in a deficit of the sum-signal.

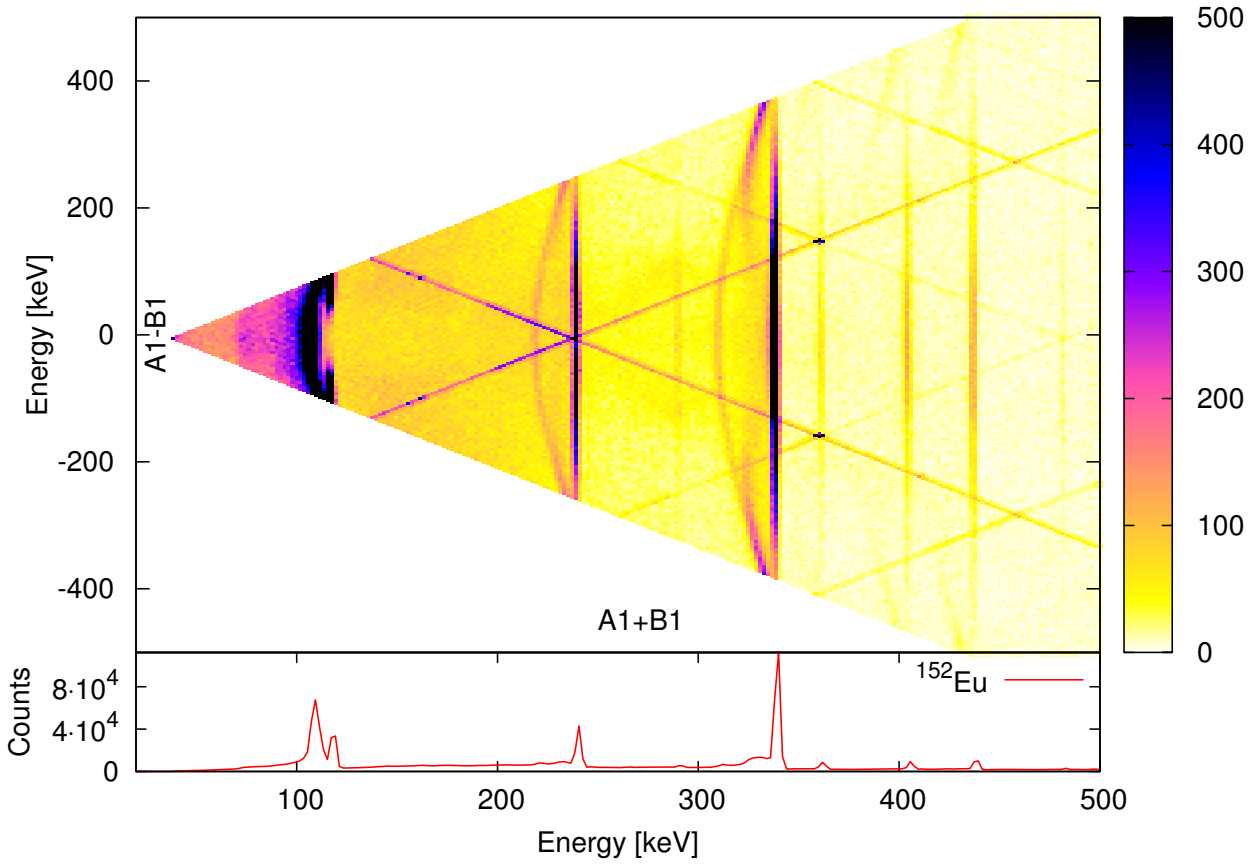


Figure 5.19 Sum of the γ energies vs. the corresponding difference. The bow effect is very strong in the front segment.

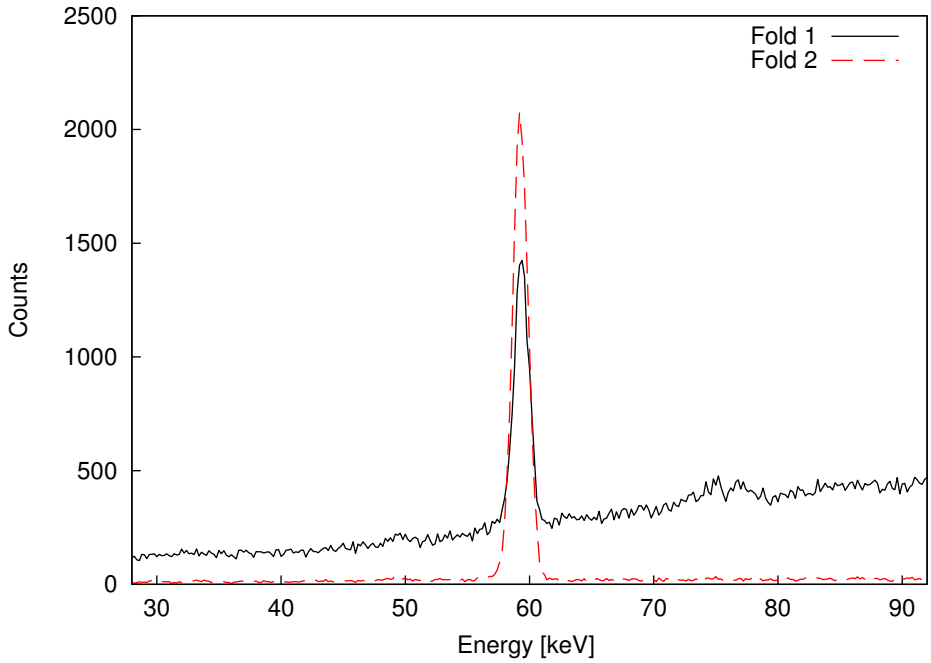


Figure 5.20 The spectrum of the core for fold-1 and fold-2 events with the collimated source at the center of the segmentation line. No charge loss is seen.

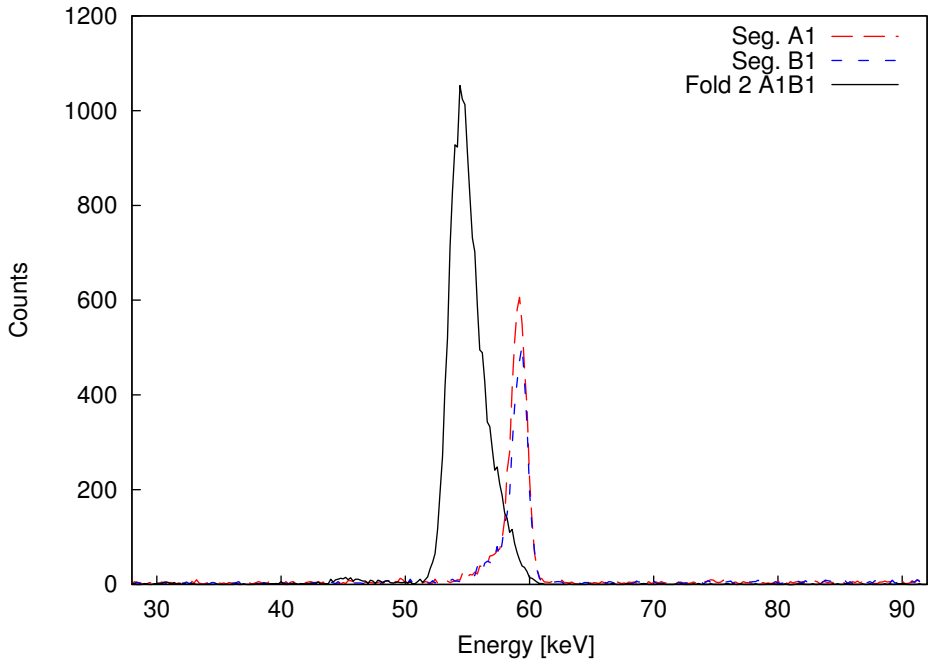


Figure 5.21 Statistic for interaction in segment A1, B1 and A1B1 can be seen in figure. Events which has been accepted as a two segment interaction has a lot of counts but the position of the peak is shifted due to uncollected charges.

The effect of the missing charge is seen clearly in the sum-energy spectrum which is presented as the vertical projection of the matrix of Figure 5.19. This matrix is obtained from the (A1,B1) matrix of Figure 5.17 by the transformation (x+y, y-x), which corresponds to a 90 degrees clockwise rotation. It is evident that the shape of the low energy lines is completely distorted by the tails due to charge losses; at 121 keV the peaks has split into 2 components, producing a very strong spurious line at 111 keV. It is clear that, making good experiments in such a situation is practically impossible.

The energy-loss effect observed in the segment-sum spectra should, in principle, be seen also on the core. This is because the signal formation at the electrodes is due to the charge induced during the collection of the charge carriers. Therefore, if there is lost charge (or very slow collection with respect to the shaping time of the amplifier) this should be noted on all electrodes.

The fact that the observed core-spectra are practically insensitive to the distance of the collimator to the segment separation line (Figure 5.20 with respect to Figure 5.21, with data taken as described in next section) is because, for interactions taking place at the surface of the crystal, the signal in the core is due essentially only to the motion of the electrons. Being attracted away from the surface, don't feel the problem of splitting.

5.3.4.1 Size of the Segmentation Lines

Since the charge-sharing and charge-loss phenomena can have a strong impact on the overall energy resolution and photo-peak efficiency of the AGATA array, it is very important to determine experimentally the basic parameter on which they depend, namely the effective gap in between the neighbouring segments.

According to the manufacturer, the size of the segmentation line between neighbouring segments should be smaller than 0.1 mm.

The experimental setup, shown in Figure 5.22, comprised the AGATA prototype detector S001 and a collimated calibration source, with a micrometrical movement. A ^{241}Am source (emitting low-energy 60 keV photons for which the average interaction depth in Ge is less than 1 mm) was used in order to produce single interaction points close to the detector surface.

The two different collimators used in our measurements are a 100 mm thick lead

brick with a nominal hole of 1.5 mm radius, and a 50 mm thick iron block with a smaller hole of 0.5 mm radius. The collimator was moved in steps of 0.2 mm in the direction perpendicular to the segmentation line and the area of the 60 keV peak was measured in both segments under study for each of the measured positions. To have the possibility to determine the area of the "bow" the measurements were performed, as described in Section 5.1.3, by triggering on the core signal and forcing the both segments to produce a value. The data was recorded as a list of values for the core and all segments (also those not shown here). The data acquisition time for each point was ranging from 10 minutes to 30 minutes depending on the distance to the centre position and the used collimator. The recorded events were analysed off-line to produce the spectra and matrices reported in the following.

The matrix in Figure 5.23 (left panel) is taken at the centre of the segmentation line, while the one in the right panel is taken in a side position. The fact that the bow is strong on the left panel and rather weak on the left panel is consistent with explanation given before.

The full result of a scan over the A1-B1 separation line in the front face of the crystal is shown in Figure 5.24: the intensity of the 121 keV peak moves from one segment to

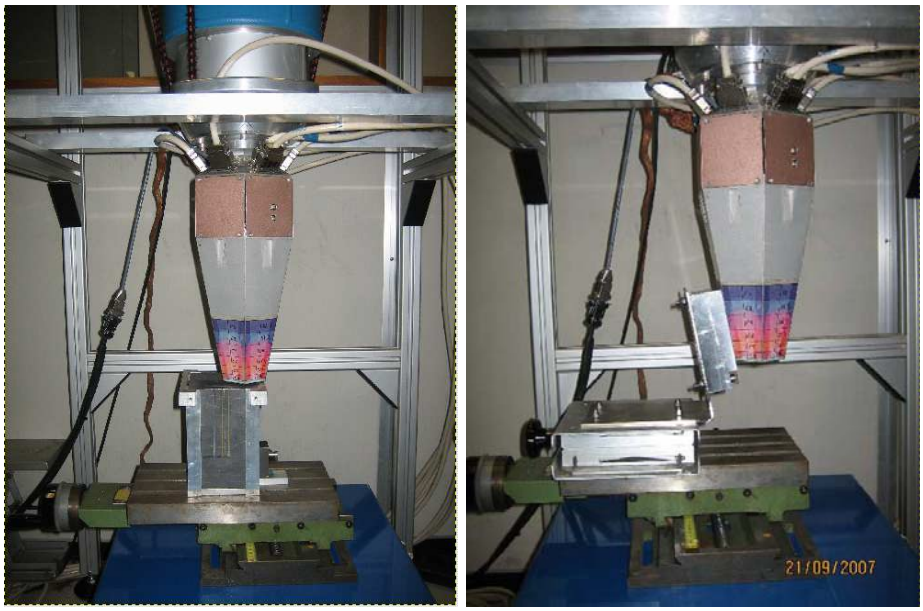


Figure 5.22 The scanning table used to determine the size of the segmentation lines. Front face scanning with a lead collimator (left). Front and side faces scanning with an iron collimator (right).

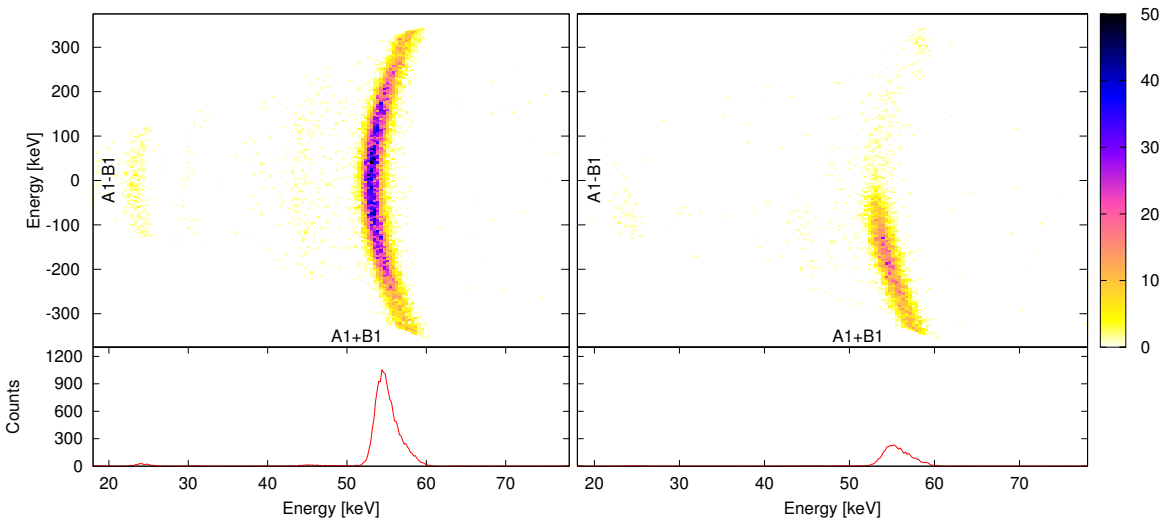


Figure 5.23 Sum of the gamma energies vs. corresponding difference on centre (left panel) and on segment B (right panel) for 60 keV gamma line of the ^{241}Am source.

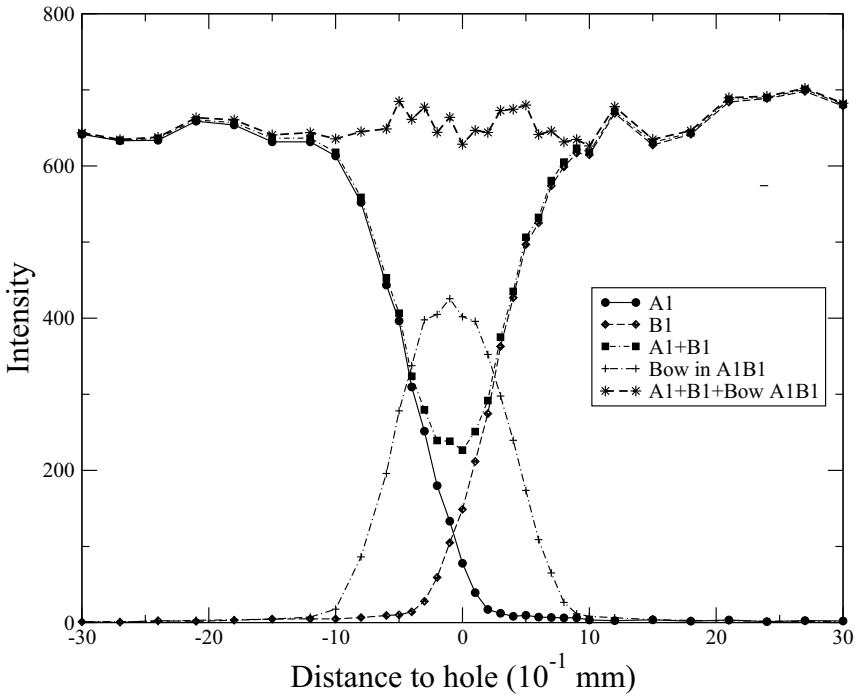


Figure 5.24 Intensity of the 60 keV peak seen in the segments A1 and B1 as a function of the collimator position. Adding the charge sharing (bow) component extracted from the γ-γ matrix, the total intensity is constant.

the other, following the position of the collimator. In an ideal condition the sum of the two values should be a constant. Instead, the sum of the two values drops by about 60% in the central part of the segmentation while the intensity of the "bow" is largest at the centre of the segmentation line. On the other side, the sum of all three components is

constant, confirming that there is no net loss of efficiency but only a change in the type of generated events.

The numerical value of the gap has been determined by fitting the data using a simple model of the collimator-detector arrangement. Assuming that the source has a uniform distribution covering the whole surface of the hole, and given that the thickness of the collimator is much larger than the size of the hole, the gammas enter into the detector as a well defined parallel beam. Knowing from the specifications of the detector that the size of the segmentation line is smaller than the collimator hole, the counts seen by the two segments and the counts in the bow are given by the area of the three regions A, B and AB of the right panel of Figure 5.25.

The intermediate steps of the simple calculation are reported in Eq.5.16, and the final expressions used in the fit are given in Eq.5.17 and 5.18.

$$\begin{aligned} x^2+y^2 &= r^2 \\ y(x) &= \sqrt{r^2-x^2} \\ dA(x) &= 2y(x)dx \\ dA(x) &= 2\sqrt{r^2-x^2}dx \end{aligned} \tag{5.16}$$

where $d(x)$ is a small vertical slices of the circle and dA is its area. The integrated area is than

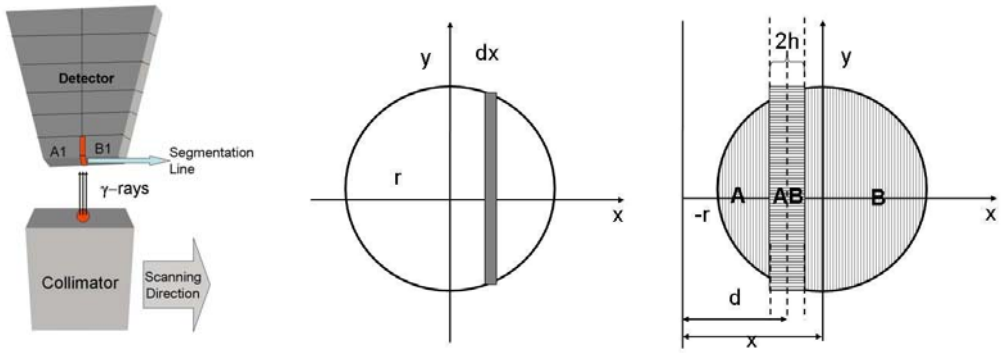


Figure 5.25 Sketch of the scanning system (left) and simple geometrical methods to determined the counts in the two segments and segmentation lines (right).

$$\begin{aligned} A(x) &= 2\int \sqrt{r^2 - x^2}dx \\ f(x) &= x\sqrt{r^2 - x^2} + r^2 arcsin\left(\frac{x}{r}\right) \end{aligned} \tag{5.17}$$

The total area of the regions is given by

$$\begin{aligned} S(A) &= f(x)|_{x-r}^{d-h} \\ S(B) &= f(x)|_{d+h}^{x+r} \\ S(AB) &= \pi r^2 - (S(A) + S(B)) \end{aligned} \tag{5.18}$$

The fit was performed simultaneously on the 3 sets of experimental data using 4 free parameters:

1. position of the hole along the scanning line ;
2. constant value of the sum of the 3 components;
3. radius of the collimator;
4. thickness of the segmentation line.

The size of the collimator hole and thickness of the segmentation lines resulting from the fit of 3 scan measurements (Figure 5.26 and Figure 5.27) are reported in Table 5.1. The quality of the fit is good, as confirmed also by the fact that the obtained value of the collimator holes is close to nominal. The A1-B1 segmentation line in the front face of the detector, where the bow effect is particularly strong, was scanned with both collimators. The obtained values 0.68(1) and 0.72(2) mm are in mutual agreement within the experimental error, but they are much bigger than the 0.1 value specified by the manufacturer.

The A3-B3 side face was scanned only with the iron collimator because of the mechanical difficulty of mounting the heavier lead block. However this should be sufficient because the obtained value is consistent with the specifications of the manufacturer.

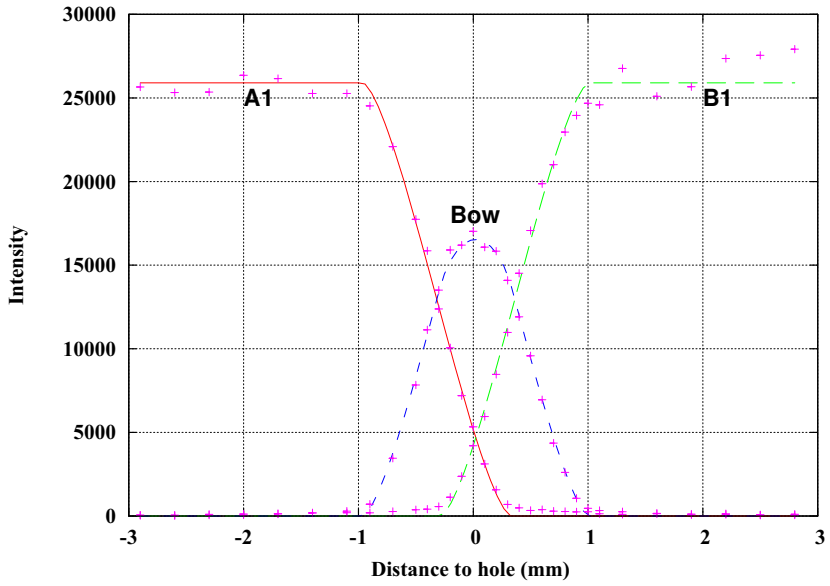


Figure 5.26 Intensity of the 60 keV peak seen in the segments A1 and B1 with fitting curves as a function of the collimator position.

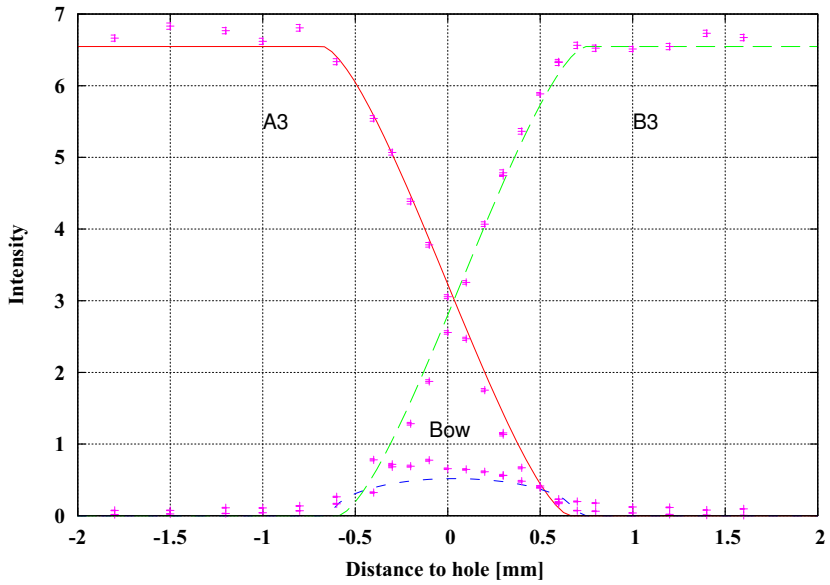


Figure 5.27 Intensity of the 60 keV peak seen in the segments A3 and B3 with fitting curves as a function of the collimator position.

Due to the fact that the procedure used to determine the size of the segmentation lines is not a direct measurement but is based on the position-dependent number of detected events, the obtained values should not be interpreted as geometrical but as “effective” gaps. However the fact that for the front face the effective size is so large is of big

Table 5.1 The relevant geometrical parameters derived from the fit.

Collimator Material	Collimator Radius[mm]	Segments	Gap [mm]
Pb	1.46	A1-B1	0.72(2)
Fe	0.65	A1-B1	0.68(1)
Fe	0.61	A3-B3	0.09(1)

concern. As the front of the crystal is where most of the low energy gamma rays are detected, the large amount of bow-generating gaps has, as shown in Figure 5.19 important consequences on the quality of the spectra.

5.3.4.2 Correction of the Bow Effect

The fact that the charge-loss is affecting the segments much more that the core, allows to develop a practical correction procedure to restore the shape of the segment-sum spectra.

Without charge loss, the value measured by the core should be (up to the energy resolution) equal to the value of the segment sum. In a 2-dimensional representation the events should then lie on the main diagonal of the matrix. Of course, the events will lie on the main diagonal also if both values are reduced by the same amount. If one of the two values is reduced much more than the other, the corresponding event will be out of the main diagonal at a distance proportional to the energy difference.

Figure 5.28 shows the [core, A1+B1] matrix for a measurement with a non-collimated ^{152}Eu source positioned in front of the detector. As expected, we see the 45 degrees diagonal but there are also many events below it, for which the value of the segment-sum is lower than the value of the core. By looking more closely to the inset of the figure it is clear that there are also some events above the main diagonal ($E_{Core} < E_{A1} + E_{B1}$) but they are not considered here because their intensity is small.

If the core would be completely unaffected by the charge loss problem, the shape of the off-diagonal structures in correspondence of the sharp lines of the energy spectrum should be completely vertical.

However it is clear that these structures have an inclination and this means that also the

core has some energy loss. The tilting of the off-diagonal lines gives the relative influence of the charge-loss problem on the two signals.

For the correction procedure described in the following, the detected events are separated into "good" events lying on the main diagonal (energy difference lower than 0.2 keV) and "bow" events which are off-diagonal (energy difference $>$ 0.2 keV).

The bow events are corrected using a simple geometrical model that moves them in a direction determined from the tilted structures of Figure 5.28 until their values are the same.

With reference to Figure 5.29, the tilting of the lines is given by the angle and the points are moved according to the following parametrical stright line:

$$\begin{aligned} E'_C &= E_C + t \cdot sin\alpha \\ E'_S &= E_S + t \cdot cos\alpha \end{aligned} \tag{5.19}$$

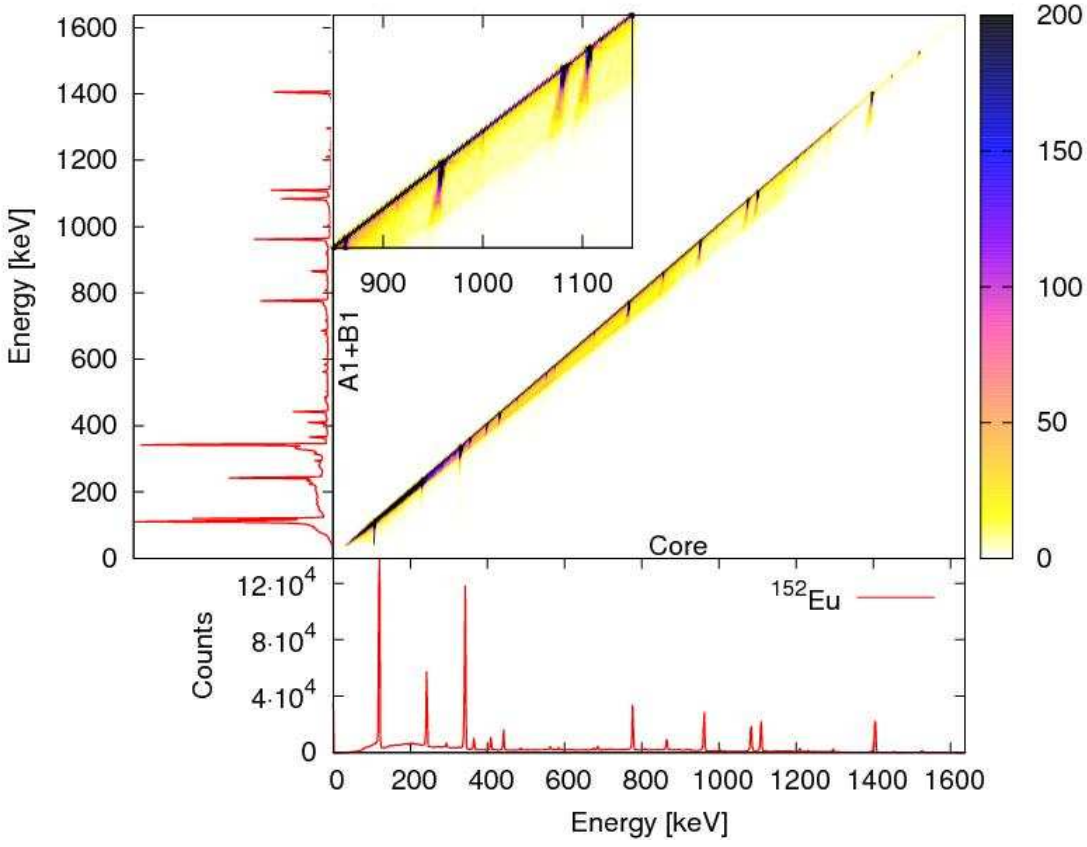


Figure 5.28 Correlation between core and sum of the segments.

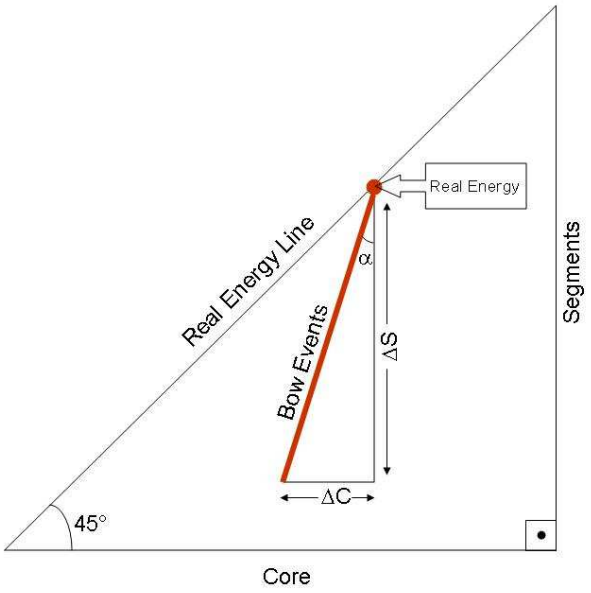


Figure 5.29 Geometrical model of the bow correction.

The parameter t is determined by requesting that the two corrected energies have the same value:

$$t = \frac{E_C - E_S}{cos\alpha - sin\alpha} \tag{5.20}$$

and

$$\begin{aligned} \Delta S &= \frac{E_C - E_S}{1 - tan\alpha} \\ \Delta C &= tan\alpha \cdot \frac{E_C - E_S}{1 - tan\alpha} \end{aligned} \tag{5.21}$$

The optimum tilting angle for the A1+B1 combination obtained from Figure 5.28 is 3.5 degree.

The correction is applied by replying the same data as of Figure 5.28 and the obtained result is presented in Figure 5.30, where all events are now, of course, on the main diagonal. As the correction modifies the energy of the segments and also the energy of the core there is a clear improvement of quality for both spectra. The improvement is particularly relevant for the sum-of-segments spectrum, resulting, as shown in Figure 5.31, in the removal of the low-energy double peaks.

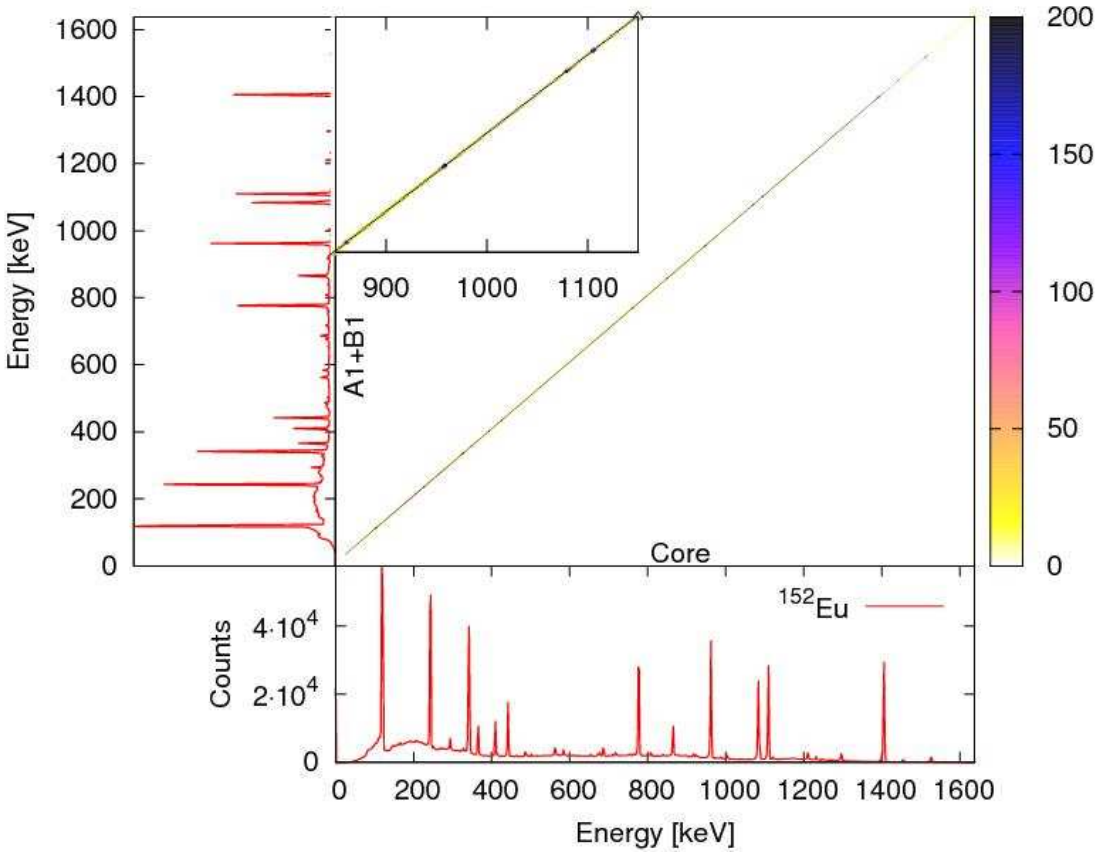


Figure 5.30 Correlation between core and sum of the segments after the bow correction.

The application of the same correction to higher segment-fold events is shown in Figure 5.32.

This correction procedure does not discard events and therefore the increased spectrum quality results in more intensity in the peaks, which corresponds to an effective increase of detection efficiency.

The final results of energy resolution, peak position and peak area as a function of the number of fired segments is reported in Table 5.2, Table 5.3 and Table 5.4 respectively.

5.3.4.3 Combining the Segment and Core Spectra

From Table 5.3 we see that the energy resolution of the core does not change much with the number of fired segments, while the resolution of the sum-energy spectra de-

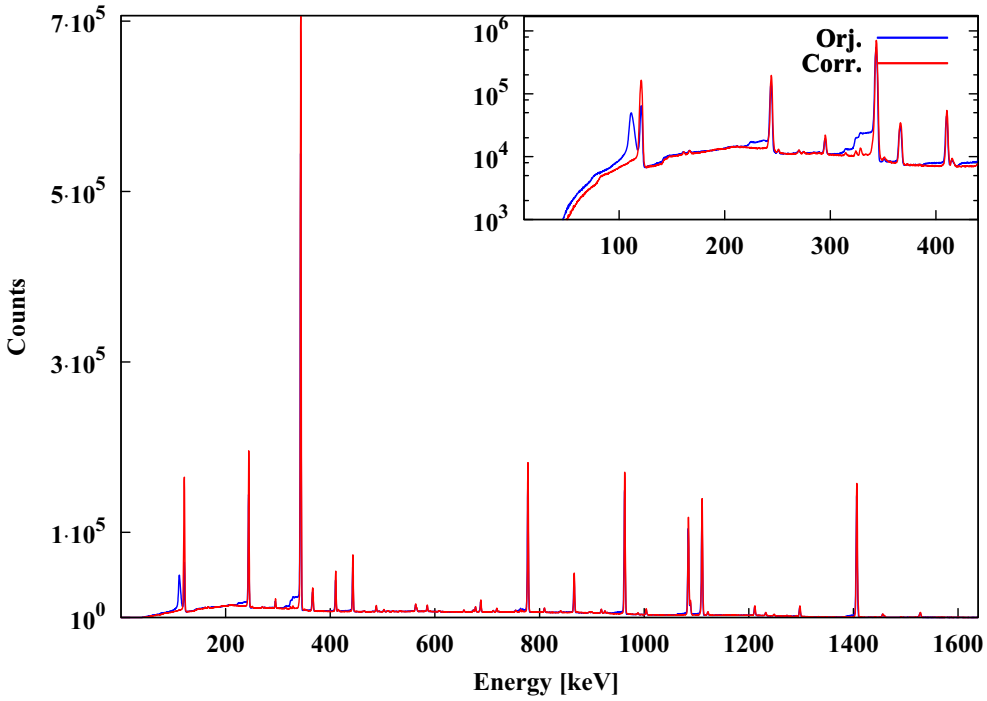


Figure 5.31 Original and corrected spectra for multiplicity 2 using a ^{152}Eu source.

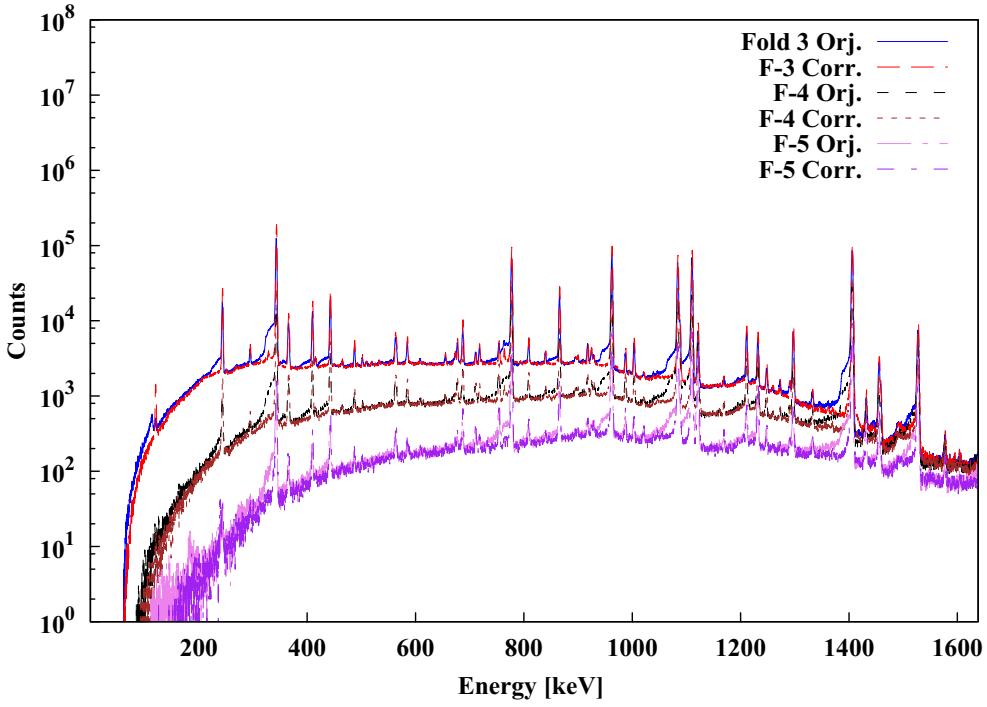


Figure 5.32 Original and Corrected spectra for multiplicity 3,4 and 5.

grades significantly. The worsening of energy resolution is ~ 0.6 keV/Fold and is due the random noise of the individual segments entering into the sum.

Table 5.2 Energy resolution (FWHM [keV]) of segment sum energy peaks for the $E_\gamma = 1407$ keV line of the ^{152}Eu source.

Fold	uncorr. Core	uncorr. Seg.	After Xtalk	After Bow
1	3.140	2.458	2.458	2.503
2	3.108	3.070	2.744	2.750
3	3.077	3.699	3.036	2.900
4	3.098	4.274	3.296	3.030
5	3.134	4.653	3.551	3.137
6	3.141	4.955	3.796	3.234
7	3.205	5.212	4.095	3.389

Table 5.3 Peak positions of the original spectra and after the corrections.

Fold	uncorr. Core	uncorr. Seg.	After Xtalk	After Bow
1	1407.988	1407.990	1407.986	1407.990
2	1407.991	1405.465	1407.637	1407.810
3	1408.001	1402.616	1407.302	1407.712
4	1407.969	1399.603	1406.943	1407.601
5	1407.916	1396.497	1406.577	1407.506
6	1407.864	1393.363	1406.190	1407.414
7	1407.834	1390.304	1405.711	1407.360

Table 5.4 Peak areas of the 1407 keV line before and after corrections. The gain in the high folds is very large

Fold	uncorr. Core	uncorr. Seg.	After Xtalk	After Bow	Gain(%)
1	1167736	1134915	1135050	1151285	(1)
2	2220245	2043983	2036520	2225689	(9)
3	1511729	1341356	1335096	1531236	(14)
4	563862	480854	481894	585015	(22)
5	133670	107333	110227	143483	(34)
6	22856	17168	18206	25714	(50)
7	3199	2148	2382	3746	(74)

In this situation we should use the energy from the segment-sum when the number of fired segments is 1 or 2 and the energy of the core for all higher multiplicities.

However the best possible value of the energy at each segment fold is obtained as a

proper combination of the two measurements:

$$E_{avg} = E_{seg} \cdot \alpha + E_{core} \cdot \beta \tag{5.22}$$

As it is known, the weights that provide the smallest error on the result are inversely proportional to the error (i.e. energy resolution) of the individual components:

$$\alpha = \frac{\sigma^2_{Core}}{\sigma^2_{Core} + \sigma^2_{Seg}}, \quad \beta = \frac{\sigma^2_{Seg}}{\sigma^2_{Core} + \sigma^2_{Seg}} \tag{5.23}$$

The "best" energy spectrum is produced by applying the weighed average event-by-event and the result the procedure, for a measurement with a ^{60}Co source and the detector in a better condition than the measurement with ^{152}Eu is presented in Table 5.5 and in Figure 5.33.

Table 5.5 Energy resolution (FWHM [keV]) of segment-sum energy peaks for the $E_\gamma =$ 1332.5 keV line of ^{60}Co. The sum of segment (after the corrections), the core and combined final best value.

Fold	Segment	Core	Average
1	2.106	2.671	2.112
2	2.440	2.619	2.188
3	2.717	2.582	2.259
4	2.962	2.565	2.334
5	3.187	2.553	2.401
6	3.405	2.543	2.495
7	3.625	2.500	2.536

To conclude, after a long series of calibrations and corrections, the performance of the complex AGATA detectors is very good for all kinds of interaction events that take place inside the germanium crystal.

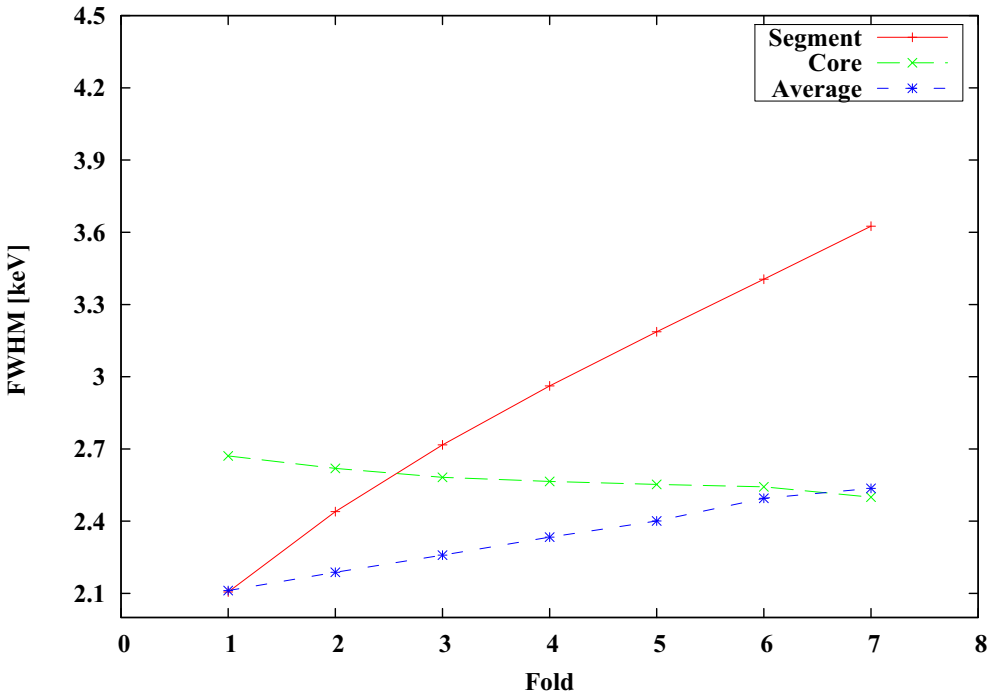


Figure 5.33 Energy resolution of ^{60}Co@1332.5 keV for core, corrected sum of segments and the best weighted average of the two.

6. DISCUSSION and CONCLUSION

The main part of the work reported in this thesis has been focused on understanding the crosstalk, the charge sharing and charge trapping problems that are intrinsic to the AGATA segmented detectors.

The crosstalk is corrected using a method that derives the coefficients from 1-segment and 2-segments events.

The detailed scan with the ^{241}Am source has shown clearly that the intensity of the charge trapping lines (bows) is correlated to the size of the segmentation lines, in good agreement with the model proposed by Amman and Luke (Amman and Luke, 2000).

The step forward with respect to the previous work is the development of a correction procedure to remove the effect of the lost charge. This correction procedure is based on the fact that the electrons collected in the non-segmented anode of the detector are not affected by the charge loss problem and provide therefore the proper reference value for the segments.

The gain in spectral quality on the segment sum obtained with this correction side is significant because, in particular at low energy, up to 30% of the intensity is recovered into the proper energy peak. Reminding that in a γ-ray tracking array the real information is extracted from the segments, any improvement in their response function corresponds to an overall gain in performance.

Almost all of the work has been done using the first symmetric AGATA crystal S001. However, the results are expected to be valid also for the final asymmetric detectors because the problems are connected to the size of the segmentation lines which depends on the production process of the manufactured and cannot be easily changed.

Preliminary measurement with the final AGATA asymmetric crystals that became available towards the end of this thesis confirm the existence of the problem and the validity of the correction procedure.

The AGATA Demonstrator Array which is being set-up at the Legnaro National Laboratory now, and all future phases of the AGATA with their increasing number of detectors will profit from results reported here.

REFERENCES

AGATA COLLABORATION, 2007. 5th agata week orsay. http://agata.lnl.infn.it/AgataWeek2007/programAW.htm. AGATA.

AMMAN, P., and LUKE, P., 2000. Position-sensitive germanium detectors for gamma-ray imaging and spectroscopy. Proc. SPIE, 4141:144.

ARNOLD, L., BAUMANN, R., CHAMBIT, E., FILLIGER, M., FUCHS, C., KIEBER, C., KLEIN, D., MEDINA, P., PARISEL, C., RICHER, M., SANTOS, C., and WEBER, C., 2005. Tnt digital pulse processor. Real Time Conference, 2005. 14th IEEE-NPSS, pages 265–269.

BAZZACCO, D., 1992. Proc. of Conf. on the Physics from Large γ-ray Detector Arrays,(Chalk River, Ontario, Canada), page 376.

BAZZACCO, D., 2004. The Advanced Gamma Ray Tracking Array AGATA. Nuclear Physics A, 746:248–254.

BEAUSANG, C. W., FORBES, S. A., FALLON, P., NOLAN, P. J., TWIN, P. J., MO, J. N.,LISLE, J. C., BENTLEY, M. A., SIMPSON, J., BECK, F. A., CURIEN, D., DEFRANCE, G., DUCHˆE NE, G., and POPESCU, D., 1992. Measurements on prototype Ge and BGO detectors for the Eurogam array. Nuclear Instruments and Methods in Physics Research A, 313:37–49.

BEAUSANG, C. W., and SIMPSON, J., 1996. TOPICAL REVIEW: Large arrays of escape suppressed spectrometers for nuclear structure experiments. Journal of Physics G Nuclear Physics, 22:527–558.

BELLATO, M., 2007. Agata trigger processor. In 5th AGATA Week, Orsay.

BERGER, M. J., HUBBELL, J. H., SELTZER, S. M., CHANG, J., COURSEY, J. S., SUKUMAR,R., and ZUCKER, D. S., 1998. Photon cross sections database. Technical report, National Institute of Standards and Technology.

BERTOLINI, G., and COCHE, A., 1968. Semiconductor Detectors. Elsevier-North Holland, Amsterdam. BRUYNEEL, B., REITER, P., and PASCOVICI, G., 2006. Characterization of large volume HPGe detectors. Part II: Experimental results. Nuclear Instruments and Methods in Physics Research A, 569:774–789.

BRUYNEEL B. and REITER P., and PASCOVICI, G., 2006. Characterization of large volume HPGe detectors. Part II: Experimental results. Nuclear Instruments and Methods in Physics Research A, 569:774.789.

BRUYNEEL B. and REITER P., 2008. Crosstalk properties of 36-fold segmented symmetric hexagonal hpge detectors. Nuclear Instruments and Methods in Physics Research Section A: Accelerators, Spectrometers, Detectors and Associated Equipment, In Press, Uncorrected Proof:–.BAZZACCO, D., 1992. Proc. of Conf. on the Physics from Large g-ray Detector Arrays, (Chalk River, Ontario, Canada), page 376.

CAEN, C., 2007. Mod. n1728a/n1728b 4 ch. flash adc. Technical report, CAEN.

CHEN, C., BOGGS, S., BOLOTNIKOV, A., COOK, W., HARRISON, F., and SCHINDLER, S., 2002. Numerical modeling of charge sharing in CdZnTe pixel detectors. IEEE Transactions on Nuclear Science, 49, Issue: 1, Part2:270–276.

COBURN, W., BOGGS, S., AMROSE, S., LIN, R., BURKS, M., AMMAN, M., LUKE, P., MADDEN, N., and HULL, E., 2001. Results of Charge Sharing Test In a Ge-Strip Detector. IEEE Transactions on Nuclear Science, 1:226–229.

CORNELL, J., 2003. The EURISOL Report. GANIL.

DELEPLANQUE, M. A., and DIAMOND, R., 1988. Gammasphere proposal. Lawrence Berkley National Laboratory Report, 5202.

DUCHˆENE, G., BECK, F. A., TWIN, P. J., DE FRANCE, G., CURIEN, D., HAN, L., BEAUSANG, C. W., BENTLEY, M. A., NOLAN, P. J., and SIMPSON, J., 1999. The Clover: a new generation of composite Ge detectors. Nuclear Instruments and Methods in Physics Research A, 432:90–110.

EBERTH, J., THOMAS, H. G., BRENTANO, P. V., LIEDER, R. M., J¨A GER, H. M.,K¨AMMERLING, H., BERST, M., GUTKNECHT, D., and HENCK, R., 1996. Encapsulated Ge detectors: development and first tests. Nuclear Instruments and Methods in Physics Research A, 369:135–140.

EVANS, R., 1982. The Atomic Nucleus. Krieger, New York.

FARNEA, E., 2004. comparison of the a120, a180 configurations.

http://agata.pd.infn.it/documents/simulations/comparison.html.

_____, 2005. The agata demonstrator. http://agata.pd.infn.it/documents/simulations/demonstrator.html.

FARNEA, E., and BAZZACCO, D., 2004. A Monte Carlo code for the AGATA array.LNL-INFN(REP), 202:158–159.

GADDY, L., and KAWAI, H., 2000. Dynamic performance testing of digital audio d/a converters. Technical report, Burr-Brown, Texas.

GADEA, A., 2005. First results of the CLARA-PRISMA setup installed at LNL. European Physical Journal A, 25:421–426.

GADEA, A., NAPOLI, D. R., DE ANGELIS, G., MENEGAZZO, R., STEFANINI, A. M., CORRADI, L., AXIOTIS, M., BERTI, L., and FIORETTO, E., 2003. Coupling a CLOVER detector array with the PRISMA magnetic spectrometer. European Physical Journal A, 20:193–197.

GAST, W., LIEDER, R., MIHAILESCU, L., ROSSEWIJ, M., BRANDS, H., GEORGIEV, A., STEIN, J., and KR¨OLL, T., 2001. Digital signal processing and algorithms for gamma-ray tracking. IEEE Transactions on Nuclear Science, 48, Issue: 6:2380–2384.

GATTI, E., PADOVINI, G., and RADEKA, V., 1982. Signal evaluation in multielectrode radiation detectors by means of a time dependent weighting vector. Nuclear Instruments and Methods, 193:651–653.

GEANT4 COLLABORATION, 2003. Geant4 - a simulation toolkit. Nuclear Instruments and Methods in Physics Research A, 506:250–303.

GEORGIEV, A., and GAST, W., 1993. Digital pulse processing in high resolution, high throughput, gamma-ray spectroscopy. IEEE Transactions on Nuclear Science, 40, Issue: 4, Part 1-2:770–779.

GERL, J., and KORTEN, W., 2001. Technical proposal for the AGATA project.

GIELEN, G., 2006. Analog Building Blocks for Signal Processing. KULeuven-ESATMICAS, Leuven. G¨ORGEN, A., 2003. The position sensitivity of the agata prototype crystal analyzed using a database of calculated pulse shape. http://wwwdapnia.cea.fr/Sphn/Deformes/Agata/local/files/report.pdf.

GORGEN, A., 2003. The position sensitivity of the agata prototype crystal

analyzed using a database of calculated pulse shape. *http://wwwdapnia.cea.fr/Sphn/Deformes/Agata/local/files/report.pdf*.

GRETA STEERING COMMITTEE, 2003. Proposal for GRETINA. Lawrence Berkeley National Laboratory.

HAYWARD, J., and WEHEB, D., 2008. Incomplete charge collection in an HPGe doublesided strip detector. Nuclear Instruments and Methods in Physics Research A, 586:215–223.

JORDANOV, V. T., and KNOLL, G. F., 1994. Digital synthesis of pulse shapes in real time for high resolution radiation spectroscopy. Nuclear Instruments and Methods in Physics Research A, 345:337–345.

JULIN, R., 2005. Gamma-ray and conversion-electron spectroscopy of exotic heavy nuclei. Lect. Notes Phys., 651:263–294.

KALEMCI, E., and MATTESON, J., 2002. Investigation of charge sharing among electrode strips for a cdznte detector. Nuclear Instruments and Methods in Physics Research A, 478:527–537.

KNOLL, G. F., 2000. Radiation detection and measurement. Radiation detection and measurement. 3rd ed. New York, NY: Wiley, 2000. xiv, 802 p. ISBN 0471073385.

KROLL, T., and BAZZACCO, D., 2001. Simulation and analysis of pulse shapes from highly segmented HPGe detectors for the g-ray tracking array MARS. Nuclear Instruments and Methods in Physics Research A, 463:227–249.

_____, 2006. A genetic algorithm for the decomposition of multiple hit events in the g-ray tracking detector MARS. Nuclear Instruments and Methods in Physics Research A, 565:691–703.

KUGLER, E., 2000. The ISOLDE facility. Hyperfine Interactions, 129:23–42.

LEE, . Y., 1990. The Gammasphere. Nuclear Physics A, 520:641.

LOPEZ-MARTENS, A., HAUSCHILD, K., KORICHI, A., ROCCAZ, J., and THIBAUD, J.-P., 2004. g-ray tracking algorithms: a comparison. Nuclear Instruments and Methods in Physics Research A, 533:454–466.

MILECHINA, L., and CEDERWALL, B., 2003. Improvements in g-ray

reconstruction with positive sensitive ge detectors using the backtracking method,. Nuclear Instruments and Methods in Physics Research Section A, 508(3):394–403.

MUELLER, W., CHURCH, J., GLASMACHER, T., GUTKNECHT, D., HACKMAN, G., HANSEN, P., HU, Z., MILLER, K., and QUIRIN, P., 2001. Thirty-two-fold segmented germanium detectors to identify gamma-rays from intermediate-energy exotic beams. Nuclear Instruments and Methods in Physics Research Section A: Accelerators, Spectrometers, Detectors and Associated Equipment, 466:492–498.

NESPOLO, M., 2004. Pulse Shape Analysis with Germanium Detectors: from MARS to AGATA. PhD thesis, Padova University.

NYQUIST, H., 1924. Certain factors affecting telegraph speed. Bell Syst. Tech. J., 3:324.

PIQUERAS, ., BECK, F., PACHOUD, E., and DUCHENE, G., 2004. A probabilistic gray tracking method for germanium detectors. Nuclear Instruments and Methods in Physics Research Section A.

PRETE, G., 2007. SPES Technical Design for an Advanced Exotic Ion Beam Facility at LNL. INFN-LNL-220.

PULLIA, A., ZOCCA, F., and PASCOVICI, G., 2006. An Advanced Preamplifier for Highly Segmented Germanium Detectors. IEEE Transactions on Nuclear Science, 53, Issue: 5, Part 2:2869–2875.

RECCHIA, F., 2008. In-beam test and imaging capabilities of the AGATA prototype detector. PhD thesis, Universit`a degli Studi di PADOVA.

ROSSI-ALVAREZ, C., 1993. Nucl. Phys. News Europe, 2:10.

_____, 1998. The EUROBALL array. Nuovo Cimento A Serie, 111:601.

SCHMID, G. J., DELEPLANQUE, M. A., and LEE, . Y., 1999. A g-ray tracking algorithm for the greta spectrometer. Nuclear Instruments and Methods in Physics Research Section A, 430(1):69–83.

SCHMID, G. J., DELEPLANQUE, M. A., LEE, . Y., STEPHENS, F. S.,

VETTER, K., CLARK, R. M., DIAMOND, R. M., FALLON, P., MACCHIAVELLI, A. O., and MACLEOD, R. W., 1999. A g-ray tracking algorithm for the GRETA spectrometer. Nuclear Instruments and Methods in Physics Research A, 434:481–481.

SHATKAY, H., 1995. The Fourier Transform-A Primer. Brown University.

SHEPHERD, S. L., NOLAN, P. J., CULLEN, D. M., APPELBE, D. E., SIMPSON, J., GERL, J., KASPAR, M., KLEINBOEHL, A., PETER, ., REJMUND, M., SCHAFFNER, H., SCHLEGEL, C., and DE FRANCE, G., 1999. Measurements on a prototype segmented Clover detector. Nuclear Instruments and Methods in Physics Research A, 434:373–386.

SIMPSON, J., 1997. The Euroball Spectrometer. Zeitschrift fr Physik A Hadrons and Nuclei, 358:139.

SMITH, S., 1999. The Scientist and Engineer's Guide to Digital Signal Processing. California Technical Publishing.

STEIN, J., SCHEUER, F., GAST, W., and GEORGIEV, A., 1996. X-ray detectors with digitized preamplifiers. Nuclear Instruments and Methods in Physics Research Section B: Beam Interactions with Materials and Atoms, 113(1-4):141 – 145. Accelerators in Applied Research and Technology.

SVENSSON, C., HACKMAN, G., PEARSON, C., SCHUMAKER, M. and WATTERS, L., 2005. Position sensitivity of the tigress 32-fold segmented HPGe Clover detector. Nuclear Inst. and Methods in Physics Research, A, 540:348–360.

VAN DER MAREL, J., and CEDERWALL, B., 1999. Backtracking as a way to reconstruct compton scattered. Nuclear Instruments and Methods in Physics Research Section A, 437(2-3):538–551.

VAN DER MAREL, J., and CEDERWALL, B., 2002. g-ray tracking in germanium: the backtracking method. Nuclear Instruments and Methods in Physics Research Section A, 477(1-3):391–396.

VENTURELLI, R., and BAZZACCO, D., 2005. Adaptive grid search as pulse shape analysis algorithm for g-tracking and results. LNL-INFN(REP), 204:220–221.

VENTURELLI, R., BAZZACCO, D., BELLATO, M., PULLIA, A., and KR¨OLL, T., 2002. Fold-dependent energy correction in segmented germanium detectors. LNL-INFN(REP), 198:156–157.

WARR, N., EBERTH, J., PASCOVICI, G., THOMAS, H. G., and WEISSHAAR, D., 2003.MINIBALL: The first gamma-ray spectrometer using segmented, encapsulated germanium detectors for studies with radioactive beams. European Physical Journal A, 20:65–66.

WILHELM, M., EBERTH, J., PASCOVICI, G., RADERMACHER, E., THOMAS, H. G., VON BRENTANO, P., PRADE, H., and LIEDER, R. M., 1996. The response of the Euroball Cluster detector to g-radiation up to 10 MeV. Nuclear Instruments and Methods in Physics Research A, 381:462–465.

WOLLERSHEIM, H. J., APPELBE, D. E., BANU, A., BASSINI, R., BECK, T., BECKER, F., and BEDNARCZYK, P., 2005. Rare ISotopes INvestigation at GSI (RISING) using gamma-ray spectroscopy at relativistic energies. Nuclear Instruments and Methods in Physics Research A, 537:637–657.

ZOCCA, F., 2008. New technologies for low-noise wide-dynamic-range preamplification of HPGe segmented detector signals. PhD thesis, Universit`a degli Studi di Milano.

CURRICULUM VITAE

Name	: Sezgin AYDIN
Date of Birth	: 1979
Nationality	: Turkish

EDUCATIONAL BACKGROUND

1996-2001	: B.Sc Çukurova University
2001-2004	: M.Sc Çukurova University
2004-2009	: Ph.D Çukurova University

PROFFESSIONAL BACKGROUND

Nov. 2002 - Apr. 2004	: Research assistant at Niğde University
Apr. 2004 - now	: Research assistant at Çukurova University
Oct. 2006 - Sept. 2007	: Guest student in Padova University Padova, Italy with Erasmus Program
Feb. 2008 - May 2008	: Guest student in Padova University Padova, Italy with FAI Scholarship